

University of Nevada, Reno

**Using Landsat ETM+ and ASTER Sensors to Aid the Mineral Assessment of the
Desert National Wildlife Refuge, Clark and Lincoln Counties, Nevada**

A thesis submitted in partial fulfillment of the
requirements for the degree of
Master of Science in Geology

by

Timothy F. Cramer

Dr. John L. Muntean

&

Dr. Wendy Calvin

Thesis Advisors

August, 2014

© by Timothy F. Cramer 2014
All Rights Reserved



University of Nevada, Reno
Statewide • Worldwide

THE GRADUATE SCHOOL

We recommend that the thesis
prepared under our supervision by

Timothy F. Cramer

entitled

**Using Landsat ETM+ and ASTER Sensors to Aid the Mineral Assessment of the
Desert National Wildlife Refuge, Clark and Lincoln Counties, Nevada**

be accepted in partial fulfillment of the
requirements for the degree of

MASTER OF SCIENCE

Geology

John L. Muntean, Ph.D., Advisor

And

Wendy Calvin, Ph.D., Advisor

Scott Bassett, Ph.D., Graduate School Representative

David W. Zeh, Ph.D., Dean, Graduate School

August, 2014

Abstract

The Desert National Wildlife Refuge in southern Nevada has been selected for remote sensing analysis as part of a mineral assessment required for renewal of mineral withdrawal. The area of interest is nearly 3,000 km² and covers portions of 5 different ranges with little to no infrastructure. Assessing such a large area using traditional field methods is very time intensive and expensive. The study described here serves as a pilot study, testing the capability of Landsat ETM+ and ASTER satellite imagery to remotely identify areas of potentially mineralized lithologies. This is done by generating a number of band ratio, band index, and mineral likelihood maps identifying 5 key mineral classes (silica, clay, iron oxide, dolomite and calcite), which commonly have patterned zonation around ore deposits. When compiled with available geologic and geochemical data sets, these intermediate products can provide guidance for targeted field evaluation and exploration. Field observations and spectral data collected in the laboratory can then be integrated with ASTER imagery to guide a Spectral Angle Mapper algorithm to generate a distribution map of the five mineral classes.

The methods presented found the ASTER platform to be capable of remotely assessing the distribution of various lithologies and the mineral potential of large, remote areas. Furthermore areas of both high and low potential for ore deposits can be identified and used to guide field evaluation and exploration. Remote sensing studies of this caliber can be performed relatively quickly and inexpensively resulting in datasets, which can result in more accurate mapping and the identification of both lithologic boundaries and

previously unidentified alteration associated with mineralization. Future mineral assessments and exploration activity should consider similar studies prior to field work.

Acknowledgements

I would like to first thank my two advisors, Dr. John Muntean and Dr. Wendy Calvin for their support, encouragement, and guidance throughout the past two years. Having you both there to provide feedback and suggestions on the different aspects of this project has been invaluable, and the mentorship has truly been inspiring.

Thanks to Scott Bassett for taking the time to join my committee allowing me to finish in the timeliest way possible. I also thank Bret Pecoraro whose help during field work and validation was much appreciated. Additionally, I thank the staff and support of the NBMG, the UNR DGSE, the College of Science, as well as the USFWS for helping fund my time here. Thanks also to my previous academic mentors who have cultivated in me a passion for seeking a deeper understanding the world around me: Drs. Hilde Schwartz, Casey Moore and Jeremy Hourigan of U.C. Santa Cruz, Gary Hayes MSc. of Modesto JC, and Drs. Steve Wesnousky and Jim Faulds of UNR. Thanks to my peers and friends here at UNR, including Melissa Penfold, Corina Forson, Dylan Baldwin, Christine Ruhl, and Neil Pearson, who have been particularly helpful in both encouragement to keep at it and providing some much needed distraction. Thanks also to my lifelong friends Brian Wallace, Zach Mayo, and Athena DuBois who have challenged me since childhood to strive for my best and chase my dreams. Finally, I want to thank my family for their support over the years. Ultimately it was their love, encouragement, and up bringing that have allowed me to leap in and make the best of every opportunity and challenge I've encountered over the years. So a special thanks to my father Jeff, my mother and step-father Gretchen and Fred Gack, my brother Zach and my sister Jessica.

Contents

Abstract	i
Acknowledgements	iii
List of Tables	vi
List of Figures	vii
1.0 Introduction	1
2.0 Background	3
2.1 Regional Geology and Physiographic Setting	3
2.2 History of DNWR	9
2.3 Previous work	12
2.4 Spectroscopy.....	14
2.4.1 Laboratory Spectroscopy.....	16
2.4.2 Remote Sensing Imagery.....	17
2.5 Remote Sensing Instruments	18
2.5.1 Landsat ETM+.....	18
2.5.2 ASTER.....	20
2.6 Remote Mapping of Geology and Hydrothermal Alteration.....	21
2.7 Hydrothermal Ore Deposits in Nevada.....	24
2.7.1 Carlin-Type Deposits	26
2.7.2 Epithermal and Intrusion Related Deposits	28
2.7.3 Mississippi-Valley Type Deposits	31
3.0 Methods	34
3.1 Data Acquisition and Computer Software	34
3.2 Data Processing	36
3.2.1 Landsat ETM+.....	37
3.2.2 ASTER.....	39
3.2.3 Spectra.....	44
3.3 Field Validation/Verification.....	47
4.0 Results	47
4.1 Landsat ETM+ Band Ratios	47
4.2 ASTER	54
4.2.1 Band Ratio Images	54
4.2.3 Mineral Probability Mapping	60
4.3 Spectrometry.....	69
4.3.1 VNIR-SWIR (Lab and ASTER).....	69
4.3.2 TIR (Lab and ASTER)	72
5.0 Discussion	73
5.1 Landsat ETM+ Results.....	73
5.2 ASTER Results	74
5.2.1 ASTER Processing and Band Ratio Images.....	74
5.2.2 ASTER Mineral Distribution Mapping	75
5.3 Spectrometry.....	82

6.0 Conclusions	83
References	85
Appendix A – Band Ratio Composite Image.....	92
Appendix B – Final Mapping Parameters	115

List of Tables

Table 1. Landsat TM Spectral and Spatial Characteristics.....	13
Table 2. Landsat ETM+ Spectral and Spatial Characteristics.....	18
Table 3. ASTER Spectral and Spatial Characteristics.....	21
Table 4. Definition of Remote Sensing Algorithms and Processes.....	22
Table 5. Summary of Minerals related to Alteration and Formation.....	23
Environment	
Table 6. Summary of Alteration Environments and SWIR Response of.....	24
Associated Minerals	
Table 7. List of Landsat ETM+ Band Ratio Images and Descriptions.....	38
Table 8. List of ASTER Band Ratios/Band Ratio Images and Descriptions.....	41
Table 9. List of ASTER Mineral Index Methods for Likelihood Map.....	42

List of Figures

Figure 1. Location Map of the DNWR and within Nevada and the Great Basin.....	2
Figure 2. Geologic Map of the DNWR.....	4
Figure 3. Geologic Map Legend.....	5
Figure 4. DNWR Historic Mines, Prospects, and Gass Peak Mining District.....	11
Figure 5. Electro-magnetic Spectrum with Atmospheric Transmission.....	15
Figure 6. Comparison of Landsat ETM+ and ASTER S Characteristics.....	19
Figure 7. Mineral Deposits of Nevada.....	26
Figure 8. Zonation of Carlin-Type Deposits.....	27
Figure 9. Zonation of Epithermal High Sulfidation Deposits.....	29
Figure 10. Zonation of Epithermal Low Sulfidation Deposits.....	29
Figure 11. Ore Deposits Related to Intrusive Rocks.....	30
Figure 12. Mineral Deposits Near the DNWR.....	32
Figure 13. Zonation Around with MVT Deposits.....	33
Figure 14. Processing Methods Flow Chart.....	36
Figure 15. DNWR ASTER Band Ratio 3.....	40
Figure 16. Mineral Likelihood Index Map.....	46
Figure 17. DNWR Geologic Map and ETM+ Band Ratio 3 (Full).....	49
Figure 18. DNWR Geologic Map and ETM+ Band Ratio 3 (Lake Mine Area).....	50
Figure 19. DNWR Geologic Map and ETM+ Band Ratio 3 (East Desert Range)...	51
Figure 20. DNWR Geologic Map and ETM+ Band Ratio 3 (Gass Peak District)...	52
Figure 21. DNWR Geologic Map and ASTER Band Ratio 1 (Full).....	55
Figure 22. DNWR Geologic Map and ASTER Band Ratio 1 (Lake Mine Area).....	56

Figure 23. DNWR Geologic Map and ASTER Band Ratio 1 (East Desert Range)..	57
Figure 24. DNWR Geologic Map and ASTER Band Ratio 1 (Gass Peak District)...	58
Figure 25. DNWR Spectral Angle Mapper Result.....	61
Figure 26. Silica and Iron Oxide Distribution Maps.....	62
Figure 27. Final Mineral Distribution Map.....	63
Figure 28. Final Mineral Distribution Map (Lake Mine Area).....	64
Figure 29. Final Mineral Distribution Map (East Desert Range).....	65
Figure 30. Final Mineral Distribution Map (Gass Peak District).....	66
Figure 31. Final Mineral Distribution Map (Polygons).....	67
Figure 32. VNIR and SWIR Spectral Plots.....	71
Figure 33. TIR Spectral Plots.....	72
Figure 34. Photographs from Field Validation.....	77
Figure 35. TIR PCA Band Ratio Map Highlighting Silica.....	79

1.0 Introduction

The Desert National Wildlife Refuge (DNWR), located in Lincoln and Clark Counties, Nevada, 15 km north of Las Vegas, NV (Figure 1), has been selected for remote sensing analysis in partial fulfillment of a mandatory mineral assessment required for the mineral withdrawal renewal. Completion of the mineral assessment allows management of the refuge to continue at the direction of the U.S. Fish and Wildlife Service, with continued protection from the impacts of resource exploration and extraction. Additionally, the assessment serves to identify any resources, which may prove important for future utilization. Most importantly, the methods described here serve as a pilot study for future mineral assessments of land considered for mineral withdrawal, as well as mineral exploration performed by industry over arid regions.

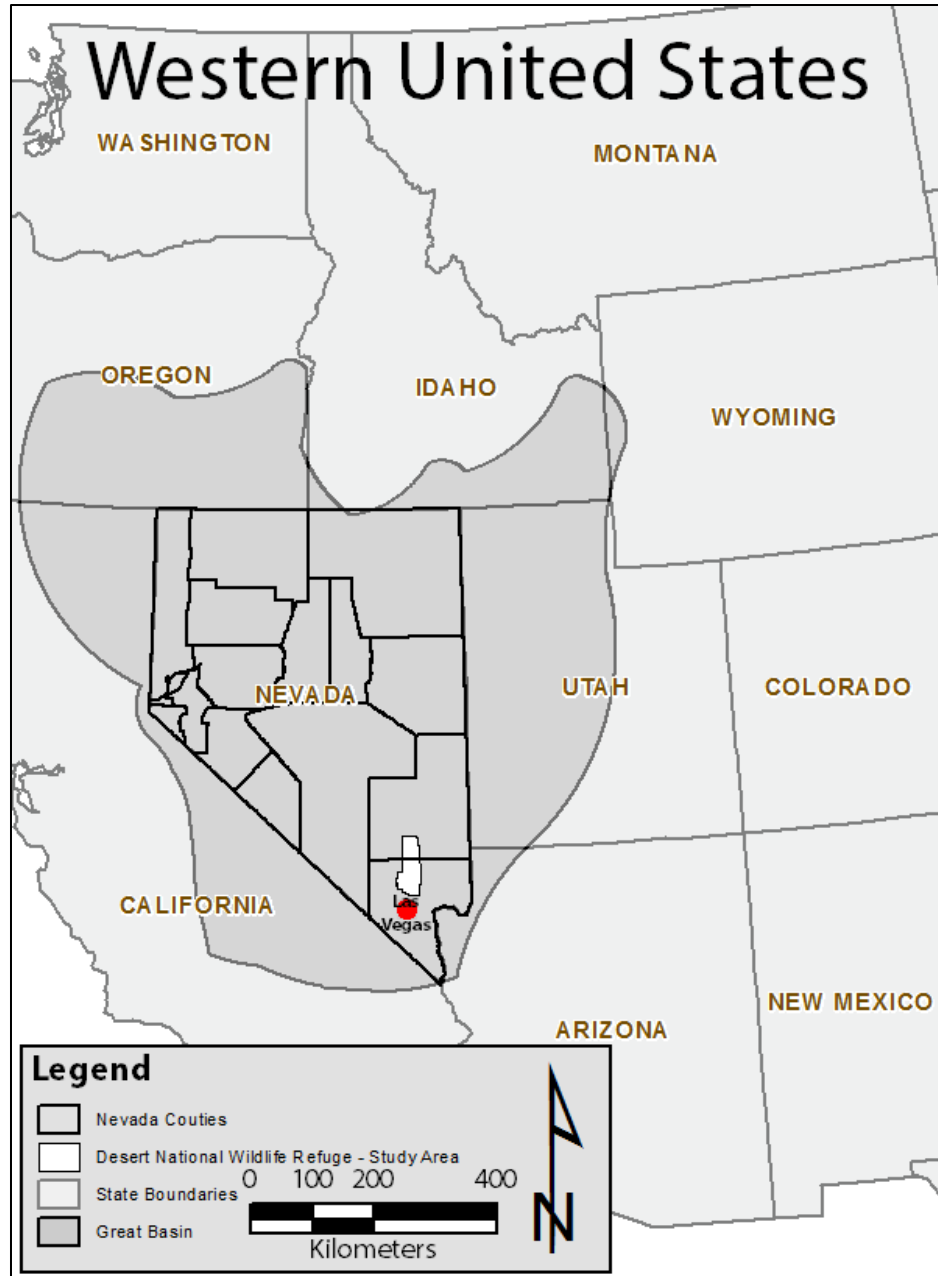


FIGURE 1: Location map showing the area of interest in the western U.S.A. relative to Las Vegas, NV and the Great Basin physiographic province.

The large area of interest (AOI) necessitates an initially broad evaluation of the DNWR to identify areas for more detailed investigations in the field. Landsat Enhanced Thematic Mapper Plus (ETM+) and the Advanced Spaceborne Thermal Emission and Reflection Radiometer (ASTER) satellites are Earth orbiting, spaceborne satellites

engineered to identify a variety of ground cover across large areas. ASTER is engineered with additional bands specifically designed to aid in lithology and mineral identification. In this study, remote sensing satellites were used to guide field studies and remotely map areas of possible economic mineral potential. Remote mineral mapping and field exploration are supplemented with a field sampling program, which utilizes laboratory spectral analysis for mineral identification and mapping. Two high resolution laboratory spectrometers are used: the Analytical Spectral Devices (ASD) Terraspec, which collects data in the visual-near infrared (VNIR) and short-wave infrared (SWIR) portion of the electromagnetic spectrum, and the Thermo Nicolet, which collects data in the thermal infrared (TIR) regions. By utilizing lab spectrometers, individual minerals are identified based on their unique spectral characteristics. By combining preliminary remote sensing imagery and geologic and geochemical data into a geographic information system (GIS), the data can be viewed simultaneously providing direction for field exploration, validation, and sampling programs. Post-fieldwork, remote sensing image processing and integration of sample spectral data has resulted in mineral potential maps with high levels of confidence.

2.0 Background

2.1 Regional Geology and Physiographic Setting

The Desert National Wildlife Refuge is located in the southern part of the Basin and Range physiographic province (Figure 1) and is characterized by north to north-east trending mountain ranges separated by alluvial and pluvial valleys (Figure 2 and Figure 3).

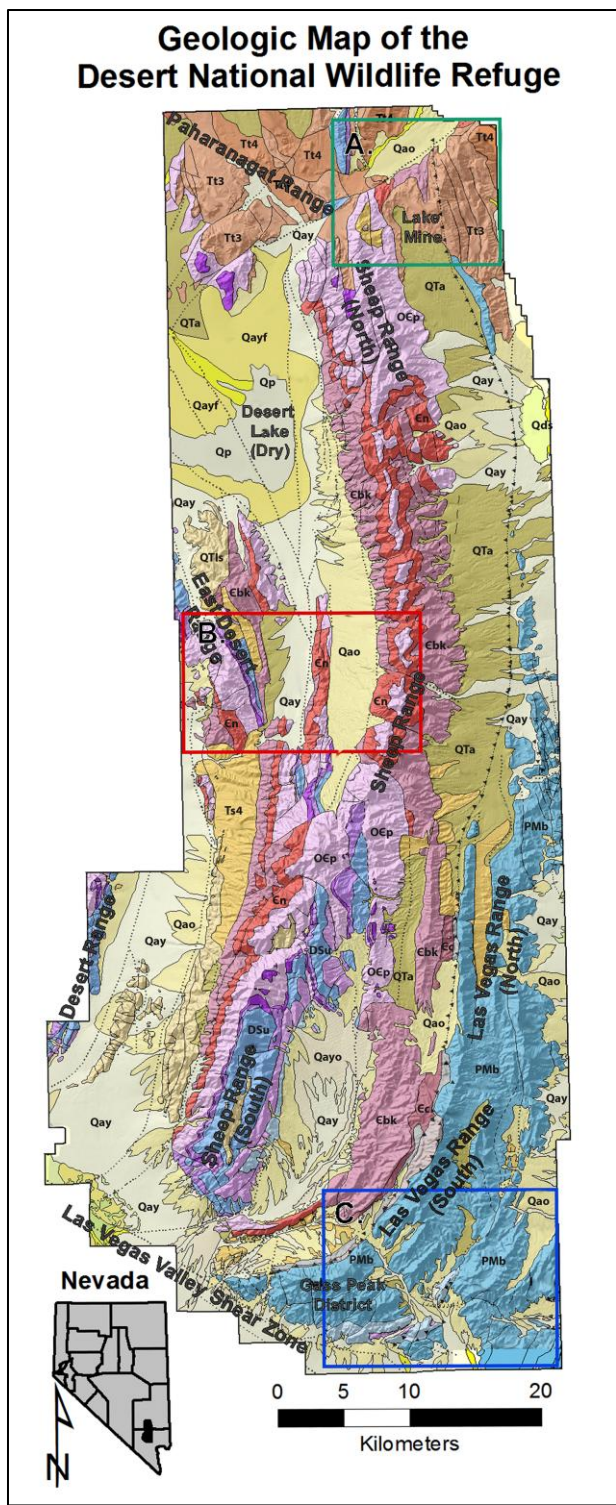

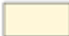
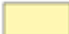
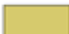
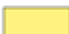

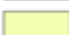



FIGURE 2: Modified geologic map of DNWR study area using ASTER digital elevation model to highlight ranges and structures. ASTER GDEM is a product of METI and NASA. Geologic map modified from Page et al. (2005). Boxes represent general areas discussed in detail in this text. A. Lake Mine area; B. East Desert Range; C. Gass Peak District. Legend for this map is in Figure 3.


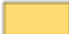



Legend

Geologic Units



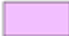
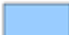









Quaternary

-  Qay - Young alluvium (Holocene to latest Pleistocene)
-  Qayo - Intermediate alluvium (late to middle Pleistocene)
-  Qao - Old alluvium (middle to early Pleistocene)
-  QTa - Oldest alluvium (early Pleistocene to Pliocene)
-  Qayf - Young fine-grained alluvium (Holocene to late Pleistocene)
-  Qp - Playa deposits (Holocene to late Pleistocene)
-  Qds - Modern and past groundwater discharge deposits (Holocene to late Pleistocene)
-  QTIs - Landslide and megabreccia deposits (Pleistocene to Miocene?)

Tertiary

-  Tb - Older basaltic lava flows (Pliocene and Miocene)
-  Ts4 - Sedimentary rocks, unit 4 (Miocene and Oligocene)
-  Tt4 - Ash-flow tuffs and interbedded airfall tuffs, unit 4 (Miocene)
-  Tt3 - Ash-flow tuffs and interbedded airfall tuffs, unit 3 (Miocene and Oligocene)
-  Tt2 - Ash-flow tuffs and interbedded airfall tuffs, unit 2 (Oligocene)

Paleozoic

-  PMb - Bird Spring Formation and related rocks (Lower Permian to Upper Mississippian)
-  Mm - Monte Cristo Group of Langenheim and others (1962) (Upper and Lower Mississippian)
-  MDu - Lower Mississippian to Middle Devonian rocks, undivided
-  DSu - Middle Devonian to Silurian rocks, undivided
-  Oes - Ely Springs Dolomite (Upper Ordovician)
-  Oep - Eureka Quartzite (Mid. Ord.) and Pogonip Group (Mid. Ord. to Upp. Camb.), undiv.
-  Oe - Eureka Quartzite (Middle Ordovician)
-  Op - Pogonip Group (Lower Ordovician)
-  O€p - Pogonip Group (Middle Ordovician to Upper Cambrian)
-  €nb - Nopah (Upp. Camb.) and Bonanza King (Upp. and Mid. Camb.) Fm., undiv.
-  €n - Nopah Formation (Upper Cambrian)
-  €bk - Bonanza King Formation (Upper and Middle Cambrian)
-  €c - Carrara Formation (Middle and Lower Cambrian)

Proterozoic

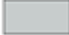

-  €Zw - Wood Canyon Formation (Lower Cambrian and Late Proterozoic)
-  Zs - Stirling Quartzite (Late Proterozoic)

Figure 3: Legend showing geologic units displayed in Figure 2 above. Modified from Page et al. (2005).

Quaternary map units (Qay, Qayo, Qao, QTa, and Qayf) from Figure 2 and Figure 3 are alluvial deposits comprised of Holocene to Pleistocene unconsolidated to consolidated, fine sand to gravel sized clasts, which typically form large alluvial fans or piedmont slopes (Page et al., 2005). Additional Quaternary deposits (Qp and Qds) are Holocene to late Pleistocene clay, silt, sand, and mud forming playa and ground water discharge deposits (Page et al., 2005). QTls indicates Pleistocene to Miocene landslide and mega-breccia deposits.

Ts4 is a moderate to well consolidated fluvial and lacustrine unit, comprised of tuffaceous sandstone, conglomerate, limestone, siltstone, mudstone and gypsum, which was deposited during the Miocene and Oligocene. Other Tertiary units include: Pliocene and Miocene basalt flows (Tb); and Miocene and Oligocene ash-flow and interbedded air-fall tuffs (Tt4, Tt3, and Tt2). These volcanic rocks are most likely derived from any one of several caldera complexes 30-70 km north to northeast of the DNWR (Page et al., 2005).

Paleozoic units in the DNWR consist of carbonate shelf deposits and slope to basin sequence rocks. The Pennsylvanian-Mississippian Bird Spring Formation (PMb) is comprised of limestone, dolostone, siltstone, sandstone, shale, and chert, as well as submarine debris flow conglomerate and turbidite beds. Mississippian Monte Cristo Group (Mm) rocks consist of limestone with sparse to locally abundant chert nodules and beds. MDu includes the Devonian Guilmette, Mississippian-Devonian Pilot Shale, and Mississippian Joana Limestone formations. These formations are predominantly limestone and dolostone with local dolomitic sandstone (Page et al., 2005). They are locally cherty, bioclastic, platy, or bioturbated (Page et al., 2005). The Ely Springs

Dolomite (Oes) contains micritic dolostone with local laminations of chert and unconformably overlies Eureka Quartzite (Oe). The Eureka Quartzite (Oe) is comprised of medium grained quartzite, friable sandstone, and minor sandy carbonate beds. The Pogonip Group (Op) is cherty dolostone. Op is locally mapped with Oe, which is collectively referred to as Oep.

OEp represent older Pogonip Group rocks comprised of Antelope Valley and Goodwin Limestones. These rocks are middle Ordovician to Upper Cambrian and are typically bioclastic and arenaceous limestone and dolostone (Page et al., 2005).

Enb, represents Nopah and Bonanza King Formations which are undifferentiated. The Nopah Formation (En) is typically burrow-mottled dolostone with minor silty limestone, and scattered chert layers and nodules, which are interbedded to form distinctive banding. En rocks also include the Dunderberg Shale Member, which consists of siltstone, silty limestone, and shale. The Bonanza King Formation (Enbk) is predominately dolostone and correlates locally with the Highland Peak Formation. The Carrara Formation (Enc) is comprised of limestone, siltstone, sandstone, and shale, while the Wood Canyon Formation (Enzw) is quartzite sandstone, siltstone, shale and sandy shale. The only Precambrian map unit in the DNWR is Stirling Quartzite (Zs), a conglomeratic quartzite and sandstone with minor beds of sandy shale and siltstone.

From west to east the ranges include small portions of the Desert Range in the southwest and the Pahrnagat Range in the northwest, the East Desert Range, Sheep Range, and the Las Vegas Range (Figure 2). Drainages in the DNWR typically drain into the Las Vegas Wash or the Pahrnagat Wash, to the south and east respectively, and then to the Colorado River. Drainages from the western portion of the Sheep Range drain into

Desert Lake, a typically dry playa in Desert Valley, in the northwest portion of the area of interest (Tingley et al., 1993). Alluvial and pluvial valleys are at elevations between 1.2-1.5 km, and the ranges have a maximum relief of approximately 3 km. The ranges show relief between 0.6 km at Saddle Mountain in the East Desert Range and 1.5 km at Hayford Peak in the Sheep Range (Tingley et al., 1993).

The Desert Range, East Desert Range, and Sheep Range are predominantly comprised of Middle Cambrian and Middle Devonian carbonate rocks with local clastic units. Late Devonian, Mississippian, and Permian rocks crop out more extensively to the south (Figure 2 and Figure 3). They are predominantly limestone, local chert, and minor interbeds of shale and quartzite (Tingley et al., 1993; Longwell et al, 1965; Tschanz and Pampeyan, 1970; Page et al., 2005). In the Las Vegas Range, younger Pennsylvanian and Permian units crop out below the Gass Peak thrust fault. Tertiary volcanic units typically crop out where a portion of the Pahranaagat Range is within the DNWR boundaries and to the east and north east of the Sheep Range near the Lake Mine area.

The ranges of the DNWR have undergone two major periods of deformation: thrust faulting, primarily related to the Mesozoic Sevier orogeny, and extensional faulting during the Eocene through Pliocene (Tingley et al., 1993). The only regionally extensive thrust fault of Sevier age within the DNWR is the Gass Peak thrust along the western portion of the Las Vegas Range (Figure 2) (Tingley et al., 1993). The Gass Peak thrust places Precambrian through Ordovician rocks over Devonian through Permian rocks (Tingley et al., 1993 and Longwell et al., 1965) (Figure 2). At the south end of the Las Vegas Range, near Gass Peak, the trace of the Gass Peak thrust fault is rotated 90 degrees to the west by right-lateral slip along the Las Vegas Valley shear zone (Figure 2), a large

magnitude (about 50 km) strike-slip fault zone most active between 14 and 8.5 Ma (Rowley, 1998, Longwell, 1974 and Duebendorfer and Black, 1992). In the northern Las Vegas Range the trace of the Gass Peak thrust fault strikes north for about 20 km where units are buried under alluvium and may extend further to the north and correlate with thrust exposures in the northeastern margin of the Sheep Range (Tingley et al, 1993, Longwell et al, 1965, Wernicke et al., 1984, Page et al., 2005). North of the Sheep Range and south of the Pahrnagat Range the Maynard Lake fault strikes east-north-east and has been active within the last 130 ka (Anderson, and compiler, 1999). Other Tertiary extensional structures in the DNWR include range bounding and intra-range, north-north west trending normal faults, the most extensive of these can be seen along the east side of Sheep Range.

2.2 History of DNWR

A 1936 executive order established the DNWR to preserve the desert bighorn sheep population (U.S. Fish and Wildlife Service, 2005). The order withdrew approximately 3,000 km² from mineral entry (Tingley et al., 1993). This closed the refuge, including the Gass Peak Zn-Pb-Cu-Ag mining district (Figure 4), to mineral exploration and development and placed administration at the direction of the U.S. Department of the Interior (Longwell et al., 1965 and Tingley et al., 1993). Currently the DNWR is managed at the direction of the U.S. Fish and Wildlife Service (U.S. Fish and Wildlife Service, 2005). In 1988 congress passed 43 U.S.C. 1714 (2009), which requires a third party mineral assessment be performed every 20 years on all federal lands closed to mineral entry and larger than five thousand acres (Tingley et al., 1993). The Nevada

Bureau of Mines and Geology (NBMG) were contracted in 1992 to conduct the first mineral assessment, which was carried out by Tingley and others between 1992 and 1993 (Tingley et al., 1993). The assessment by Tingley et al., 1993 was thorough and utilized available geologic data along with remote sensing imagery to guide extensive geochemical sampling of all known mines, prospects, and areas of potential mineralization (Figure 4) (Tingley et al., 1993).

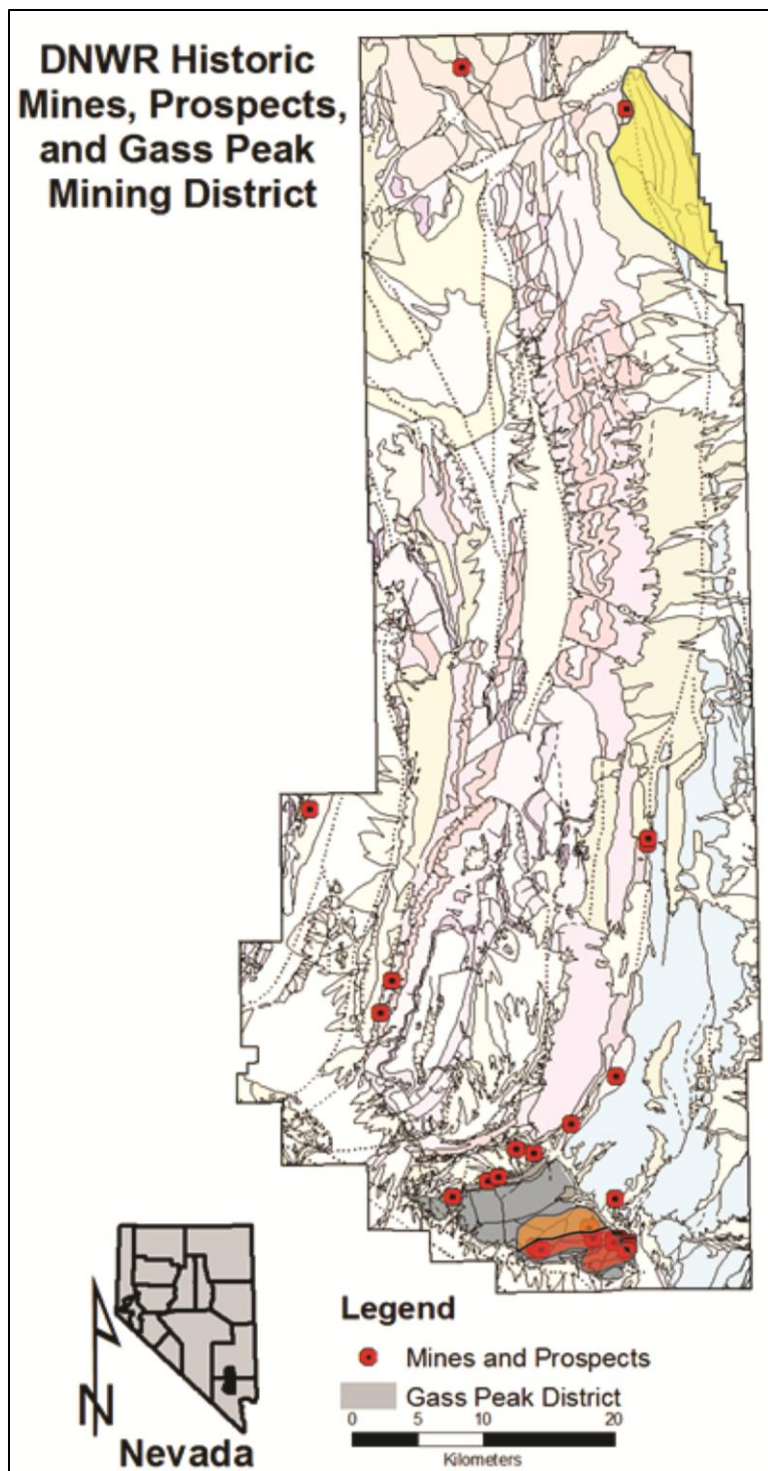


FIGURE 4: DNWR AOI Map showing the location of the Gass Peak mining district and known mines and prospects as identified by Tingley et al., 1993. Moderate potential for base metal deposits are shown in yellow and high potential zones shown in orange and red. Geologic background from Page et al. (2005). Mineral potential zones from Tingley et al. (1993).

2.3 Previous work

The Nevada Bureau of Mines and Geology (NBMG) was contracted in 1992 to conduct the first mineral assessment, which was carried out by Tingley and others between 1992 and 1993 (Tingley et al., 1993). The assessment by Tingley et al., (1993) was thorough and utilized available geologic data along with remote sensing imagery to guide extensive geochemical sampling of all known mines, prospects, and areas of potential mineralization (Figure 4) (Tingley et al., 1993). Extensive data were compiled, including remote sensing, geochemical sampling, and field mapping studies. Ultimately the study concluded that no commercially exploitable mineral resources were present within the area of interest; however, a few areas of low potential for mineral resources were identified through the studies summarized below (Tingley et al., 1993).

The geochemical evaluation of the area included a review of previous geochemical work performed during the National Uranium Resource Evaluation Program and the development of four new geochemical data sets: unmineralized background, high grade samples from known mineralized areas, limonite chips, and stream sediment samples.

The remote sensing study performed over the DNWR during the assessment used Landsat TM (Thematic Mapper) data. The intent was to determine the location and extent of geologic units, structures (mainly lineaments), and to identify mineralized or altered sites that may warrant field investigation. At the time the Landsat TM data was the best readily available data set. Table 1 shows the spatial and spectral resolution of the sensor. During processing, bands 5 and 7 were first evaluated individually then as false color composite images by combining bands 5, 4, 1 or 2 RGB (red, green, and blue),

bands 7, 5, 2 RGB, and band ratio composites 5/7, 3/1, 1 and 5/7, 3/1, 5/4 RGB (Tingley, 1993). Several enhancement techniques were utilized including linear histogram stretching and deconvolution filtering as well as other radiometric, geometric and multispectral enhancements, which helped to delineate hydrothermally altered and mineralized areas and highlight lithologic and structural features (Tingley, 1993). Most of the regions identified were associated with known areas of mineral exploration and activity (Figure 4). The Gass Peak area in the southern portion of the Las Vegas Range is the only notable alteration detected with Landsat TM by Tingley and others (1993). The remote sensing lineament study of the DNWR also helped guide field work toward structural intersections, which may have been favorable for hydrothermal fluid flow. Ultimately the 1992-1993 study identified 3 locations of “moderate to high potential” for base metal deposits (Tingley et al., 1993) (Figure 4).

TABLE 1: Landsat TM spectral and spatial resolution. *TM Band 6 was acquired at 120-meter resolution but products were resampled to 60-meter. (Modified from www.landsat.usgs.gov).

Landsat Thematic Mapper (TM)	Band	Wavelength (Micrometers)	Resolution (meters)
	Band 1	0.45-0.52	30
	Band 2	0.52-0.60	30
	Band 3	0.63-0.69	30
	Band 4	0.76-0.90	30
	Band 5	1.55-1.75	30
	Band 6	10.40-12.50	120* (30)
	Band 7	2.08-2.35	30

2.4 Spectroscopy

Spectroscopy is the study of the interaction between radiated energy, such as the sun or other energy source, and the intrinsic properties of matter (Crouch et al., 2007). Spectral data are typically presented as an XY linear plot of wavelength versus intensity of response. Spectrometers are the sensors used to measure and collect spectral data, which is then compiled into a spectral library. Computer software is used for comparative analysis and identification of spectra between the spectrometer collected data and reference libraries such as those found in the ASTER Spectral Library 2.0 (Baldrige, et al., 2009). Such reference libraries have been generated with spectra collected by the United States Geologic Survey (USGS) and Jet Propulsion Labs (JPL) on known samples identified by other analytical methods.

Figure 5 highlights the difference in spectral resolution between laboratory spectroscopy and remote sensing imagery. The first has a high spectral resolution, but no image detail while the second is an imager that acquires a few 10s of broad spectral bands. In both cases the spectra are a function of absorption and scattering patterns, which occur as photons interact with all matter encountered between the object and the sensor (Clark, 1999).

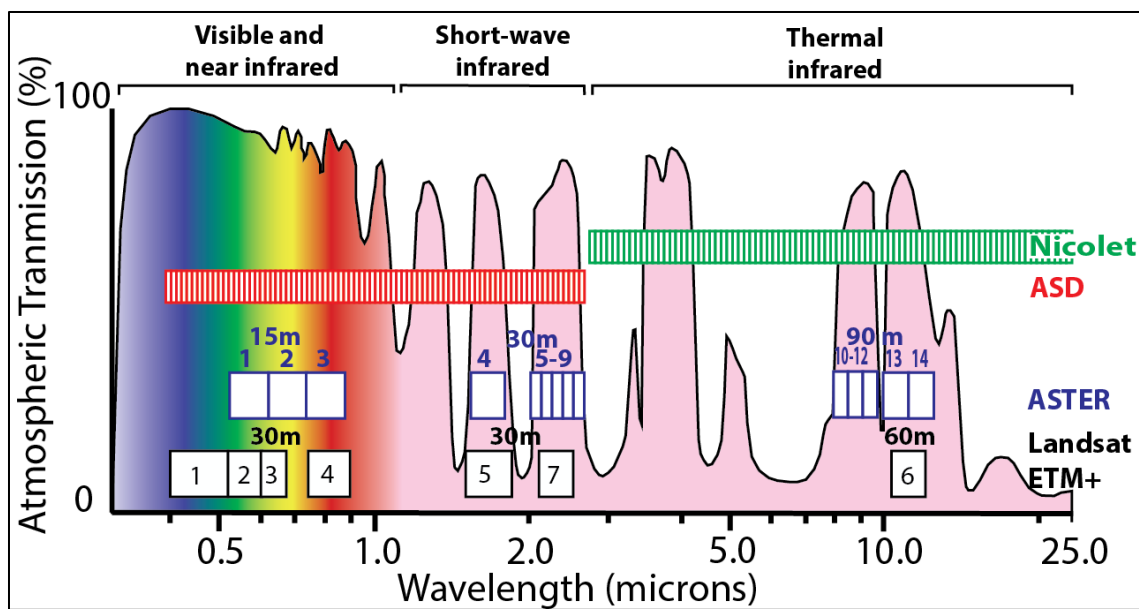


FIGURE 5: Portion of the electro-magnetic spectrum between 0.3-25.0 microns showing spectral band passes of remote sensing instrumentation. Lows in the background curve represent relative signal degradation resulting from H₂O and CO₂ interference with the spectral transmission through the atmosphere. Thermo Nicolet and ASD Terraspec are laboratory hyper-spectral spectrometers with continuous high resolution sampling in the representative intervals shown above. Landsat ETM+ and ASTER bands are shown at their designated full width half maximum resolution on the above figure. (Modified from Kabb et al., 2002 and Kaab 2005).

Spectral absorbance features can arise from either electronic or vibrational interactions between photons and matter. Electronic features are typically measured in the visual-near infrared (VNIR) and short-wave infrared (SWIR) (Fig 5) and are a combination of crystal field effects, charge transfer, conduction bands (band gaps) and color centers (Clark, 1999). Some minerals with spectral signatures most affected by electronic absorption features include iron oxides, native sulfur, cinnabar and fluorite. These absorption features result from electron transitions, which occur as electrons move between excited energy states and their ground state (Clark, 1999). Absorption features in the VNIR and SWIR portion of the electromagnetic spectrum are measured in % reflectance and occur between 0.4 and 2.5 micrometers (microns).

Vibrational spectral features are most prominent in the thermal infrared (TIR) wavelengths of EM spectrum, though overtones from fundamental vibrations can be observed in the SWIR portion of the EM spectrum. Vibrational processes affecting absorption include asymmetrical and symmetrical stretching and bending of molecules, and the deformation of lattice modes in molecules with dipole moments such as, silicate minerals, water, hydroxyl, carbonates, as well as phosphates, borates, arsenates and vanadates. The TIR portion of the electromagnetic spectrum is typically measured using relative emissivity between 2.5 and 1000 microns (1mm). Emissivity is a measure of thermal radiation and is related to reflectance by Kirschoff's Law:

$$E = \alpha = 1 - R$$

where "E" is emissivity, " α " is absorbance, and "R" is reflectance (Clark, 1999).

2.4.1 Laboratory Spectroscopy

Spectrometry performed in the laboratory utilizes instruments, which collect high resolution spectral data over a typically small, discrete area utilizing internal radiant energy sources. In the case of spectral geology, this allows specific minerals in a sample to be targeted and identified. Laboratory spectrometers are typically comprised of hundreds to thousands of "bands" or "channels", each channel measuring a narrow, discrete portion of the EM spectrum. The high spectral resolution results in near continuous data collection across the measured interval. This provides the data needed to make positive mineral identifications based solely on spectral data. Furthermore, detailed spectral analysis and study can reveal unique details regarding the crystal form of the sample, providing insight into the formation conditions such as temperature and pressure.

2.4.2 Remote Sensing Imagery

Remote sensing spectrometry relies on the same principles as laboratory spectrometry; however, instead of a discrete spot analysis of a sample with high spatial and spectral resolution the sensor is either mounted to an airplane or satellite and typically uses the sun as the radiated energy source. These sensors collect data anywhere from tens of meters (airborne) up to several hundred kilometers (spaceborne) above the targeted area on Earth. To facilitate processing of this data, georeferenced pixels are collected into scenes. The size of each pixel is a function of the sensors engineering and the altitude at which the data was collected. Typically, pixels in remotely sensed images range in size from 3-15 m for airborne sensors to 15-90 m or greater for spaceborne sensors. The result is that each pixel contains some combination of the spectra for all exposed material in the pixel. Through image processing the primary constituents of the pixel can be identified. Each pixel is comprised of all the data for each of the sensor's bands. This study utilizes only spaceborne remote sensing platforms, which due to payload and budget restrictions, have been engineered as multi-spectral sensors, meaning the 7 bands of Landsat ETM+ or the 14 bands of ASTER must serve as a proxy for the hundreds and thousands of bands typically used in airborne remote sensing and laboratory settings respectively. Additionally, the interference of atmospheric water between the surface of the Earth and the sensors results in restrictive narrow "windows" of wavelengths through which the EM spectrum can be effectively monitored remotely (Figure 5). Limited spectral windows, reduced spectral resolution, and reduced spatial resolution (resulting in spectral mixing within pixels) are some of the challenges that must be overcome when processing remotely sensed images.

2.5 Remote Sensing Instruments

2.5.1 Landsat ETM+

Landsat ETM+ was launched April, 1999 as part of the Landsat data continuity mission (DCM). The Landsat ETM+ sensor collects images or scenes comprised of 7 spectral bands covering an approximate area of 170 km X 183 km (Table 2) (Figure 6).

Table 2 - Landsat ETM+ spectral and spatial characteristics.

Landsat ETM+			
Band	Band Pass	Band Center	Spatial Resolution
1	0.45-0.52	0.485	30m
2	0.52-0.6	0.560	30m
3	0.63-0.69	0.660	30m
4	0.76-0.9	0.830	30m
5	1.55-1.75	1.650	30m
6	10.4-12.5	11.450	60m
7	2.08-2.35	2.215	30m

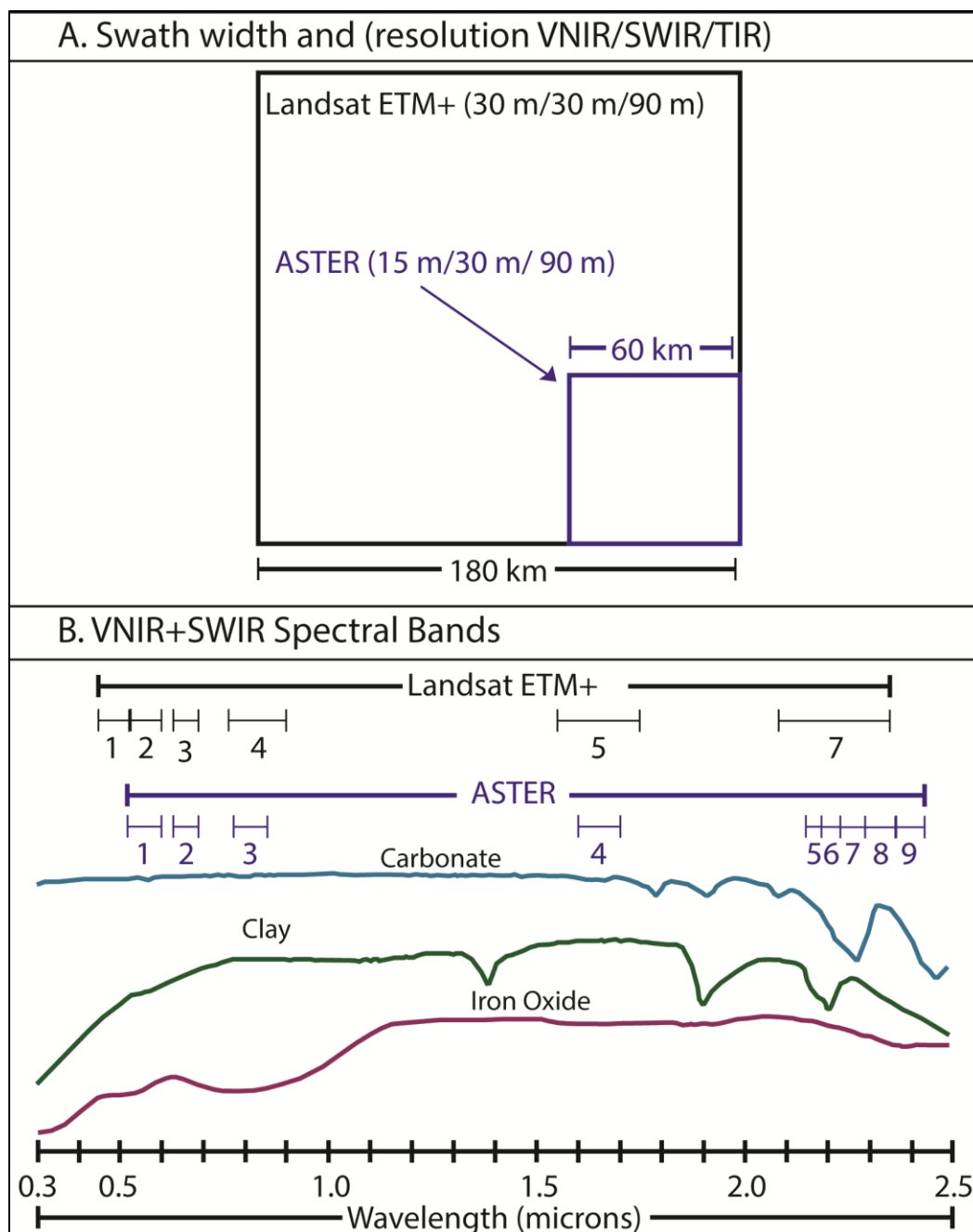


Figure 6: Comparison of Landsat ETM+ and ASTER spectral and spatial characteristics. A. Swath width and (VNIR spatial resolution). B. VNIR and SWIR spectral band passes and USGS reference end members (Modified from Rowan et al., 2003).

In summer of 2013 a new Landsat Data Continuity Mission (LDCM) was brought online and available to the public, Landsat 8: Operational Land Imager (Landsat OLI).

This satellite has three more bands than Landsat ETM+, which are located in the VNIR, SWIR and TIR. The added band in the VNIR is specialized to monitor coastal aerosols and the new SWIR band is designed for cirrus cloud detection, neither of which aid in the mineral mapping. The additional TIR band has a spatial resolution of 100 m and will be delivered as a single band combining data from the two TIR bands; this will highlight surface temperature differences. Although the additional data included in the TIR band of Landsat OLI may be of slight interest to this project, its reduced spatial resolution and the improved spectral and spatial resolution of the ASTER dataset makes using the new Landsat OLI data redundant and unnecessary. Additional considerations in excluding this data set included the lack of existing preprocessing utilities in the software, and the increased possibility of error when applying existing methods to slightly modified data sets. It is more practical to utilize the pre-existing and established Landsat ETM+ tools until processing methods for Landsat 8 have been better established and incorporated into the software.

2.5.2 ASTER

ASTER collects images comprised of 14 spectral bands (Table 3) over a 60 km by 60 km area (Figure 5 and Figure 6). The instrument collects data in the visual-near infrared (VNIR), short-wave infrared (SWIR), and thermal infrared (TIR) regions of the electromagnetic spectrum, from 0.52-11.650 microns, at the spatial and spectral resolutions shown in Table 3 and have acquired data over most of the Earth's land surface.

Table 3 - ASTER spectral and spatial characteristics

ASTER			
Band	Band Pass	Band Center	Spatial Resolution
1	0.520-0.600	0.560	15m
2	0.630-0.690	0.660	15m
3	0.780-0.860	0.820	15m
4	1.600-1.700	1.652	30m
5	2.145-2.185	2.164	30m
6	2.185-2.225	2.204	30m
7	2.235-2.285	2.259	30m
8	2.295-2.365	2.329	30m
9	2.360-2.430	2.394	30m
10	8.125-8.475	8.300	90m
11	8.475-8.825	8.650	90m
12	8.925-9.275	9.100	90m
13	10.250-10.950	10.600	90m
14	10.950-11.650	11.300	90m

2.6 Remote Mapping of Geology and Hydrothermal Alteration

As discussed above, both Landsat ETM+ and ASTER instruments have been configured to collect data in the wavelengths most useful for Earth observations, avoiding regions of the electromagnetic spectrum where atmospheric water and CO₂ degrade the signal beyond use (Figure 5). Table 4 summarizes a variety of processing methods used to map lithology and alteration. Landsat ETM+ and its predecessors have been most successful at mapping lithology, alteration, and structural features (Van der Meer et al., 2012; Ashley and Abrams, 1980 and others). Band ratio techniques and principal component analyses are some of the most commonly and successfully used tools for mineral and lithology mapping using multispectral remote sensing platforms such as Landsat platform and ASTER images (Table 4) (Sabins, 1999; Van der Meer et al., 2012; Rowan et al., 2003; Hewson et al., 2001 and others).

Table 4: Defining algorithms and processes used in an ASTER and Landsat ETM+. (Modified from Pour and Hashim, 2012)

Algorithm	Reference	Description
Principal Component Analysis (PCA)	Singh and Harrison (1985)	Principal Component (PCA) is a multivariate statistical technique that selects uncorrelated linear combination (eigenvector loadings) of variables in such a way that each component successively extracted linear combination and has a smaller variance.
Minimum Noise Fraction (MNF)	Green et al. (1988); Boardman et al. (1998)	Minimum Noise Fraction (MNF) transformation is used to determine the inherent dimensionality of image data, segregate noise in the data and reduce the computational requirements for subsequent processing.
Band ratio, Relative Absorption Band Depth (RBD), and mineral indices	Rowan et al. (1977); Goetz et al. (1983); Sabins (1987); Crowley et al. 1989); Ninomiya (2003a, 2003b); Mars and Rowan (2006)	Band ratio is a technique where the digital number value of one band is divided by the digital number value of another band. Band ratios are very useful for highlighting certain features or materials that cannot be seen in the raw bands. Relative Absorption Band Depth (RBD) is a useful three-point ratio formulation for detecting diagnostic mineral absorption features. For each absorption feature, the numerator is the sum of the bands representing the shoulders, and the denominator is the band located nearest the absorption feature minimum. Mineral indices for ASTER VNIR+SWIR and TIR set thresholds on well tested band ratio combinations in an attempt to isolate pixels dominated by a specific mineral or mineral group.
Spectral Angle Mapper (SAM)	Kruse et al. (1993)	The Spectral Angle Mapper (SAM) technique measures the spectral similarity by calculating the angle between the two spectra and treating them as vectors in n-dimensional space.
Linear Spectral Unmixing (LSU)	Boardman (1993); Adams et al. (1993)	Linear Spectral Unmixing (LSU) is known as sub-pixel sampling, the reflectance at each pixel of the image is assumed to be a linear combination of the reflectance of each material (or end-member) present within the pixel.
Matched-Filtering (MF)	Harsanyi et al. (1994); Boardman et al. (1995)	The Matched-Filtering (MF) algorithm performs a partial unmixing of spectra to estimate the abundance of user-defined end-members from a set of reference spectra. This technique maximizes the response of the known end-member and suppresses the response of the composite unknown background, thus matching the known signature.
Mixture-Tuned Matched-Filtering (MTMF)	Boardman et al. (1995); Boardman (1998)	Mixture-Tuned Matched-Filtering (MTMF) technique is a combination of the Linear Spectral Unmixing technique and the statistical Matched Filtering model. From MF it inherits the advantage of its ability to map a single known target without knowing the other background end-member signatures, unlike traditional Spectra Mixture modeling. From the Spectral Mixture modeling it inherits the leverage arising from the mixed pixel model, the constraints on feasibility including the unit-sum and positivity requirements, unlike the MF which does not employ these fundamental facts. As a result MTMF can outperform either method, especially in case of subtle, sub-pixel occurrences.

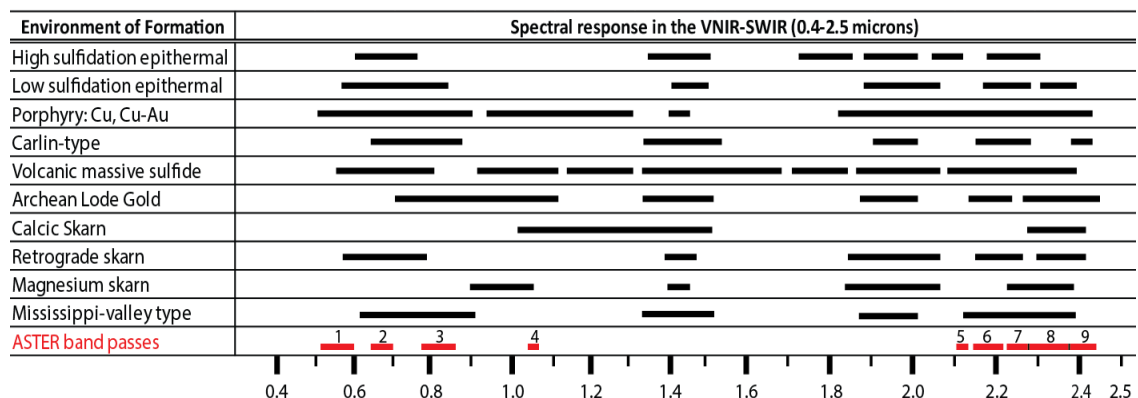
The additional bands in the ASTER data have allowed mineral indices to be developed. The indices target more specific minerals, mineral groups, and lithologies than the broad “alteration” indices used with Landsat data sets. With additional processing these indices can provide more quantitative and reliable mineral distribution mapping than was possible using Landsat datasets (Ninomiya, 2003a; Oskouei and Busch, 2012; Watanabe and Kazuaki, 2003; Rowan et al., 2006 and others).

The VNIR and SWIR portions of the EM spectrum play a key role in the identification and mapping of alteration and mineralization environments as well as the associated unaltered host rocks. Table 5 summarizes hydrothermal ore-forming environments and the spectrally active minerals associated with them. Table 6 shows the VNIR-SWIR portion of the EM spectra, which could be used to identify the minerals presented in Table 4.

Table 5: Summary of some ore-forming environments and their associated spectrally active alteration minerals (Modified from Van der Meer et al., 2012; Guilbert and Park 2007; Thompson et al., 1999).

Environment of formation	Main spectrally active alteration minerals
High sulfidation epithermal	Alunite, pyrophyllite, dickite, kaolinite, diaspore, zunyite, smectite, illite, calcite, chlorite, epidote, sericite, clay
Low sulfidation epithermal	Sericite, illite, smectite, kaolinite, chalcedony, opal, montmorillonite, calcite, dolomite, alunite, chlorite, kaolinite, christobalite, jarosite
Porphyry: Cu, Cu-Au	Biotite, anhydrite, chlorite, epidote, muscovite, pyrophyllite, zeolite, smectite, carbonate, tourmaline, sericite, actinolite, clinopyroxene, scapolite, kaolinite, pyrophyllite, alunite, topaz, zunyite
Carlin-type	Illite, dickite, kaolinite
Volcanic massive sulfide	Sericite, chlorite, chloritoid, sericite, biotite, carbonates, siderite, anhydrite, gypsum, amphibole, ankerite
Archean Lode-Gold	Carbonate, talc, tremolite, muscovite, paragonite
Calcic skarn	Garnet, clinopyroxene, wollastonite, actinolite vesuvianite, serpentinite-talc, calcite, illite, smectite, nontronite
Retrograde skarn	Calcite, chlorite, hematite, illite
Magnesium skarn	Fosterite, serpentine-talc, magnetite, calcite
Mississippi-Valley-Type (carbonate replacement)	Carbonates, calcite, dolomite, marcasite, smithsonite, jarosite, limonite, alunite

Table 6: Summary of ore-forming environments and the spectral response of minerals commonly associated with them. Modified from Van der Meer et al. (2012).



The TIR portion of the EM spectrum also plays an important role in the identification of lithologies and alteration associated with hydrothermal mineralization. Laboratory spectrometry in the TIR spectrum allows the identification of a variety minerals and lithologies; however the limited ASTER band passes only allow a few generalized band ratios and mineral indices to be effective. Ninoyima (2003B) and Ninoyima and Fu (2001) present carbonate and silica indexes and a “basic degree index” respectively. The basic degree index has been developed to identify exoskarn silicate minerals such as garnet, pyroxene, and epidote. Although somewhat limiting, these three band ratios/indexes provide sufficient data to discriminate between silica rich alteration and rock, and unaltered carbonate hosts; making them ideal for mapping silicates in skarn zones and other carbonate hosted mineral deposits with silicate mineral assemblages.

2.7 Hydrothermal Ore Deposits in Nevada

With respect to mineral deposits, Nevada is the most well-endowed state in the United States. 2013 marked the third straight year that Nevada led the nation for non-fuel

mineral production, producing minerals valued at \$9.04 billion (USGS Minerals Commodities Summary, 2013). Much of that value was generated from gold production. Nevada is a world leader in gold production, in 2012 it was ranked fourth largest producer behind China, Australia, and Russia (NBMG Mineral Industry Report 2012). Additionally, Nevada produces a significant amount of copper, silver, and molybdenum (NBMG Mineral Industry Report 2012).

Most of the metals mined in Nevada are produced from hydrothermal ore deposits, typically located in the northern half of the state. Bulk tonnage, sub-micron, sediment hosted Carlin-type gold deposits, which mainly occur in lower Paleozoic carbonate rocks, account for most of the gold produced in Nevada; though Cenozoic volcanic rocks hosting epithermal gold-silver deposits are also common. Intrusion related deposits such as porphyry, skarn, and polymetallic vein and replacement deposits host gold, copper, molybdenum, tungsten, silver, lead, and zinc ore adjacent to Mesozoic and Cenozoic intrusive rocks. These three mineral deposit types: 1) Carlin-type deposits, 2) epithermal deposits, and 3) intrusion related deposits are broad deposit classes, which account for the bulk of the dollar value mined from mineral deposits in Nevada. Models for these 3 classes of deposits are discussed below. In addition to the deposits mentioned above, base metal, (lead and zinc dominated), carbonate -hosted Mississippi Valley type (MVT) deposits, are hosted mainly in middle Paleozoic carbonate rocks in southern Nevada. Figure 7 below shows the distribution of a variety of Nevada mineral deposits with respect to physiographic features and the area of interest.

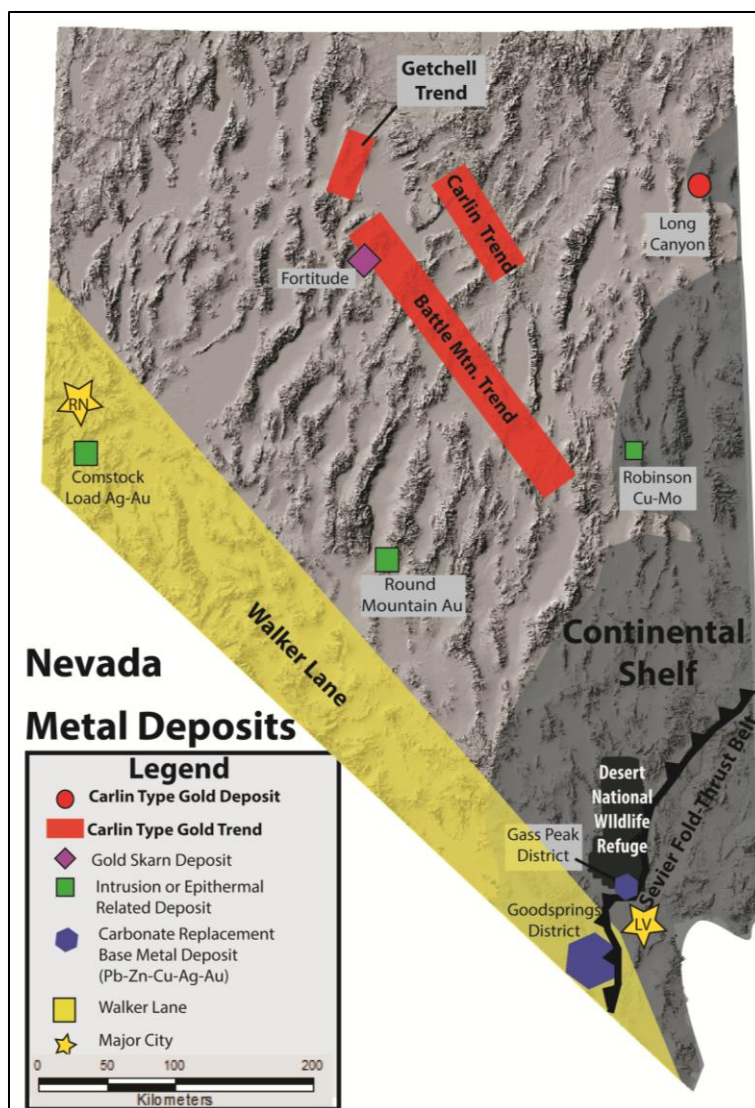


FIGURE 7: Mineral deposits of Nevada and the depositional and structural setting of the DNWR. (Modified from Long, 2012 and Schilling, 1968).

2.7.1 Carlin-Type Deposits

Carlin-type gold deposits (CTD) occur mainly in northern Nevada along large (50-200 km), often range cutting, northwest to slightly east of north trending belts such as the Getchell, Carlin and Battle Mountain trends (Figure 7). Long Canyon represents a recently discovered CTD, not associated with any currently identified mineral belts or trends and is uniquely located on the continental shelf (Figure 7). Carlin-type deposits are

bulk tonnage gold deposits characterized by regional ore systems that are hosted in predominantly carbonate rock that have undergone multiple stages of compression and extension, which structurally prepare the host rocks for hydrothermal activity, which often concentrates ore along folds and high-angle faults. Ore fluids are thought to have evolved from both magmatic and meteoric sources (Cline et al., 2005). Gold deposition has generally been thought to have occurred during the late Eocene (Hofstra et al., 1999; Arehart et al., 2003). In unweathered ore, gold occurs mainly in the atomic structure of arsenian pyrite in Paleozoic carbonates and mudstones that have been hydrothermally dissolved, silicified, and argillized during the process of ore emplacement. Intersections with Mesozoic granite bodies and intrusive dikes are common. Figure 8 is representative of the original Carlin mine and highlights alteration and zonation commonly associated with these deposits.

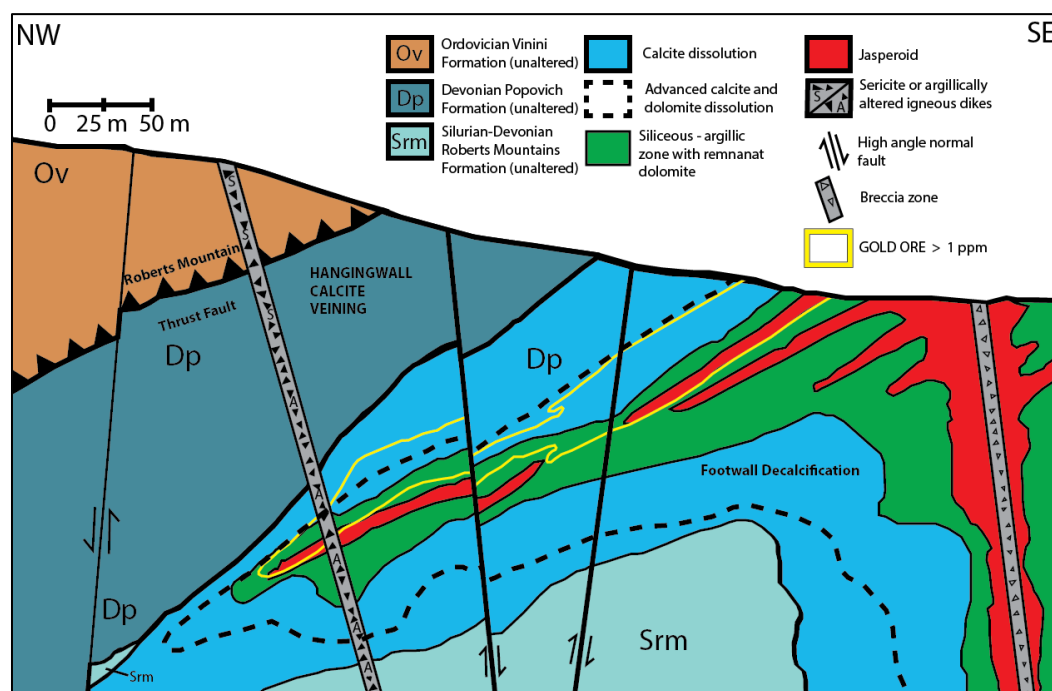


FIGURE 8 – Alteration and zonation of Carlin-type deposits. Modified from Kuehn and Ros (1992) and Cline et al. (2005).

2.7.2 Epithermal and Intrusion Related Deposits

Epithermal gold-silver deposits are another common mineral deposit in Nevada. They are typically hosted by Tertiary volcanic rocks and are associated with veins, stockwork veining and disseminations of ore minerals, Figures 9 and 10 respectively). Typical alteration zonation of high-sulfidation deposits is shown in Figure 9 and for low-sulfidation deposits in Figure 10. Potential relationships between intrusive rocks and epithermal systems are shown in Figure 11. Zoning in high-sulfidation deposits typically zone outward from silicic alteration (quartz + alunite \pm pyrite \pm kaolinite \pm dickite), to clay alteration (kaolinite \pm alunite \pm illite \pm smectite), to more distal propylitic alteration (chlorite \pm albite \pm carbonate \pm epidote \pm sphene), and eventually to fresh rock (Simmons and Browne, 2000). Figure 10 shows a generalized low-sulfidation deposit with common mineral zonation shown in the lower right; note shallow sinter and/or steam heated acid-sulfate alteration (kaolinite \pm alunite, \pm quartz).

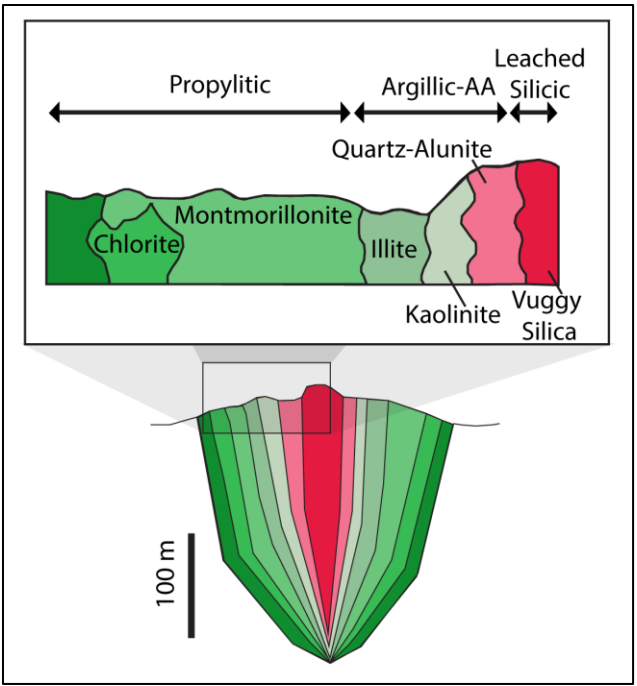


FIGURE 9: Zonation of alteration and mineralization around high sulfidation epithermal systems. AA in the figure is “advanced argillic” alteration. From Steven and Ratte, (1960) and Stoffregen, (1987).

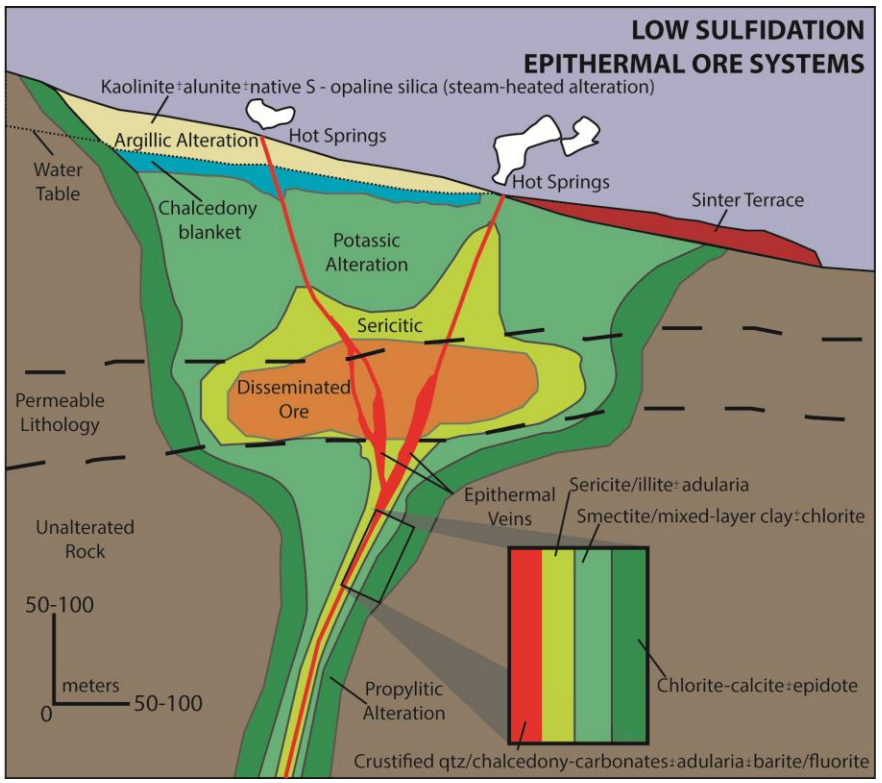


FIGURE 10: Zonation of alteration and mineralization around low sulfidation epithermal systems. Modified from Buchanan, 1981; Sillitoe 1993.

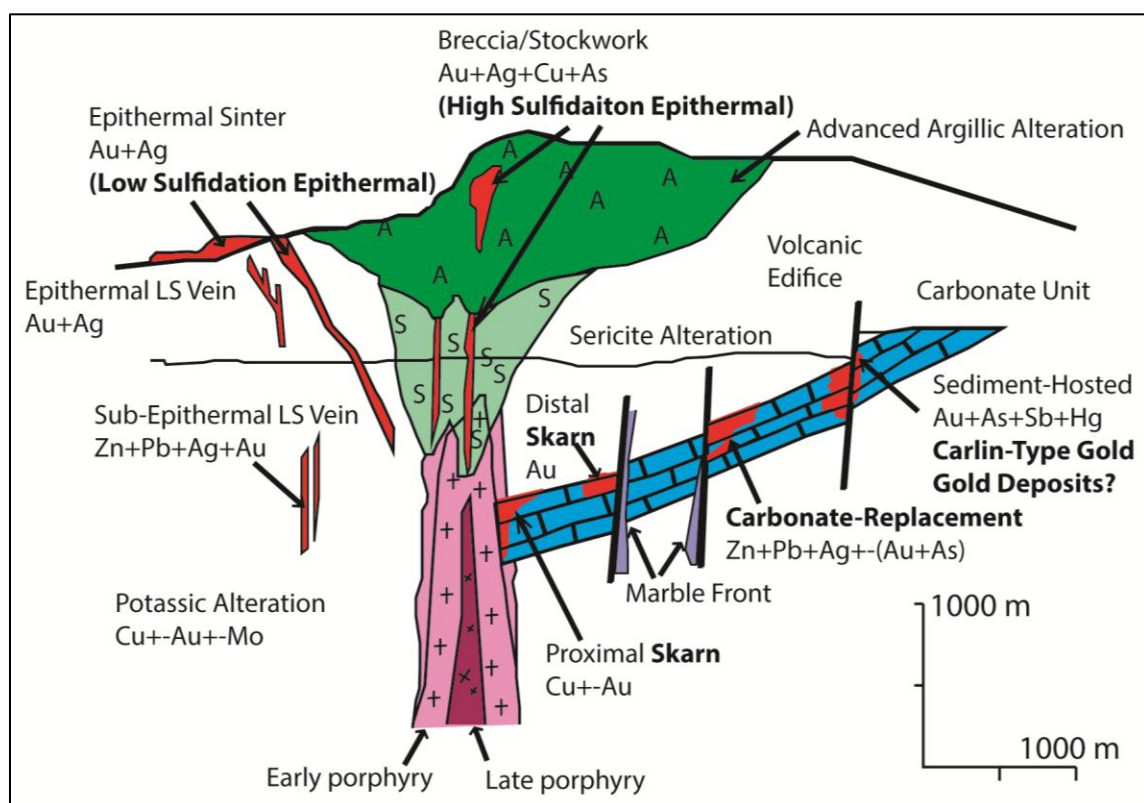


FIGURE 11: Zonation of alteration and mineralization around intrusive rocks (porphyry, skarn, carbonate replacement, Carlin-type deposits) and proximal to extrusive igneous bodies (high and low sulfidation epithermal). Modified from Sillitoe (1996), Sillitoe (2010) and Van der Meer et al. (2012).

As Figure 11 above shows intrusion related mineralization may occur in a similar environment to epithermal deposits, however, they form at a greater depth. Intrusive related deposits generally include Cu-Mo-Au porphyry and Cu-W-Au skarn deposits, though some carbonate-replacement and Carlin-type deposits of Au, Ag, Cu, Pb, and Zn are locally associated intrusions (Simmons et al., 2005). Porphyry deposits typically form at depths greater than 1 km, with hydrothermal alteration typically zoning outward from proximal potassic alteration to sericitic alteration (quartz-sericite-pyrite) to distal propylitic alteration. If carbonate rocks are present, skarn deposits, typically containing garnet and pyroxene, may form proximal to the porphyry intrusion.

2.7.3 Mississippi-Valley Type Deposits

MVT Pb-Zn deposits are only found in a few locations in Nevada, including the Goodsprings district 40 miles southwest of the DNWR and the historic Gass Peak district within the DNWR boundaries (Figure 7). The MVT deposits are formed from basinal brine fluids. Figure 12 shows the distribution of historically producing metallic mineral deposits in southern Nevada (Muntean et al., 2014). Alteration of MVT deposits is characterized by hydrothermal dolomite replacement of limestone. This represents the extent of the potential mineralization and locally hosts minable ore deposits (Figure 13).

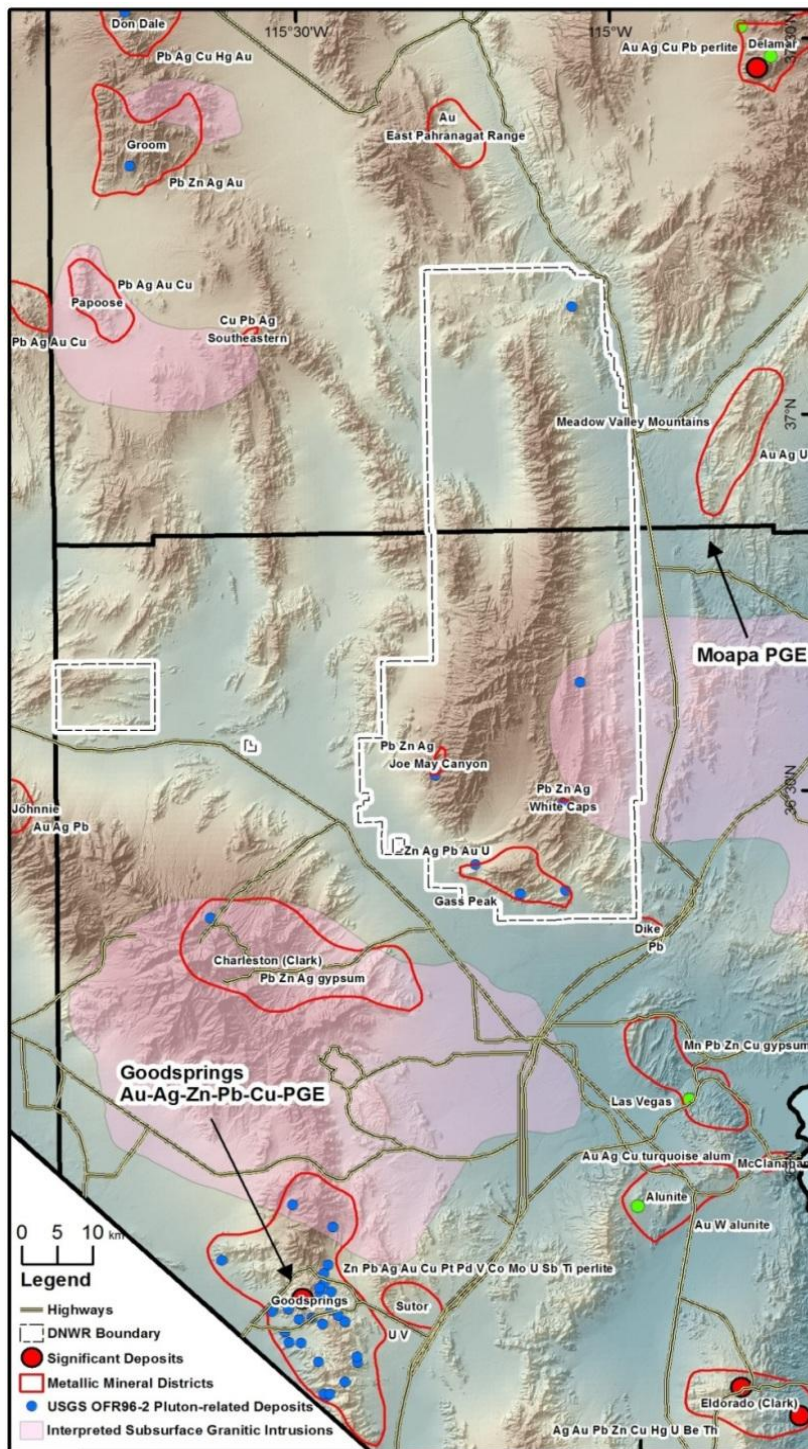


FIGURE 12: Study area relative to the Goodspring district to the southwest and other proximal mineral occurrences. (From Muntean et al., 2014)

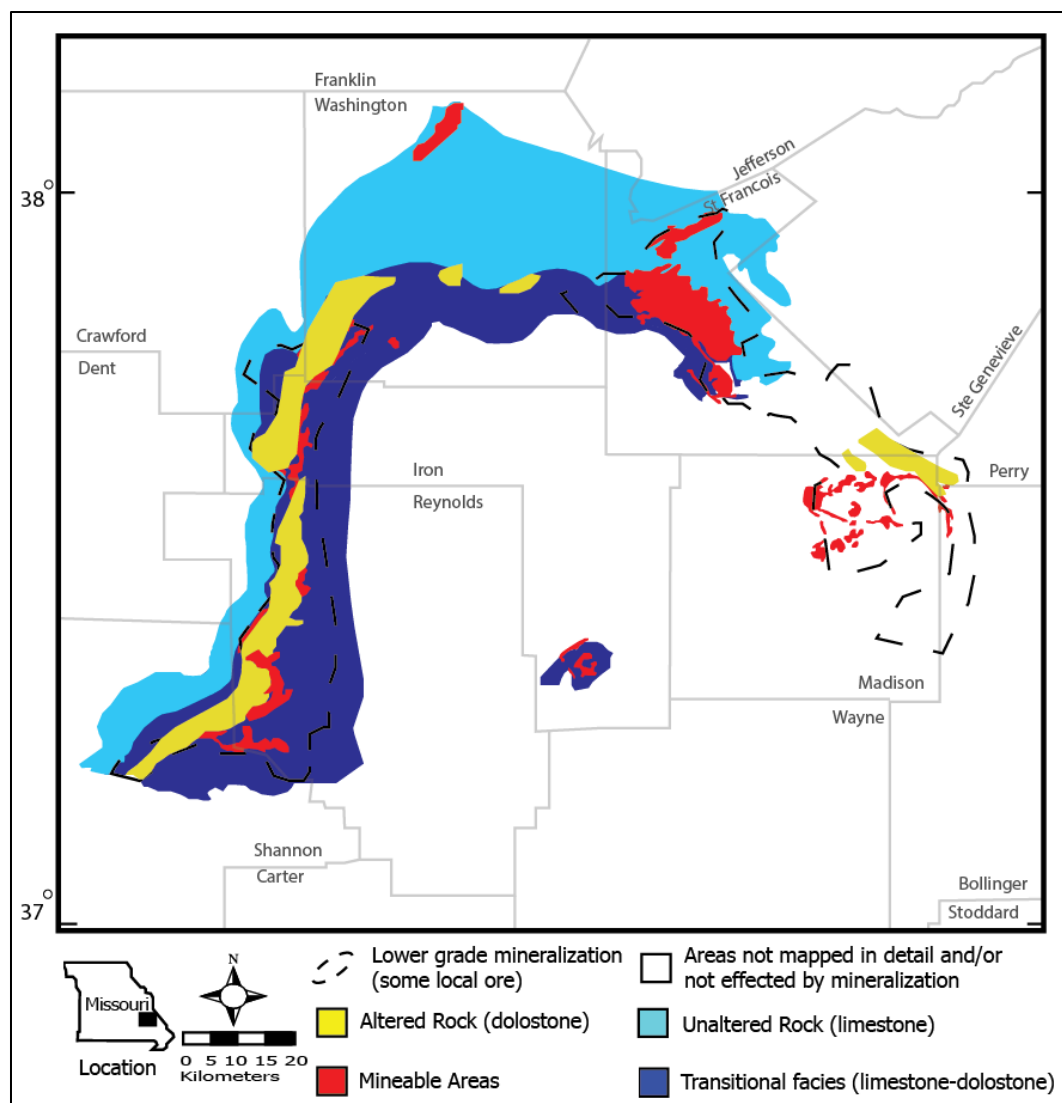


FIGURE 13: Zonation associated with MVT deposits, highlighting the extent of dolomitization vs. unaltered limestone and local mineral endowment within the dolomitized regions. (Modified from Leach et al., 2010).

The Goodsprings district is the largest of the deposits shown in Figure 12. The district comprises a complex group of mineralized deposits, hosted in Mississippian-Permian limestone and Late Proterozoic-Early Cambrian limestone and dolomite. It contains a variety of precious and base metal deposits. Gold, silver, copper, lead, zinc and platinum group elements (PGE) are all found within the district in a variety of combinations and concentrations (Vikre et al., 2011). The zinc-dominant carbonate

replacement deposits in the district are thought to be older and show similarities to MVT deposits (Vikre et al., 2011), and are thought to have formed during the Late Paleozoic (Vikre et al., 2011 and Hewett, 1931). Other deposits in the district, which are more lead-rich are spatially associated with Late Triassic feldspar porphyry dikes and are thought to be related to feldspar porphyry intrusions of similar ages. The deposits in the Goodsprings district are generally lead dominant with lesser copper \pm precious metal-PGE, and gold \pm silver deposits.

The Goodsprings district is spatially smaller than the world-class Viburnum Trend of MVT deposits in southeast Missouri (Figure 13), which hosts large scale hydrothermal dolomitization (10-100 km wide) which encompass the ore bodies on Viburnum Trend. In contrast, the Gass Peak district is much smaller, less than 100 sq. km in area, with only a few mine claims and prospects that produced lead, zinc, and minor amounts of silver. Table 5 and Table 6 display the minerals some of which may be detected using the methods described below.

3.0 Methods

3.1 Data Acquisition and Computer Software

Landsat ETM+ and ASTER images are selected based on availability of cloud free imagery, image quality, and timing of acquisition (NASA Land Processes Distributed Archive Center). All images were initially viewed and selected via www.earthexplorer.usgs.gov. Landsat ETM+ data was downloaded directly from the USGS earthexplorer website and preprocessed using ENVI software routines, which performed atmospheric correction and converted radiance data to reflectance products.

Atmospherically corrected, reflectance (VNIR and SWIR) and at-surface-radiance (TIR) ASTER images were purchased and downloaded from <http://gdem.ersdac.jspacesystems.or.jp/>, which provides a standardized atmospheric correction and reflectance or emissivity conversion to the raw image. Both Landsat ETM+ and ASTER images were then processed using a 64 bit PC running Microsoft Windows 7, preloaded with ENVI 5.0 (spectral image processing software). Processed imagery was then compiled with other datasets using ArcGIS 10.0 geographic information system (GIS) software.

Laboratory spectra were collected from field samples using an Analytical Spectra Devices (ASD) TerraSpec Fourier Transform Infrared (FT-IR) spectrometer, which collects spectra in the VNIR and SWIR portions of the electromagnetic spectrum, from 0.350-2.500 microns (2,151 bands total). The ASD TerraSpec has a 3 nm resolution between 0.350 and 0.7 microns, 6-8 nm resolution between 0.7 and 1.4 microns, and 10 nm resolution above 1.4 microns (Figure 5). The ASD TerraSpec samples every nm making the data oversampled with respect to spectral resolving power. Comparative analysis of spectra was performed using SpecWin spectral viewing software and spectral reference libraries from both USGS Spectral Library, which is included in ENVI software (Clark et al., 1993), and the ASTER Spectral Library 2.0 (Baldrige et al., 2013). TIR spectra were collected using a Thermo Scientific Nicolet 6700 FTIR spectrometer, which collects spectra between 2.5 and 25 microns (1,869 bands), TIR samples are analyzed using OMNIC spectral viewing software and the ASTER Spectral Library 2.0 (Baldrige et al, 2009) and USGS Spectral Library (Clark et al., 1993).

3.2 Data Processing

Figure 14 graphically displays the primary steps utilized during the mapping of the 5 main mineral end member classes chosen for the study: iron oxide (includes goethite, jarosite, gossan, and hematite), dolomite, limestone, clay, and silica, which were deemed important in the detection of the various mineral deposits that were most likely to occur in the DNWR. Additional mapping and processing methods, including Matched Tuned Mixed Filter, Spectral Feature Fit, Spectral Information Divergence, Linear Spectral Unmixing, and Multi-Range Spectral Feature Fit, were explored for each of these mineral groups during the course of this study; however, the methods displayed in the Figure 14 represent those that were most effective at producing reliable and useful results.

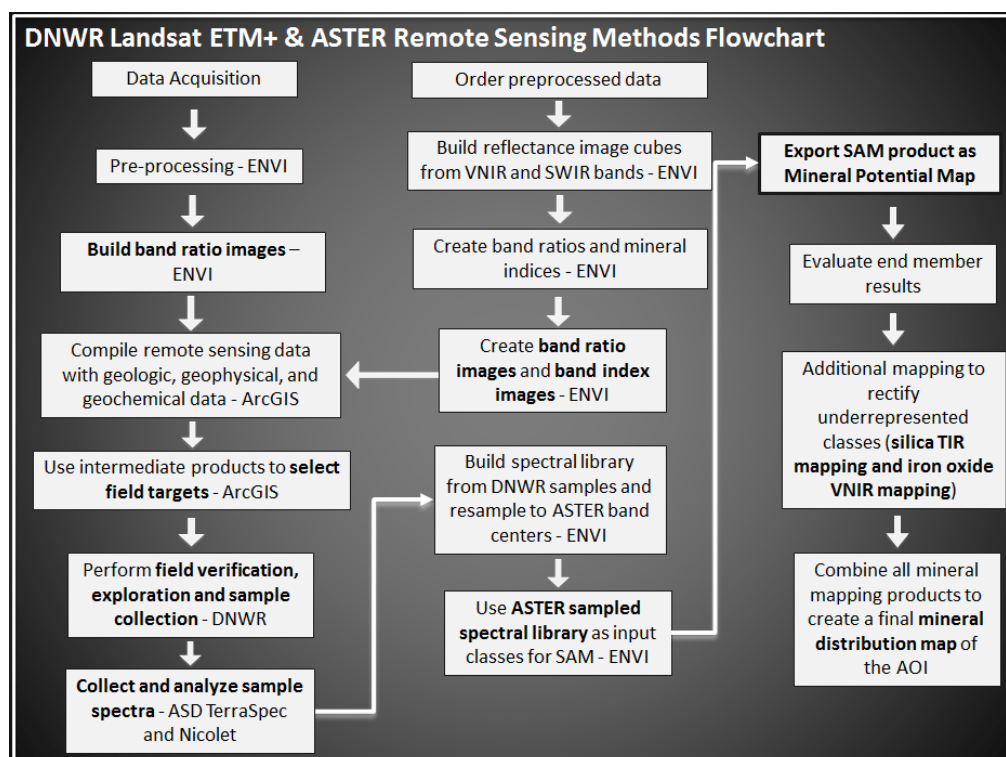


Figure 14: Flow chart generalizing all processing steps from data acquisition to final mineral distribution mapping. Landsat processing on the left ASTER on right.

3.2.1 Landsat ETM+

Four Landsat ETM+ scenes were needed to cover the AOI and were selected based on time of year similarities and the availability of cloud and snow free scenes. To avoid scan line errors resulting from equipment failure only data collected prior to April 2003 was used. The four Landsat ETM+ scenes utilized here are:

- (1) LE70390341999185EDC00 collected July 4th, 1999
- (2) LE70390351999185EDC00 collected July 4th, 1999
- (3) LE70400341999224EDC00 collected August 8th, 1999
- (4) LE70400351999224EDC00 collected August 8th, 1999.

The downloaded radiance data was first converted to reflectance data and atmospherically corrected using ENVI preprocessing algorithms designed specifically for use with Landsat ETM+. Each scene was resized to cover the AOI and mosaicked to reduce processing time. A variety of true and false color composite images were compiled and evaluated during processing and prior to field reconnaissance, utilizing several band ratio combinations to highlight a variety of potential alteration zones (Table 7). The Landsat ETM+ end products utilized band ratios and band ratios combined with principle component stretches to highlight differences in exposed geologic units and alteration where present. Table 7 describes the band ratios utilized and provides a brief description of what each band ratio is intended to highlight.

Table 7: Landsat ETM+ band combinations and false color composite image descriptions. *Images not expressly discussed in the body of this text can be found in Appendix A.

Landsat ETM+ Band Combination Images and Descriptions				
Image #	Red	Green	Blue	Description and/or Source
0	Band 3	Band 2	Band 1	True/Natural Color Image
1	5/7 FeOx/AlOH	3/2 Iron Oxide	4/3 Vegetation	"Abram's Ratio" – Ashley and Abrams (1980)
2	5/7 FeOx/AlOH	4/7 Carbonate Rocks	4/2 Vegetation	Ashley and Abram (1980)
3	5/7 FeOx/AlOH	5/1 Gossan	(5/4)(3/4) Unaltered Background	Inzana et al. (2003)
4	3/4 Outcrops	4/5 Gossan	5/7 FeOx/AlOH	Patel and Rumpel (1992)
5	PC Band 7	PC Band 4	PC Band 2	False color principle component stretch. principle component (PC) stretch disallows matching mineral groups to colors.
6	5/7 (PC Bands)	5/1 (PC Bands)	4 (PC Bands)	Colors should distinguish FeOx+AlOH, from mafic+FeIII rock use of PC stretch disallows matching mineral groups to colors but highlights differences between selected bands. Modeled after Abram (1980).
7	5/7 (PC Bands)	4/5 (PC Bands)	3/1 (PC Bands)	Initial combination Red-FeOx+AlOH Blue-Gossan+Fe rich Green-FeOx. PC stretch disallows matching mineral groups to colors but highlights differences between selected bands. Modeled after Patel and Rumpel (1992) and Harris et al., (1998).
8	5	4	1	Images used during 1993 assessment of DNWR. Primarily as a lithological discrimination image and to identify alteration as zones of higher albedo, not areas around Gass Peak in the in the north. Additionally other areas of red and magenta colors may indicate FeOx and clay minerals commonly associated with alteration south and Lake mine. Tingley et al. (1993)
9	5/7	3/1	1	
10	5/7	3/1	5/4	

3.2.2 ASTER

Processed Level 2B ASTER images were acquired through the Japanese Global Distribution System (GDS), at a cost of ~\$300 USD per scene. This processing provides the best crosstalk correction, (a type of interference between measured bands, which uncorrected, results in anomalously high values in the effected bands); additionally, it uses atmospheric corrections based on recorded day of year conditions to calibrate the image. The four atmospherically corrected and reflectance/emissivity calibrated ASTER scenes purchased are:

- (1) AST1_0010171853010106260661 collected October 17, 2000
- (2) AST1_0010171852430106260659 collected October 17, 2000
- (3) AST1_0005101854350204120789 collected May 5, 2000.
- (4) AST1_0507271838130508020119 collected July 27, 2005

After downloading, the ASTER scenes were loaded into ENVI methods similar to those used on the Landsat ETM+ data used beginning with an attempt to mosaic the images; however, due to slight differences within and between scenes (Figure 15), each image needed to be processed individually, this was done to avoid compounding problems relating to these “image artifacts”. True and false color images and band ratio images were generated based on established and tested methods described above and in Table 8. To reduce processing time and eliminate extraneous data, 15 m “true color” ASTER imagery was used in combination with geologic maps and digital elevation models (DEM) to build a mask over alluvium. The resulting data set was comprised of primarily in situ outcrops, which reduce false positives anomalies that commonly occur when mapping mineral end members over unconsolidated, unsorted, alluvial debris. These false positive anomalies were first identified in the DNWR scenes used in this

study, when mapping covered large areas of alluvial cover. The false positive anomalies likely result from pixels containing a mixed spectral signal derived from a variety of source rocks.

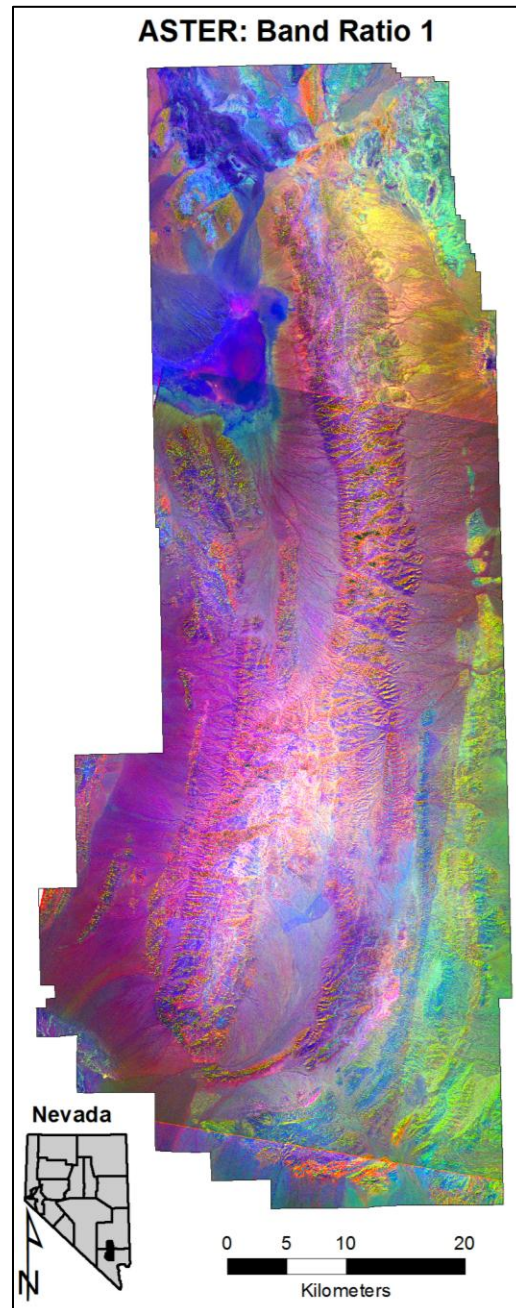


Figure 15: ASTER false color band ratio image highlighting data artifacts within an individual scene, note the bright green right half of the central scene vs. the red tones in the left half of the image, as well as the differences between the scenes in the north and south.

Table 8: List of ASTER band ratio and false color images. *Images not expressly discussed in the body of this text can be found in Appendix A.

ASTER Band Ratio Combinations				
Image #	Red	Green	Blue	Source
1	4/8 FeOx	4/2 Alteration	8/9 Contrast	Gabr et al., 2010
2	5/6 Sericite	7/6 Muscovite	7/5 Kaolinite	Hewson, 2001
3	4/2 Gossan	4/5 Alteration	5/6 Host	Volesky, 2003
4	5/6*7/6 Phengitic	6/8 Amphibole	4/5 Laterite	Bierwith, 2002
5	5/3+1/2 FeIII	(6+8)/7 Dolomite	(7+9)/8 Carbonate	Rowan et al., Combination (2003 & 2006)
6	Band 3	Band 2	Band 1	True/Natural Color Image
7	(11*11)/(10*12) Silica	13/14 Carbonate	12/13 Carbonate	Ninoyima et al., 2005

Following the methods used by Ninoyima (2003) and Gabr (2010), mineral indexes were initially created for hydroxyl minerals using $\left(\frac{\text{band7}}{\text{band6}}\right)\left(\frac{\text{band4}}{\text{band6}}\right)$, kaolinite using $\left(\frac{\text{band4}}{\text{band5}}\right)\left(\frac{\text{band8}}{\text{band6}}\right)$, alunite using $\left(\frac{\text{band7}}{\text{band5}}\right)\left(\frac{\text{band7}}{\text{band8}}\right)$, and carbonate minerals using $\left(\frac{\text{band6}}{\text{band8}}\right)\left(\frac{\text{band9}}{\text{band8}}\right)$. Additional mineral indexes and processing following Agar (2010) were used for dolomite, silica and iron oxide (Table 9). Agar's (2010) methods to map argillic, advanced argillic, propylitic, and opaline hydrothermal alteration were also tested along with the kaolinite and alunite indexes presented by Ninoyima (2003A) and Gabr (2010), but these mineral indices and mapping methods were not selected for continued processing and evaluation because the resulting data either only identified a few pixels, (5-20 pixels total) over large areas or the pixels were already identified by the more generalized silica and clays classes.

Table 9: List of ASTER band index methods. From Agar (2010). VNIR and SWIR images were processed surface reflectance images, at-surface radiance images were used to map silica using TIR imagery.

Mineral Index Methods*				
8 (Multi-color image)	Red-FeOx		Green-Clay	Mineral Likelihood Index Map
	Magenta-Silica	Cyan-Limestone	Blue-Dolomite	
Dolomite: Mask of ratios 4/5>1; 5/6>1; 7/6<1; 7/5<1; 7/8<1; 9/8>1, 6/9>1 on SFF result for Dolomite 1				
Calcite: Mask of ratios 4/5>1, 5/6>1, 7/6<1, 7/5<1,7/8>1,9/8>1, 5/8>1, 6/9>1 on SFF result for SFF result for Calcite 3				
FeOx: Mask of ratios 2/1, 3/2, & 3/1 within known ranges for goethite, hematite & jarosite on PC3 of PC123				
AIOH: Mask of ratios 4/5>1; 7/6>1, 7/8>1; on ratio 7/6				
Silica: Mask of band ratios 12/13<1; 12/11<1; 13/11>1; 11/10>1 on TIR MF result for silica				
*Note: Mineral Index Methods mask values are approximated here due to variables such as time of day, time of year, light cloud cover, pixel mixing etc. When masking band ratios the operator must set parameters to highlight contiguous pixels, ideally over regions known to contain the desired end member. This applies to all < > = operations shown above. (Specific masking thresholds used during this study can be found in the appendix.)				

Based on the zonation of ore deposits, discussed in the background section and preliminary evaluation of intermediate results described above, five mineral classes were selected for continued evaluation and field validation: iron oxide; dolomite (dolostone); silica; calcite (limestone); hydroxyl (clay) group minerals (Table 9). The weathering of iron sulfides (like pyrite to limonite) is a common indicator of potential ore zones. As the iron sulfide weathers, sulfuric acid can mobilize ore minerals while leaving limonite (jarosite, goethite, hematite, and gossan) behind. As discussed in the background, the identification of clay alteration zones is a very good indicator of hydrothermal activity, which commonly hosts zoned ore deposits such as high and low sulfidation deposits.

Hydrothermal silica including silicification, vuggy silica, jasperoid, and sinter, can be used as a geothermometer, indicating hot and/or acidic fluid capable of carrying ore minerals such as gold. Dolomite and calcite were selected for mapping to distinguish between dolomitization, which may be associated with a MVT and carbonate replacement deposits, and background or host lithology. This will also help identify discordant alteration minerals as they cut across various lithologies.

Band thresholds for end member “likelihood maps” were chosen by testing thresholds similar to those established by Agar (2010) (Table 9). The threshold values were selected to highlight contiguous pixels (representing outcrops), minimize scattered results (anomalous values), and result in regions of interest that best fit the spectral profile of end member classes. Using these methods, specific pixels corresponding to georeferenced ground locations were selected for field validation based on end member diversity, accessibility, and correspondence with geologic and geochemical features on available maps.

Samples were collected at each field site for laboratory spectral analysis. The most pure spectral end members were selected and used as the spectral end member input for final mapping using the ENVI Spectral Angle Mapper (SAM) mapping algorithm, which extrapolates spectral input data to classify pixels into end members or classify the pixel as unmapped if it does not meet the operator specified qualifications. Observations made during field validation were considered when determining final spectral mapping parameters and provided direction for operator guidelines when determining the mapped extent of final end member data products. The threshold values presented in Appendix B are the result of testing several SAM maximum angle values in an attempt to map each

individually processed scene to correspond with both field observations and end members mapped in continuous units across image boundaries. Where this was not possible values were selected similar to adjacent scenes. Intermediate evaluation found that iron oxides and silica minerals were underrepresented based on field observations and index mapping. To remedy this, silica and FeOx minerals were mapped separately from the other mineral classes using the tested threshold values shown in Appendix B. Band ratio threshold values were determined using similar methods to those described for “mineral likelihood” mapping described above, but looser constraints were used in an effort to capture more of the potential end members and field observations were used to guide the distribution of end member classes. All mineral maps were then exported as georeferenced TIFF images from ENVI and compiled into ArcGIS and evaluated alongside geologic data. Finally, polygons were drawn over areas dominated by somewhat continuous spectral end members. The final mapping products were compared to existing geologic maps and evaluated with respect to zoning patterns that are typically present in economic mineral deposits formed by the ore systems described above.

3.2.3 Spectra

Samples collected in the field were brought back to the laboratory for further spectral analysis. Additional analysis was performed using an ASD TerraSpec spectrometer for all samples; select samples were also analyzed with the Thermo Nicolet spectrometer. Spectrometry provides a more precise analysis and higher confidence identification beyond identification in the field. Standard practices were followed by measuring the rock target compared to a standard reference material. This generated

spectral output data as reflectance products, allowing direct comparison with library spectra.

Areas for sample collection in the field were initially chosen to verify the results of the preliminary remote image processing (Figure 16). After spectral collection ASD data was exported to SpecWin for viewing and interpretation. Comparative analysis was performed using USGS (Clark, 1993) and ASTER Spectral Library 2.0 (Baldrige et al., 2009). The most spectrally pure samples were identified based on dominant absorption features and comparison with library reference spectra. These “pure samples” were selected and used to generate a DNWR Spectral Library to be used with further processing using ENVI’s Spectral Angle Mapper (SAM) algorithm. This library was resampled to ASTER band positions and used as reference spectra to guide the SAM mapping algorithm for the five mineral end members.

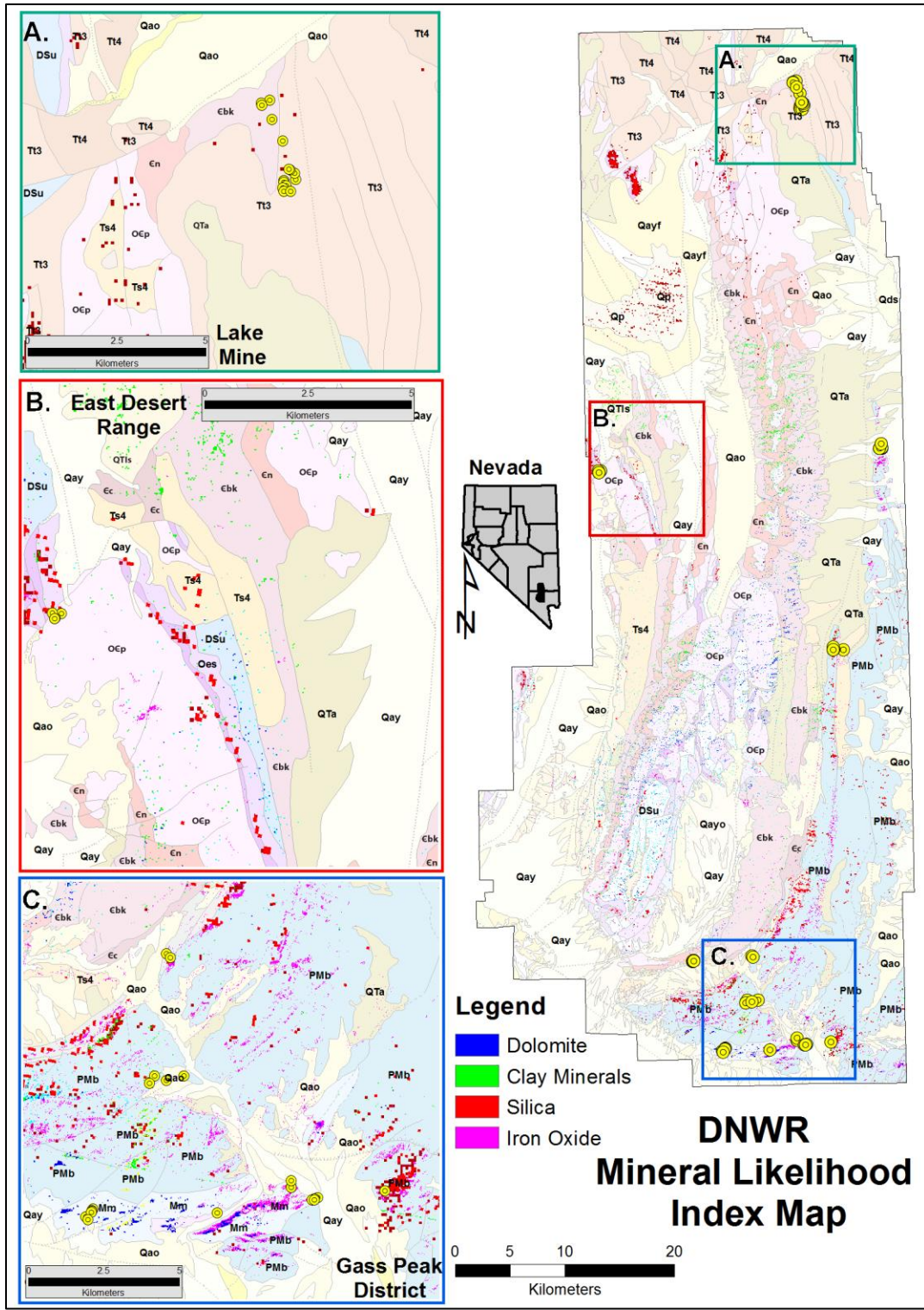


Figure 16: Mineral Likelihood Index Map: Southern DNWR. Limestone is extensive in the refuge and therefore not shown in this image. To better highlight the unique end members and their distribution pixels from index mapping are shown over a geologic map.

3.3 Field Validation/Verification

Samples collected in the field are carefully described both at the outcrop and hand-sample scale. Limestone/calcite and dolostone/dolomite are distinguished in the field by using dilute 10 M hydrochloric acid (HCl) to effervesce samples. Samples that readily effervesce are mainly limestone/calcite and those that only effervesce slightly contain mainly dolostone/dolomite. Samples with no reaction with HCl and are harder than steel are generally silica rich (i.e., quartzite sandstone, chert or a silicified rock (jasperoid). Red to yellow iron oxide staining was noted when present. Rocks, which appear bleached or decalcified, typically scratch easily with a steel probe and do not effervesce with HCl are typically comprised of dominantly hydroxyl-bearing clay minerals (illite, kaolinite, dickite, montmorillonite (smectite)).

4.0 Results

4.1 Landsat ETM+ Band Ratios

The Landsat ETM+ band ratio images below (Figure 17-20) are false color composite, band ratio images (other band ratio images can be found in Appendix A). This composite image combines R-G-B bands 5/7-5/1-5/4*3/4 respectively. Figure 17 includes the entire area of interest with the geologic map on the left. Red colors, intended to highlight clay and iron oxide rocks (alteration), correlate primarily with Nopah Formation and Pogonip Group rocks at higher elevations in the Sheep Range. Green areas in the image represent gossan rocks, which are relatively scattered and localized and generally correspond with alluvial deposits in the DNWR. The use of this band ratio mapping gossan rocks is intended as an additional way of mapping iron oxide minerals,

improving the chances of highlighting and identifying potential areas of alteration. The blue areas in the band ratio image represent unaltered background rocks and can be found relatively extensively in the DNWR though more continuously in the eastern portion of the DNWR. Magenta colors are a combination of red, clay and iron oxide alteration, and blue, unaltered rocks, suggesting weak to moderate alteration over these areas. Cyan colors are a combination of green, gossan rocks and blue, unaltered rocks, also suggesting only weak to moderate potential of gossan rocks. Yellow colors in the band ratio image represent a combination of red and green band ratios; therefore, yellow and bright colored areas should be regarded as locations most likely to contain altered rocks. However, at higher elevations in the Sheep Range densely vegetated juniper-pinyon pine forests are likely effecting spectral values and resulting in the anomalously mapped bright orange-yellow areas in Figure 17. Additional composite images highlight this same area in bright pixels.

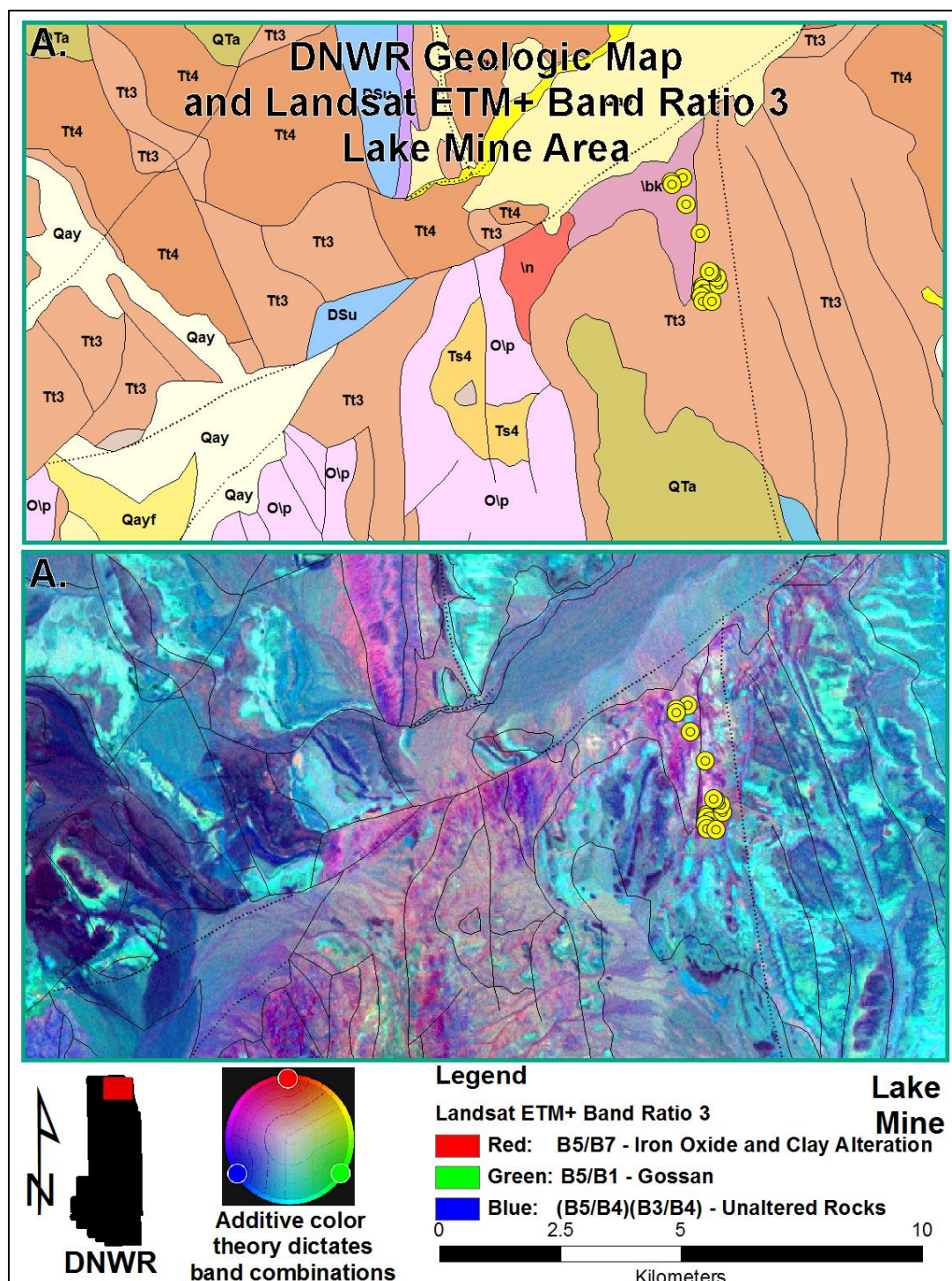


Figure 18: The Landsat ETM+ band ratio image shown here is a false color, band ratio, composite image with R-G-B bands $5/7-5/1-5/4*3/4$, covering the Lake Mine area in the DNWR as shown by box A in Figure 17. The $5/7$ band ratio, assigned to the red channel, highlights iron oxide and clay minerals. Band ratio $5/1$, assigned to the green channel, and is meant to highlight gossanous regions. Band ratio $5/4*3/4$ was assigned to the blue channel to highlight differences in lithologies. Sample locations shown with yellow dots. Geologic map and features from Page et al. (2005).

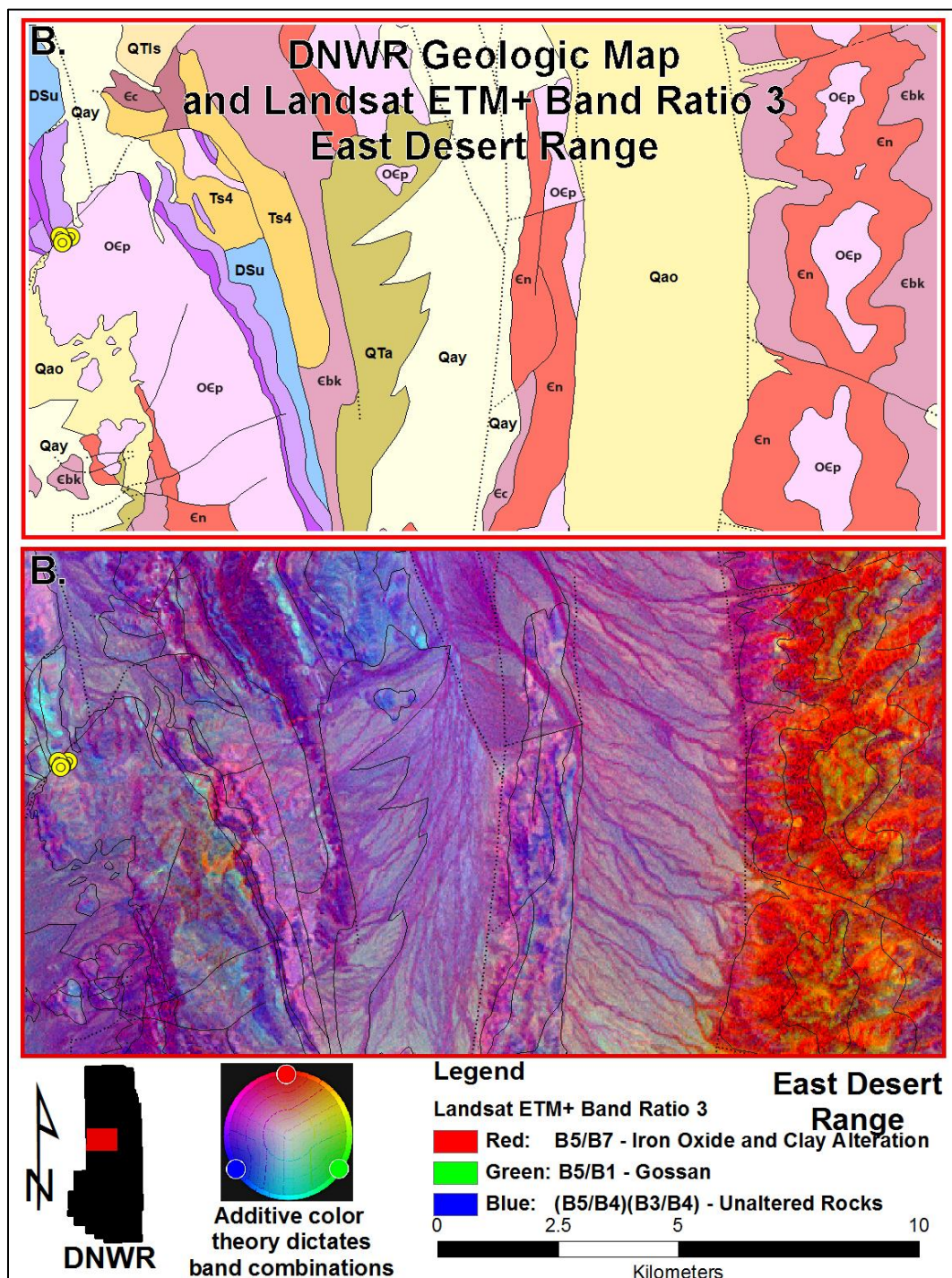


Figure 19: The Landsat ETM+ band ratio image shown here is a false color, band ratio, composite image with R-G-B bands $5/7-5/1-5/4*3/4$, covering the Lake Mine area in the DNWR as shown by box B in Figure 17. The $5/7$ band ratio, assigned to the red channel, highlights iron oxide and clay minerals. Band ratio $5/1$, assigned to the green channel, is meant to highlight gossanous regions. Band ratio $5/4*3/4$ was assigned to the blue channel to highlight differences in lithologies. Sample locations shown with yellow dots. Geologic map and features from Page et al. (2005).

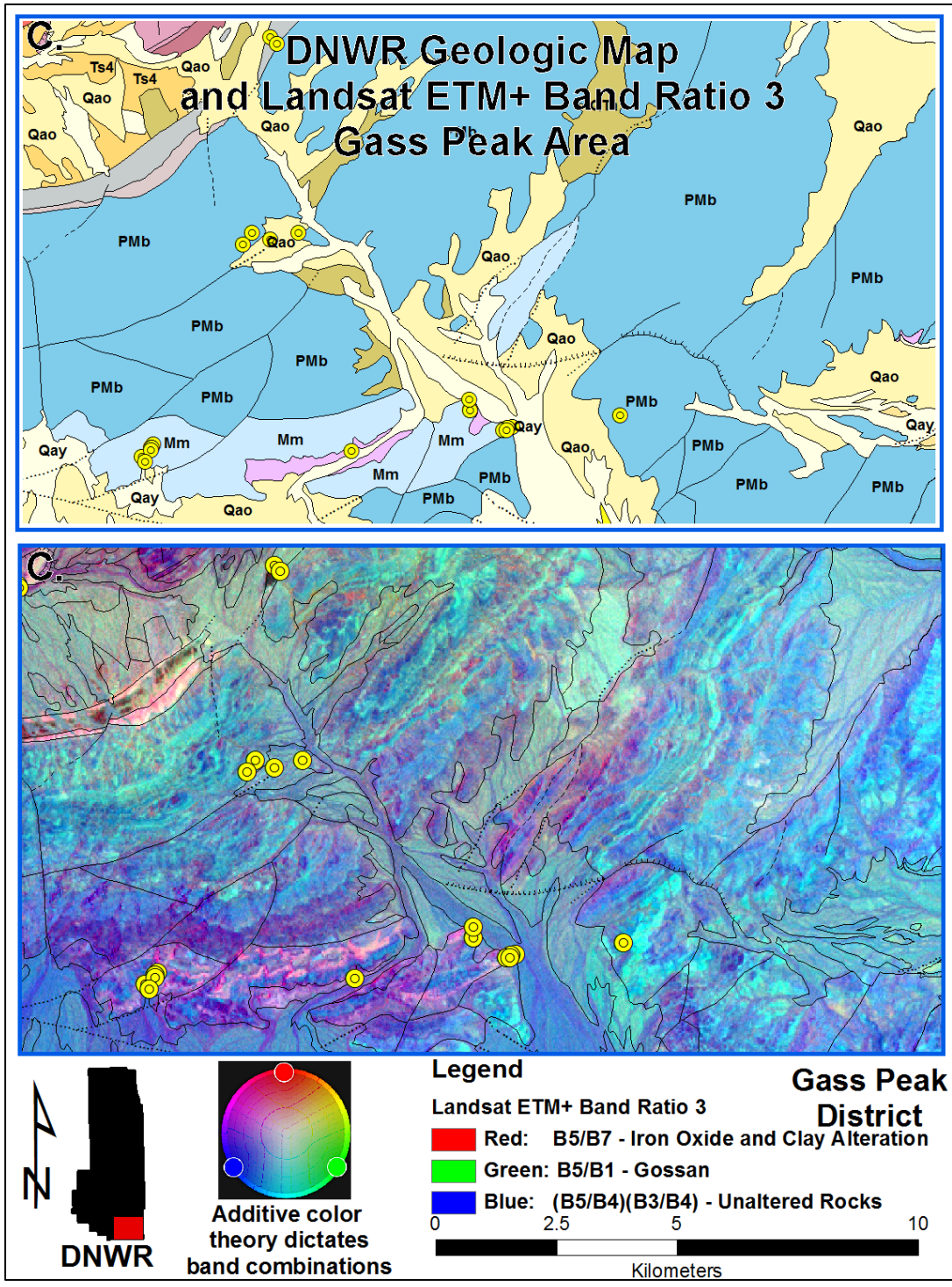


Figure 20: The Landsat ETM+ band ratio image shown here is a false color, band ratio, composite image with R-G-B bands $5/7-5/1-5/4*3/4$, covering the Lake Mine area in the DNWR as shown by box C in Figure 17. The $5/7$ band ratio, assigned to the red channel, highlights iron oxide and clay minerals. Band ratio $5/1$, assigned to the green channel, and is meant to highlight gossanous regions. Band ratio $5/4*3/4$ was assigned to the blue channel to highlight differences in lithologies. Sample locations shown with yellow dots. Geologic map and features from Page et al. (2005).

Figure 18, Figure 19, and Figure 20 show enlargements of Landsat ETM+ band ratio image 3 focusing on the Lake Mine area in the north, the East Desert Range in the west and the Gass Peak District in the south respectively. Field locations are shown with yellow points and the line work from the geologic map is overlain to help correlate features between the ratio image and the geologic map.

In Figure 18 the Lake Mine area found that the Bonanza King Formation rocks shown on the geologic map correlate well with the extent of the hydrothermal alteration observed in the field. The alteration correlates with the light red (pink) to magenta colors in the band ratio image. Purple to magenta colors also correlate with Devonian and Silurian Undifferentiated carbonate rocks and some Pogonip Group rocks. Blue and cyan colors correlate most with Tertiary volcanic rocks. Field observations of Tertiary volcanic rocks in the northeast corner of the map area found they are unaltered.

Figure 19 shows the correlation between Nopah Formation and Pogonip Group rocks at high elevations of the Sheep Range and the red colors from the band ratio image. Rocks of the Bonanza King and Nopah Formations, Pogonip Group rocks at lower elevations are typically marked by dark magenta colors in the band ratio image. Sedimentary and alluvial fan units are generally marked by light colored pink to magenta colors, and darker magenta and blues correspond to regions mapped as Eureka Quartzite and Ely Springs Dolomite rocks in the geologic map.

Figure 20 shows most of the Gass Peak District including the June Bug Mine area. Most of the blue and cyan colors correspond to the Bird Spring Formation rocks. Mississippian-Devonian Undifferentiated rocks and Mississippian Monte Cristo

Formation rocks are marked by magenta and pink colors in the Landsat ETM+ band ratio image. In the northwest corner of the figure, where lower Cambrian and Late Precambrian rocks crop out, the band ratio image shows very light pink to white colors.

4.2 ASTER

4.2.1 Band Ratio Images

The ASTER band ratio image 1 is shown in Figures 21-24, which are false color, band ratio, composite images with R-G-B bands 4/8-4/2-8/9 respectively, (additional ASTER band ratios are shown in the Appendix A). The 4/8 band ratio, assigned to the red channel, highlights iron oxide (limonite) minerals. Band ratio 4/2, assigned to the green channel, and it is intended to highlight hydroxyl-bearing clay minerals (alteration). Band ratio 8/9 is assigned to the blue channel and designed to provide an unaltered background for the other two bands. Figure 21 shows the area of interest, as can be clearly seen by the distinctive patchwork pattern showing both differences between scenes, which mostly east-west, and image artifacts within scenes, running mostly north-south. Because of these differences the coloring is not distinctive or consistent throughout the images; however, the band ratios still highlight the desired mineral groups.

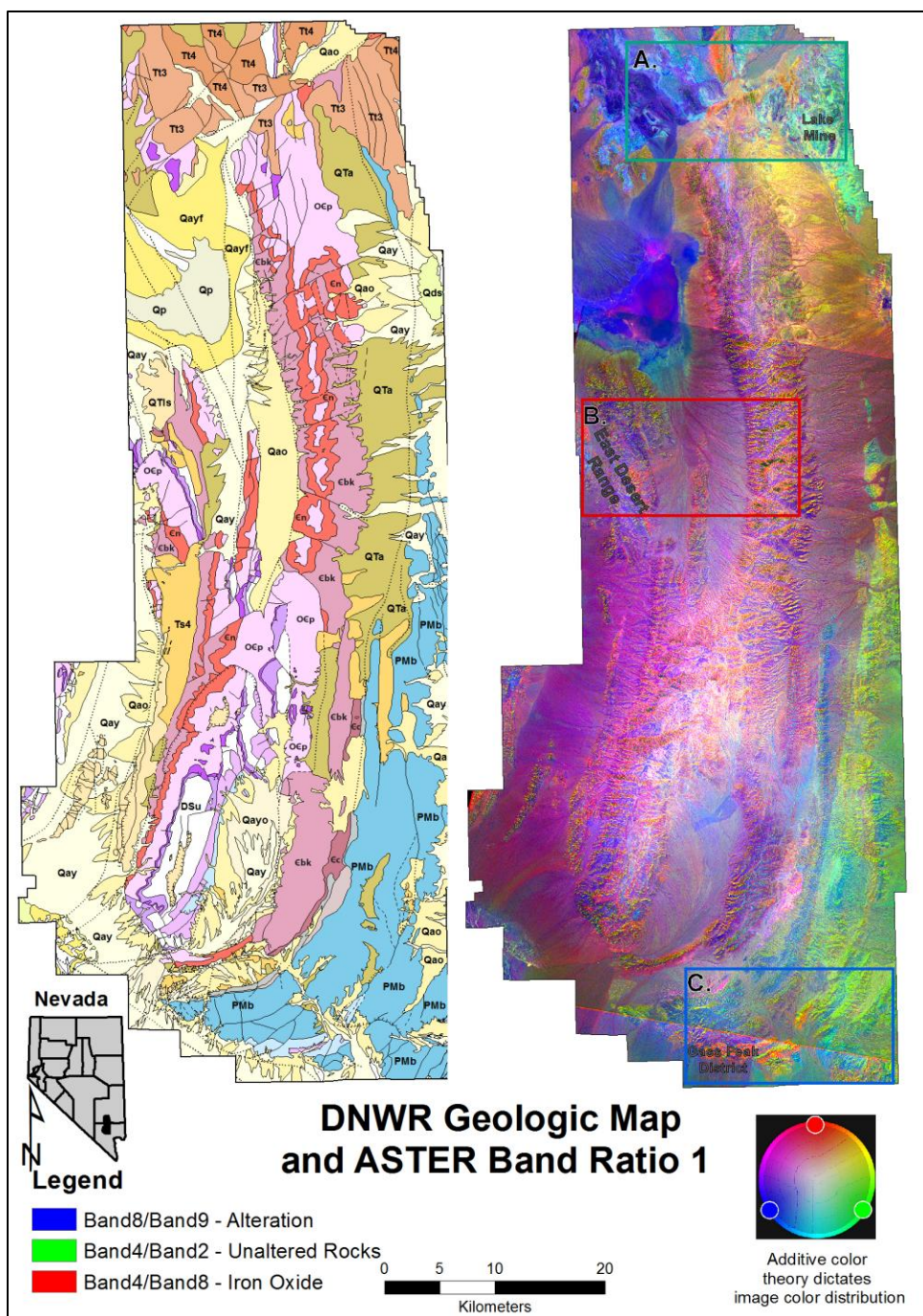


Figure 21: The ASTER band ratio image shown here is a false color, band ratio, composite image with R-G-B bands 4/8-4/2-8/9. The 4/8 band ratio, assigned to the red channel, highlights limonite (iron-oxides). Band ratio 4/2, assigned to the green channel, and is meant to highlight hydroxyl minerals (alteration). Band ratio 8/9 was assigned to the blue channel to provide unaltered background. Boxes A., B., C., represent the areas shown in Figure 22, Figure 23, and Figure 24 below. Geologic map and overlain features from map M150, Page et al. (2005).

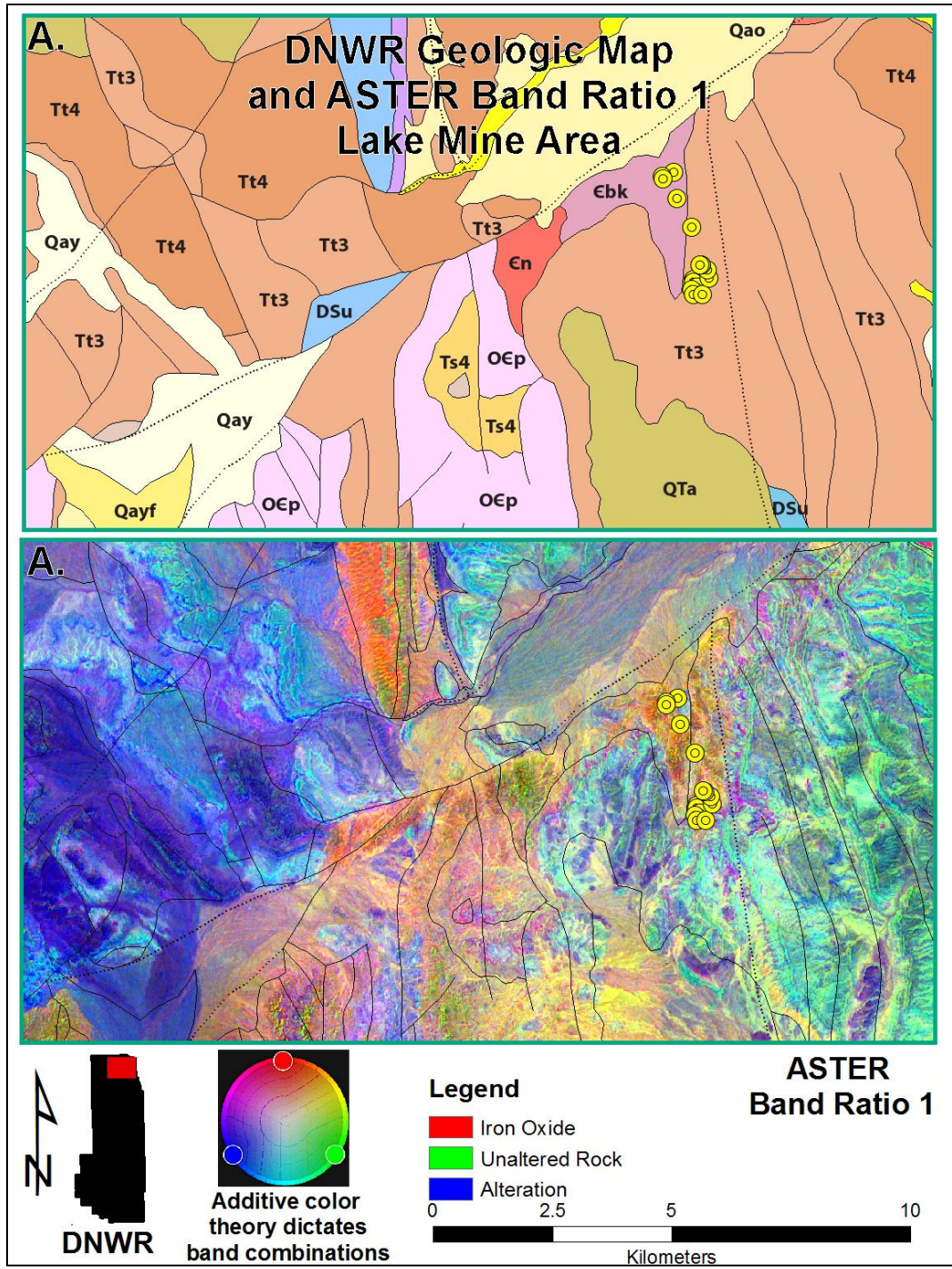


Figure 22: The ASTER band ratio image shown here is a false color, band ratio, composite image with R-G-B bands 4/8-4/2-8/9. The 4/8 band ratio, assigned to the red channel, highlights limonite (iron-oxides). Band ratio 4/2, assigned to the green channel, and is meant to highlight hydroxyl minerals (alteration). Band ratio 8/9 was assigned to the blue channel to provide unaltered background. This image focuses on the Lake Mine area. Yellow dots are GPS waypoints correlating to field stations and sample locations. Geologic map and overlain features from map M150, Page et al. (2005).

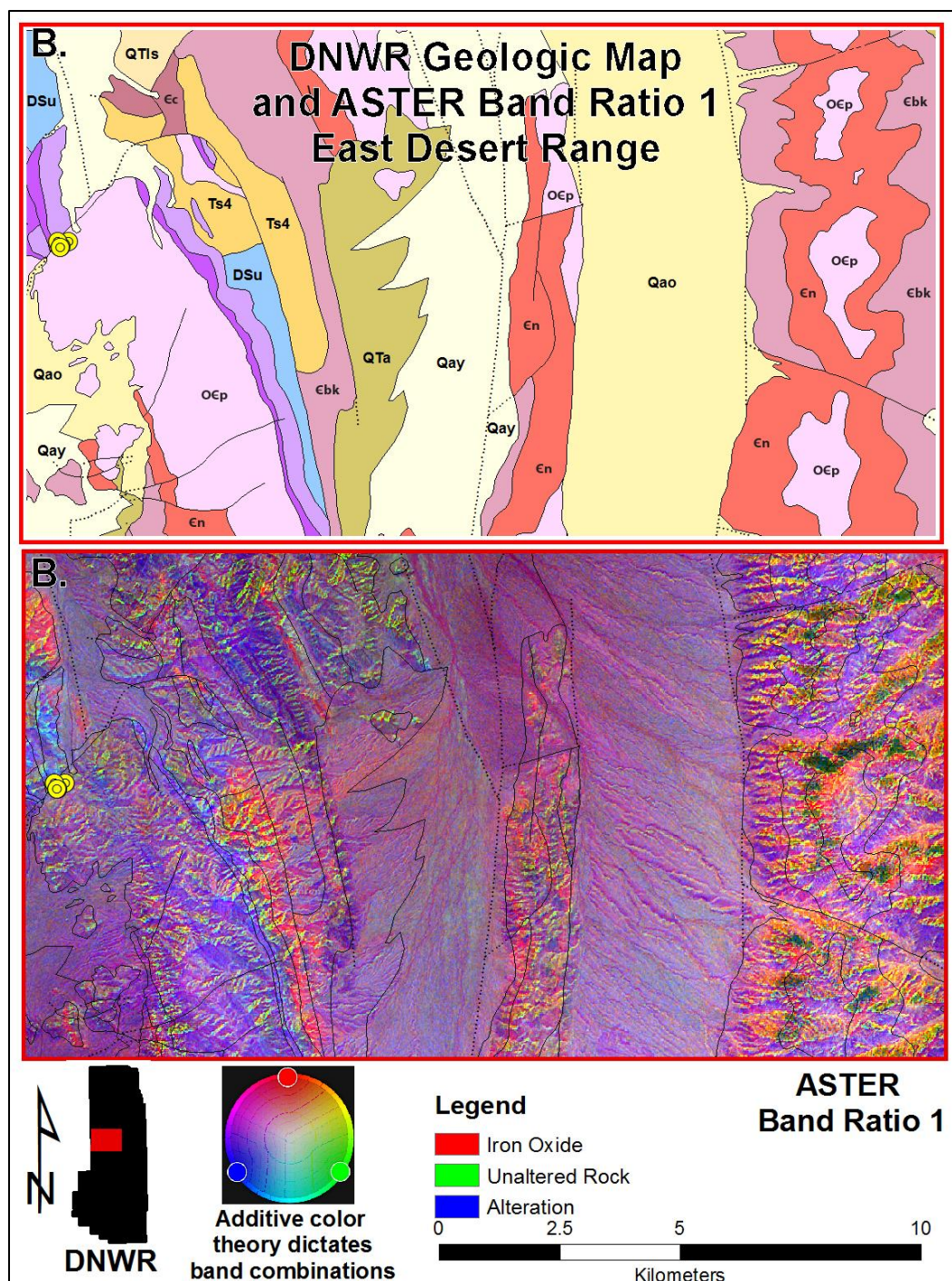


Figure 23: The ASTER band ratio image shown here is a false color, band ratio, composite image with R-G-B bands 4/8-4/2-8/9. The 4/8 band ratio, assigned to the red channel is intended to highlight limonite (iron-oxides). Band ratio 4/2, assigned to the green channel, and is meant to highlight hydroxyl minerals (mainly clays the could be related to hydrothermal alteration). Band ratio 8/9 was assigned to the blue channel to provide unaltered background. Yellow dots are GPS waypoints correlating to field stations and sample locations. This image focuses on the East Desert Range. Geologic map and overlain features from map M150, Page et al. (2005).

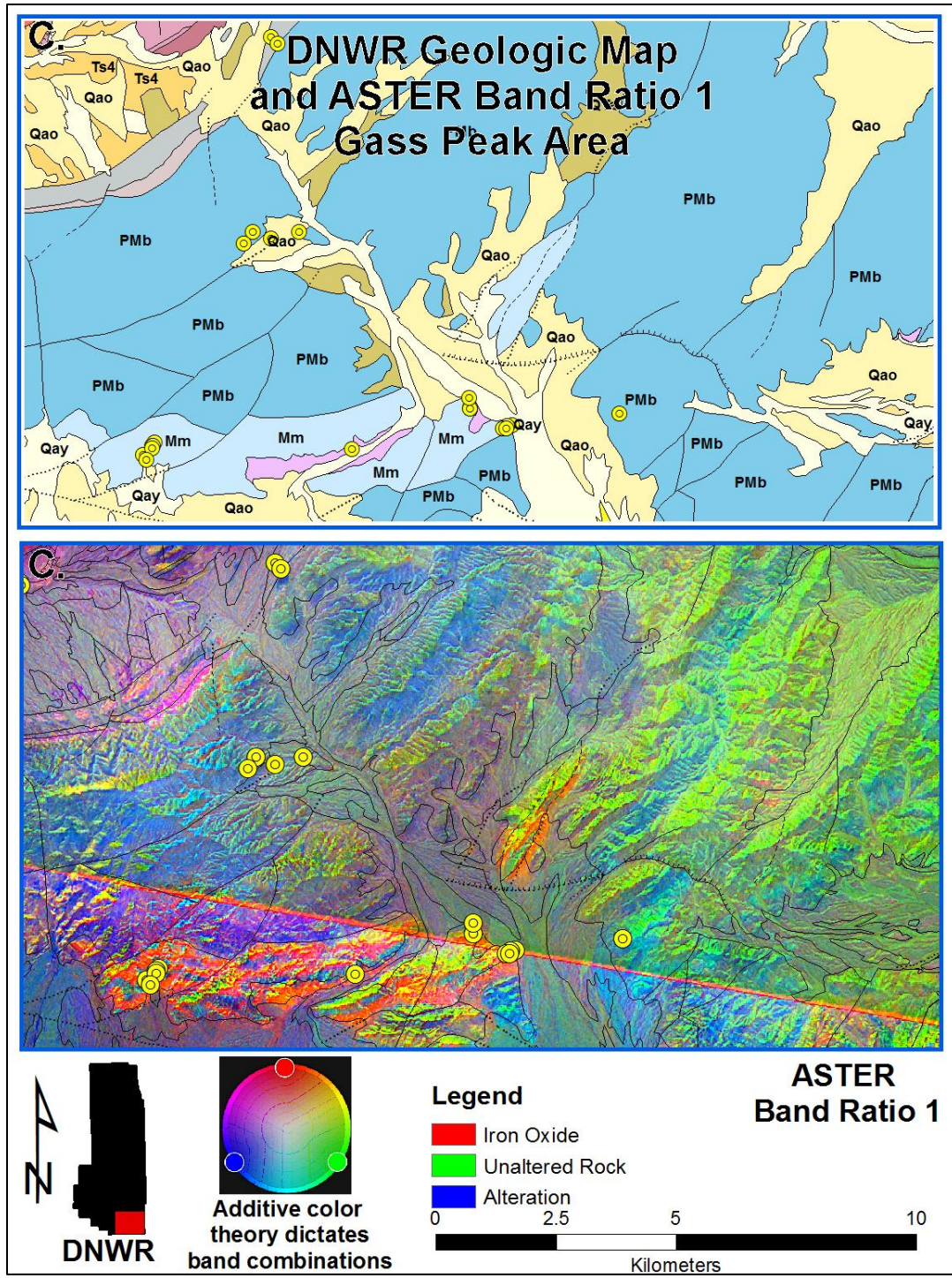


Figure 24: The ASTER band ratio image shown here is a false color, band ratio, composite image with R-G-B bands 4/8-4/2-8/9. The 4/8 band ratio, assigned to the red channel, highlights iron-oxides. Band ratio 4/2, assigned to the green channel, and is meant to highlight hydroxyl minerals (alteration). Band ratio 8/9 was assigned to the blue channel to provide unaltered background. Yellow dots are GPS waypoints correlating to field stations and sample locations. This image focuses on the Gass Peak District. Geologic map and overlain features from map M150, Page et al. (2005).

Figure 22 focuses on the Lake Mine area where Bonanza King and Nopah Formations, Pogonip Group, and Devonian-Silurian undivided rocks are differentiated similarly to the Landsat ETM+ band ratio image shown in Figure 18 above. The hydrothermal alteration near the field stations, shown with yellow dots, correlates with Bonanza King Formation rocks on the geologic map and is marked by varying shades of orange to pinkish tones in the ASTER band ratio image. Tertiary volcanic rocks east of the Lake Mine area are dominantly green colored marking them as largely unaltered. In the northwest portion of Figure 22, cyan, blue and purple tones variably correspond with Tertiary volcanic rocks.

Figure 23 covers the East Desert Range. It is dominated by red, blue, and magenta tones, which appear to correspond mostly with topographic differences, highlighting drainages in the Sheep Range. Only minor differences in tone are seen in varying lithological units.

Figure 24 covers the Gass Peak District, focuses on the same area as the Landsat EMT+ image in Figure 20, and provides similar discrimination of ground cover. The regions highlighted in yellow, red, and orange tones highlight the area near most of the mine workings in the Monte Cristo Formation and undifferentiated Mississippian-Devonian rocks near the thrust faulting described in section 17. Bird Spring Formation rocks are generally even toned with the most striking differences apparent along the east-west line that marks the edge of two ASTER scenes. Cambrian and Precambrian rocks in the northwest map as magenta, which may suggest iron oxide/alteration or simply be outlining lithologic boundaries.

4.2.3 Mineral Probability Mapping

The following figures show the final mapping products, reflecting the more rigorous mapping parameters described above and involving the integration of spectra from field gathered samples with the Spectral Angle Mapper algorithm. This algorithm, assigns unknown pixels to one of the user specified end members or as unclassified. By utilizing geologic mapping, field observations, and spectral libraries to guide the SAM algorithm mineral distribution map can be generated with a high level of confidence (Figure 25). However, after noting that the SAM result in Figure 25 failed to identify silica and iron oxide features observed in the field, such as those in Figure 16, Box C and A, shown in the Mineral Likelihood Map and Field Validation locations in the East Desert Range and Gass Peak District respectively, additional processing was used to map silica and iron oxides individually (these processing steps are described in detail in the Appendix B). Their distribution is shown in Figure 26. These data were combined with the SAM result from Figure 25 to generate Figure 27: Final Mineral Distribution Map, and its corresponding zoomed images (Figures 28-30), and polygon map (Figure 31). These data products show the geographic location of the selected mineral classes as mapped by the SAM algorithm and the additional mapping methods described above.

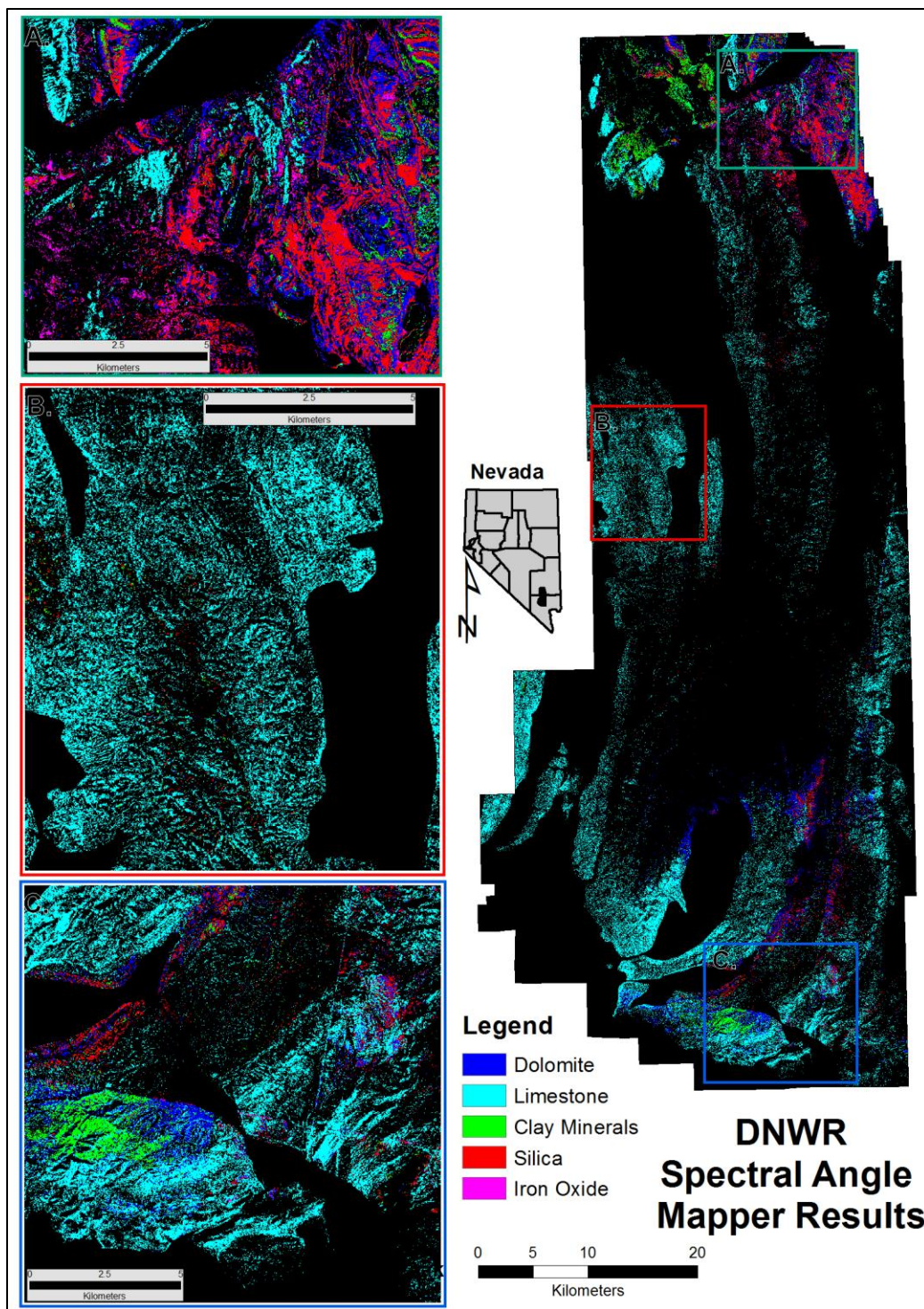


Figure 25: Spectral Angle Mapper result for dolomite; limestone; clay; silica and iron oxide mapping in the DNWR. Boxes A, B, C are zoomed images corresponding to the areas marked to the right.

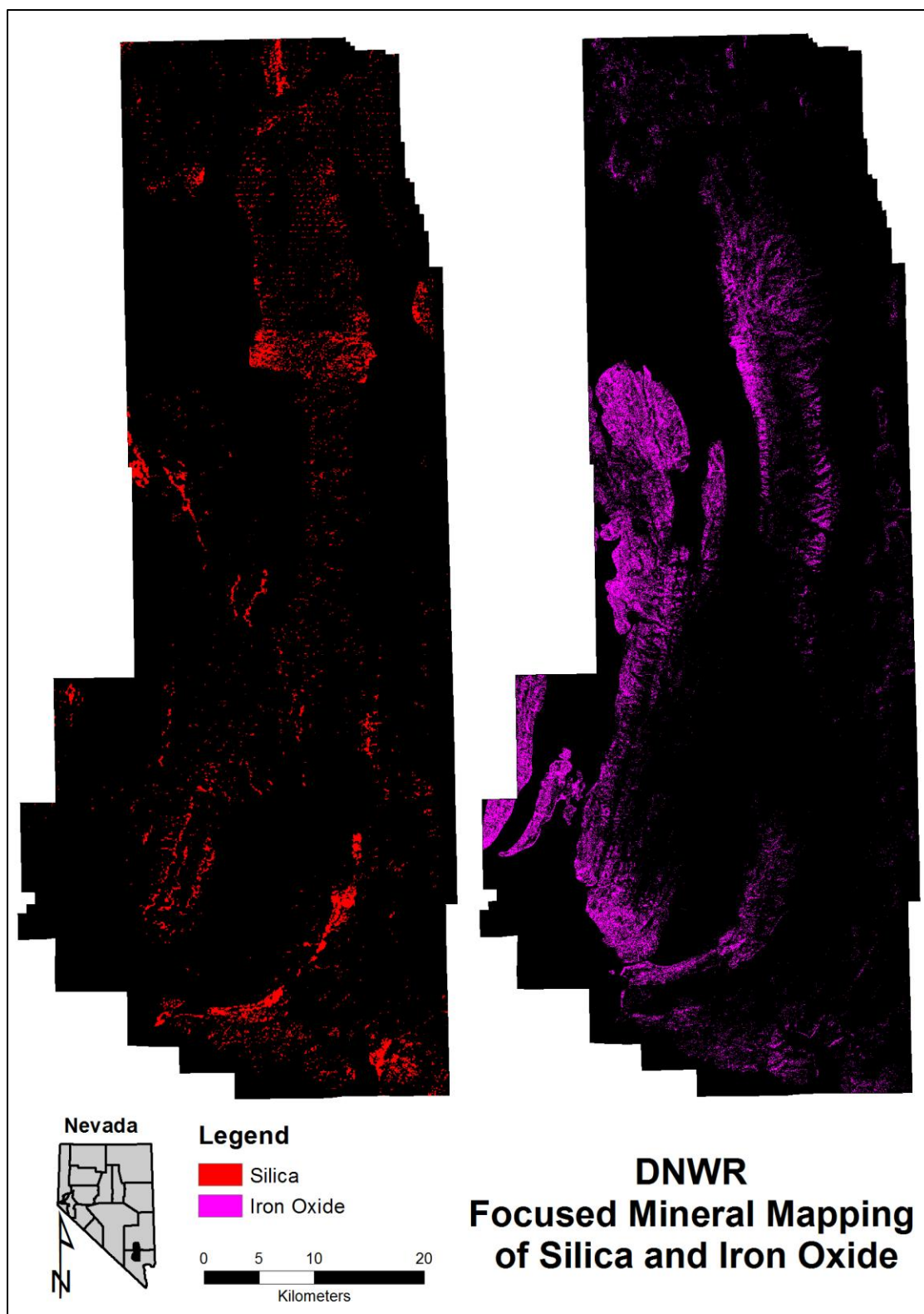


Figure 26: Individual mineral mapping for silica and iron oxides minerals.

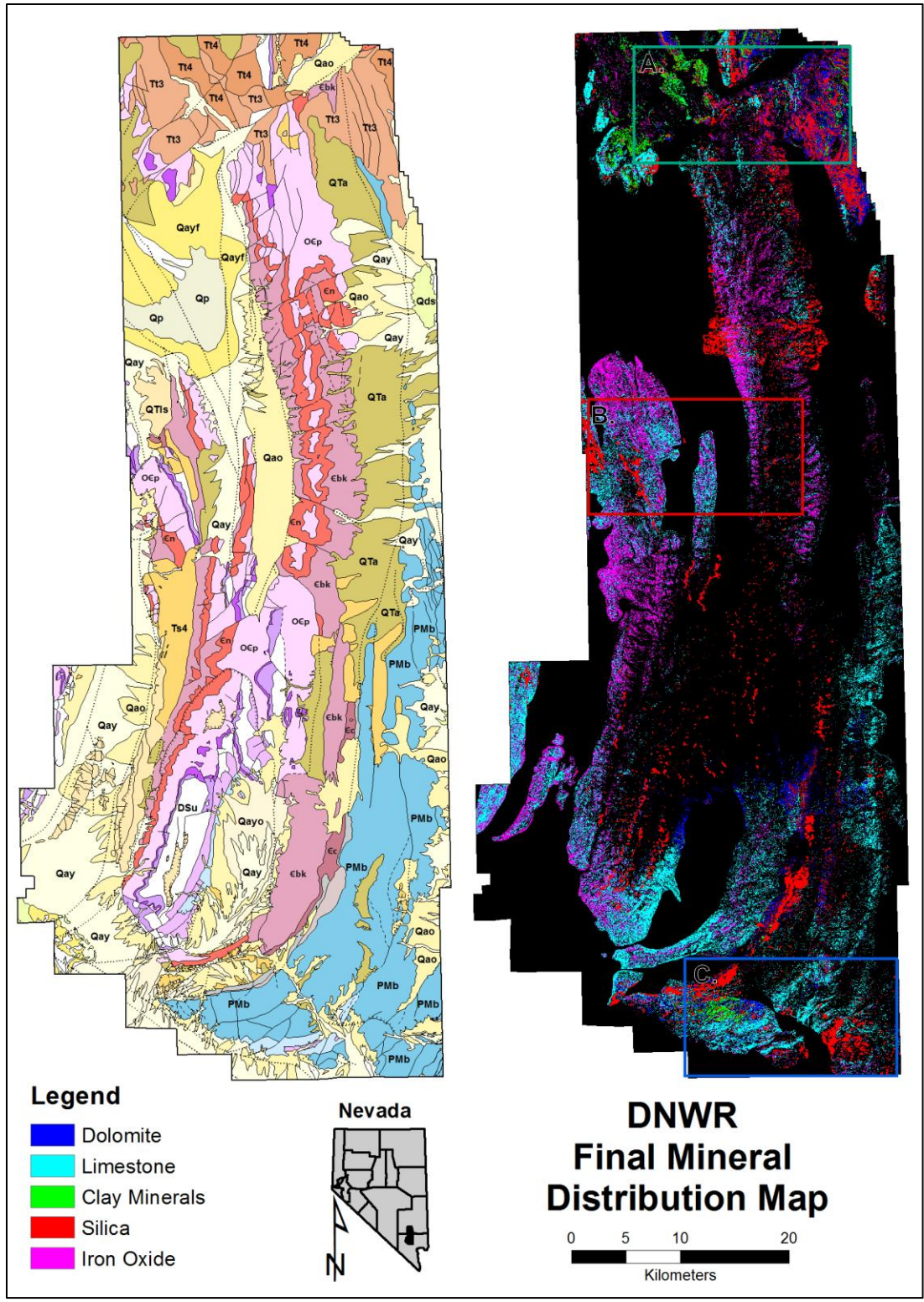


Figure 27: Spectral Angle Mapper result for dolomite, limestone, and clay; silica and iron oxide mapped separately as described above. Boxes A, B, C are zoomed regions corresponding to the areas described below. Geologic map from Page et al. (2005).

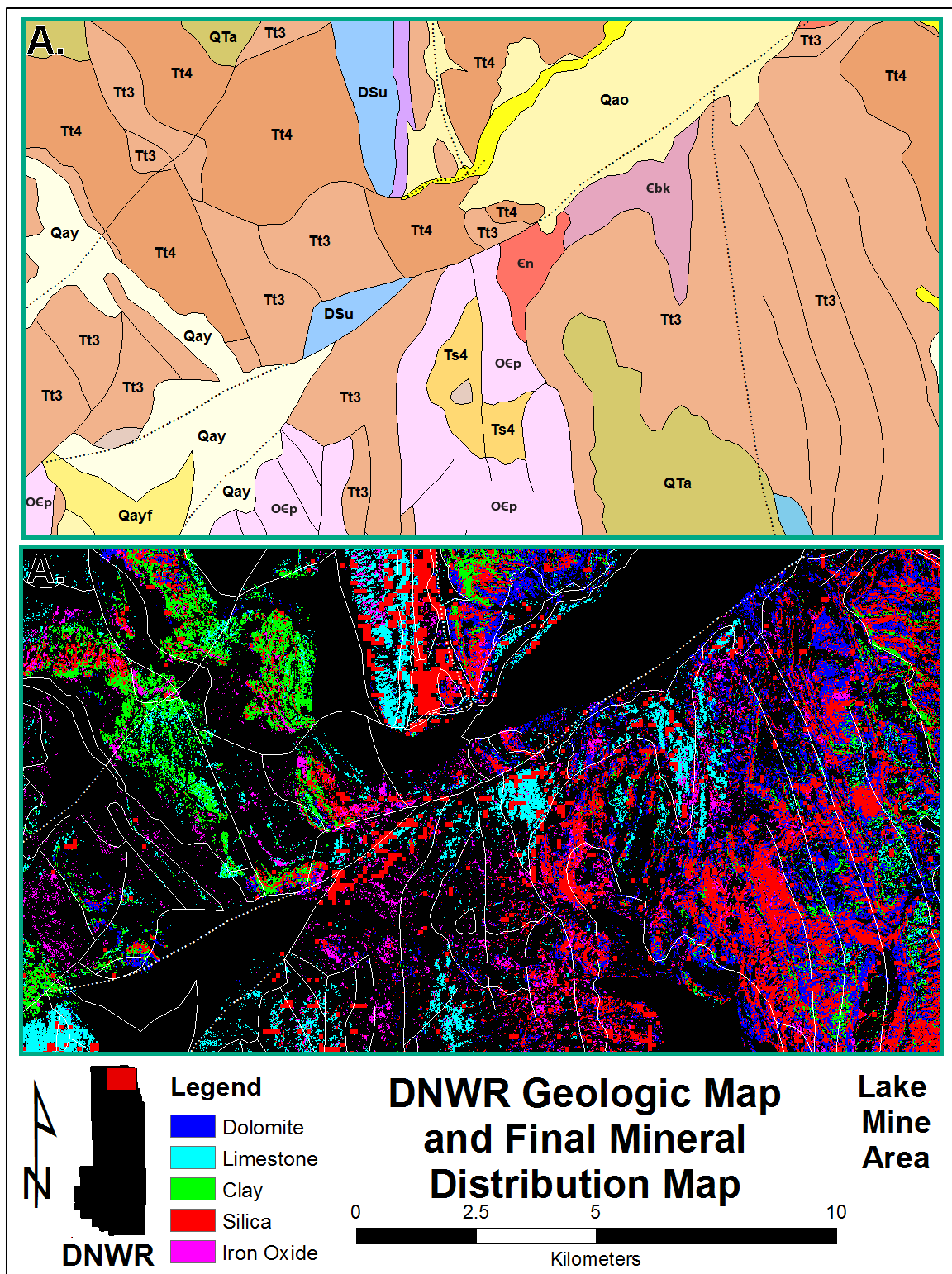


Figure 28: Spectral Angle Mapper result for dolomite, limestone, and clay; silica and iron oxide mapped separately as described above. Zoomed region corresponding to box A in Figure 27 Lake Mine area. Geologic map from Page et al. (2005).

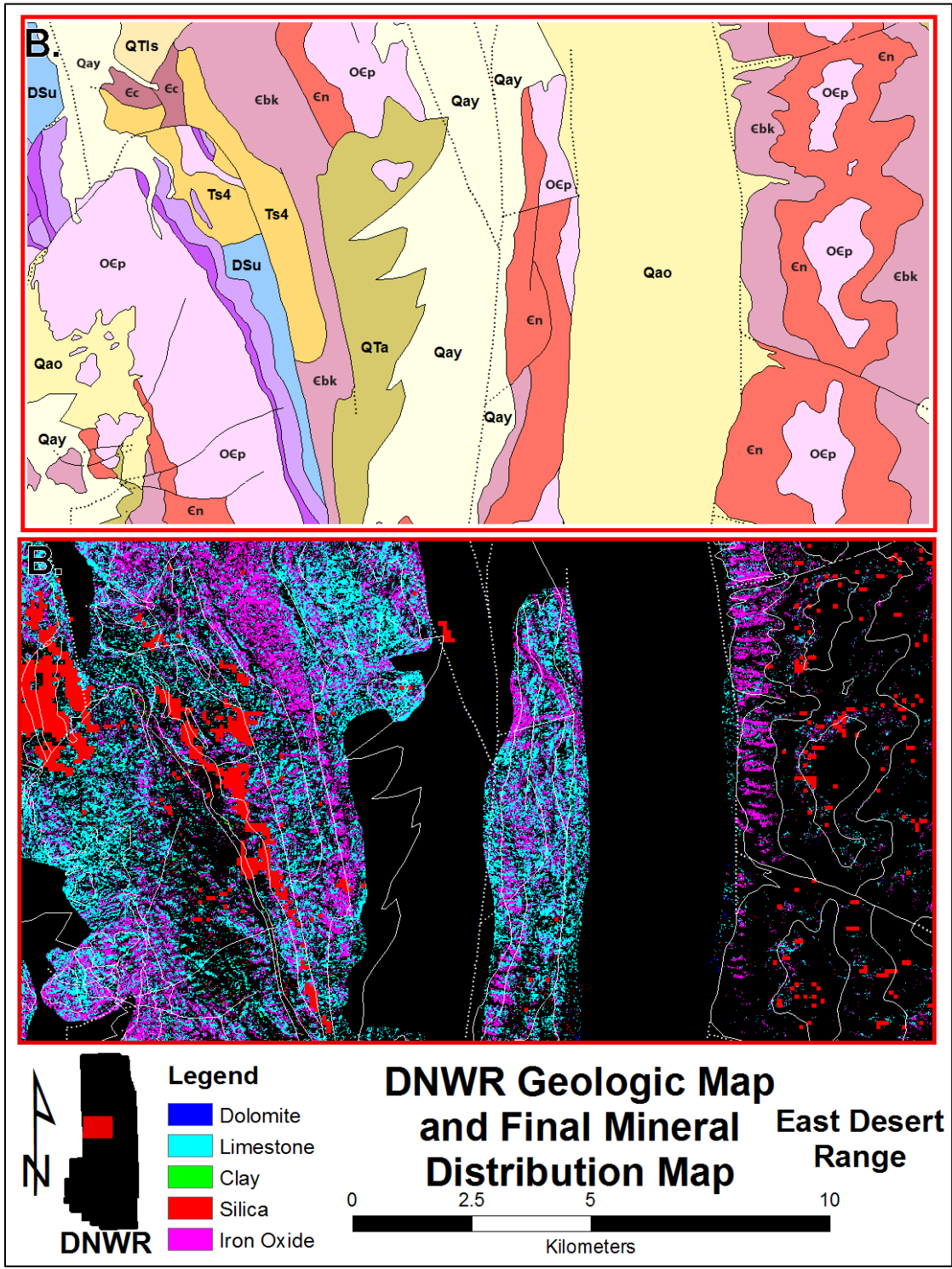


Figure 29: Spectral Angle Mapper result for dolomite, limestone, and clay; silica and iron oxide mapped separately as described above. Zoomed region corresponding to box B in Figure 27 East Desert Range. Geologic map from Page et al. (2005).

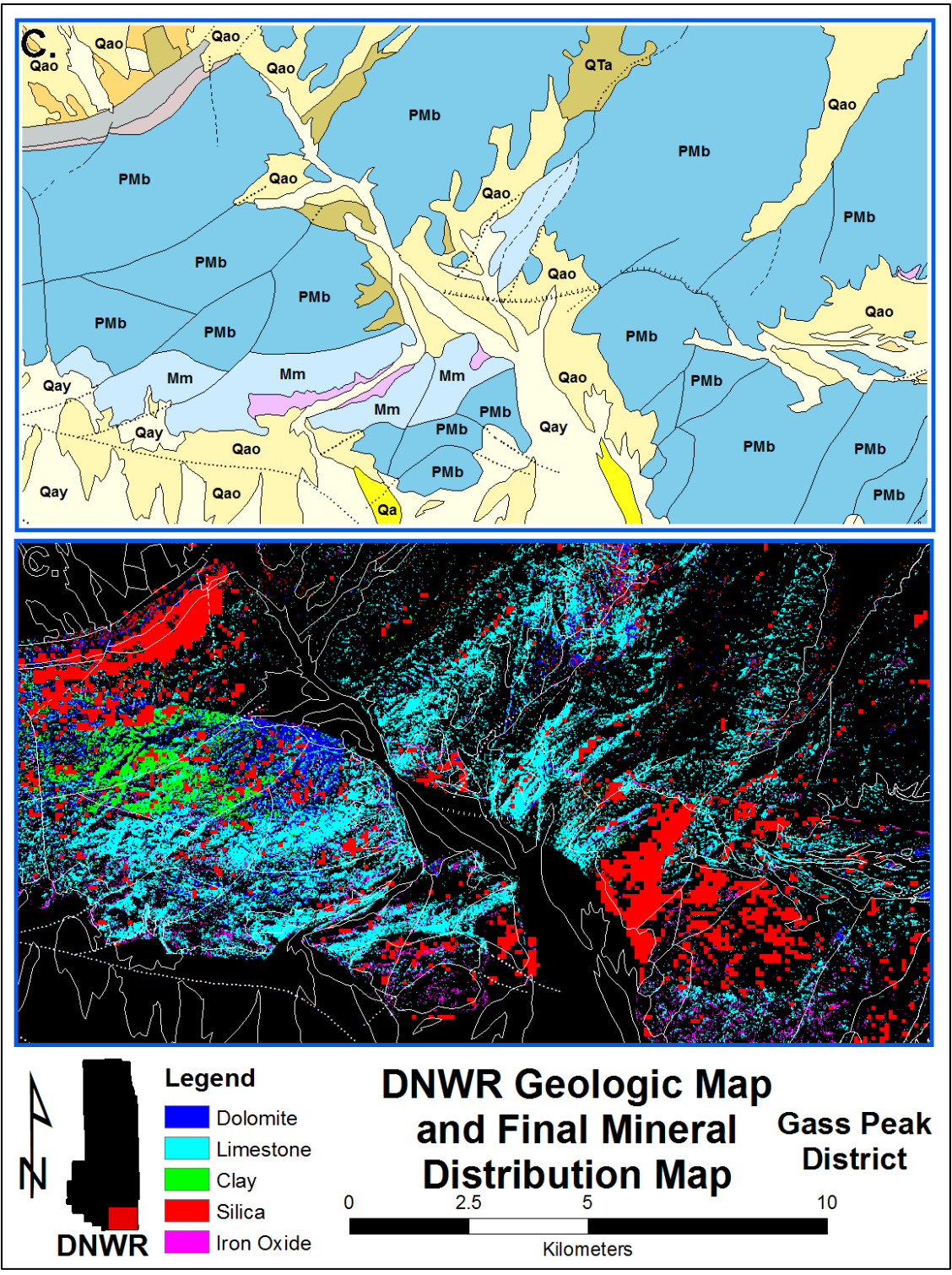


Figure 30: Spectral Angle Mapper result for dolomite, limestone, and clay; silica and iron oxide mapped separately as described above. Zoomed region corresponding to box C in Figure 27. Gass Peak District. Geologic map from Page et al. (2005).

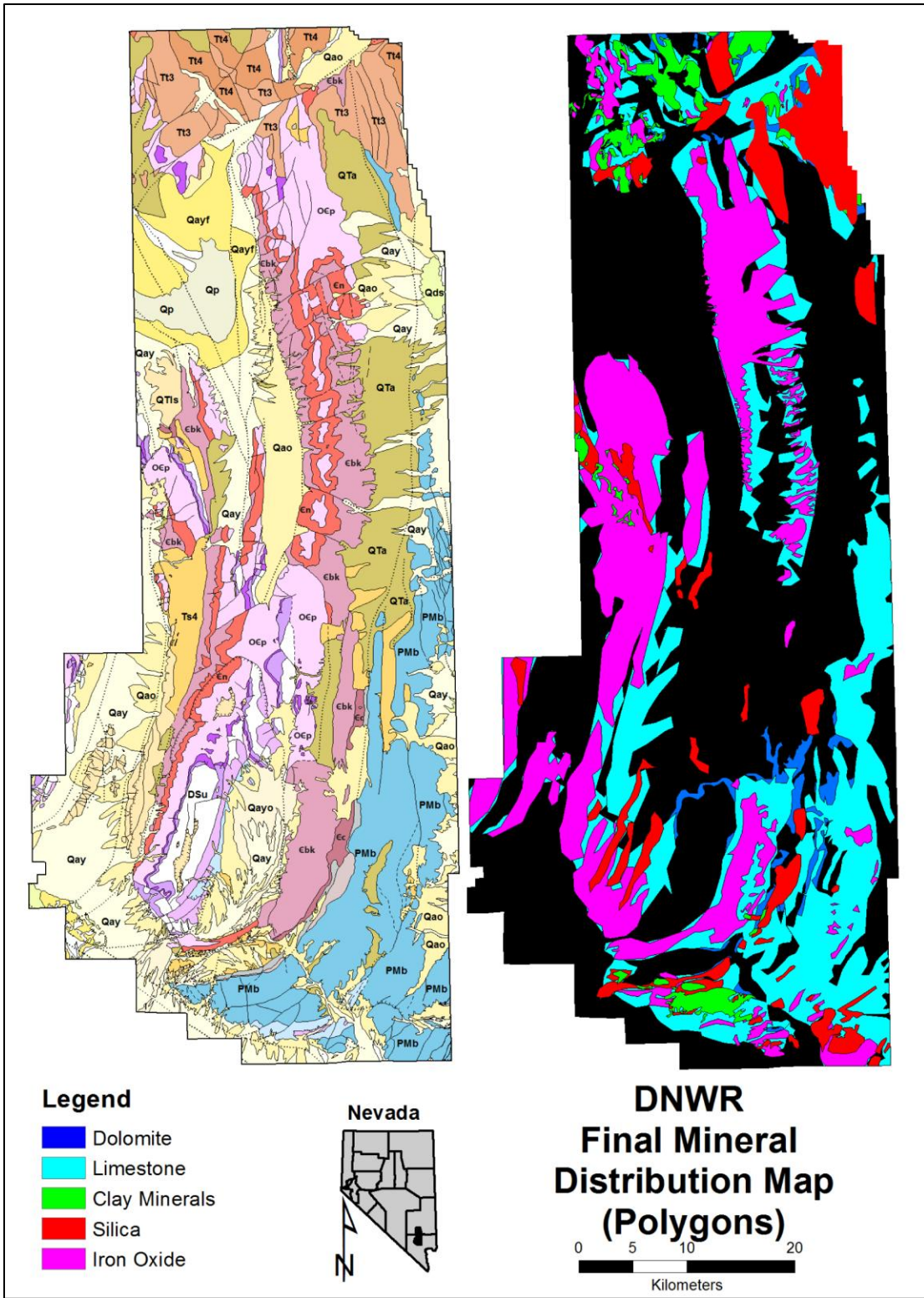


Figure 31: Polygon mapping showing the distribution of dense pixels identified from Figure 27, SAM result for dolomite, limestone, and clay; and silica and iron bearing minerals mapped using alternate processing methods as described above.

Figure 28 shows the zoomed in portion of the DNWR surrounding the Lake Mine area. Devonian-Silurian Undifferentiated units, Bonanza King Formation, Pogonip Group and Nopah Formation rocks are mostly generally mapped as limestone. Tertiary volcanic rocks in the east portion of the figure correlate mostly with the silica class, and to a lesser extent dolomite and clay. Younger Tertiary volcanic units to the northwest correlate most with the clay end member and to a lesser extent the silica end member. Iron oxide is locally present in most formations; however no distinct or significant distribution pattern is obvious in the distribution of this class.

Figure 29 shows the final mineral distribution map for the East Desert Range area. Iron oxide minerals are dominantly mapped over Bonanza King Formation rocks, locally limonite was observed coating partings between beds. Silica is mapped over areas shown as Eureka Quartzite and Eureka Quartzite/Pogonip Group rocks (undivided). Other units appear to be dominantly limestone. The large dark area on the east portion of the figure is dominantly unclassified, meaning that the spectra did not fit the end member parameters used in the mapping analysis.

In Figure 30 Bird Spring Formation rocks cover most of the image and are classified primarily as limestone. Portions of the northwest are mapped as dolomite and clay. Additionally, a significant portion of the southeast is mapped as silica where chert was observed during field work. Sterling Quartzite and parts of the adjacent Wood Canyon Formation in the northwest are also mapped as silica. Mississippian Monte Cristo formation rocks and undifferentiated Mississippian-Devonian rocks are mostly mapped as limestone with minor iron oxide and silica. Field observations over this area

found interbeds commonly with a thin silica rind, typically with some iron oxide staining, within portions of the Mississippian Monte Cristo limestone members as well as locally within the Permian Bird Spring Formation. Field checks of the more contiguous silica anomaly to the east were found to be consistent with a relatively massive (tens of meters thick) chert member in the Bird Spring Formation. Locally interbedded chert was also observed between sandstone and limestone units in the Bird Spring Formation.

4.3 Spectrometry

4.3.1 VNIR-SWIR (Lab and ASTER)

Figure 32 includes high resolution reference spectra from the USGS Spectral Library (Clark et al., 1993) for each of the mineral groups evaluated, as well as arrows marking out diagnostic absorption features in the spectra. Goethite serves as a representative for iron oxides; kaolinite and smectite are representative of hydroxyl-bearing clay minerals; calcite is used to identify limestone; dolomite is used to identify dolostone; and because silica has no spectral signature in the VNIR-SWIR portion of the EM spectrum it is evaluated using the Thermo Nicolet TIR spectrometer discussed in the next section. ASD TerraSpec spectra collected from samples gathered in the field are shown below the USGS spectra and have been re-sampled to ASTER spectral wavelengths, shown below the ASD spectra. Additionally, the spectral signature from the remotely mapped end-members in the Gass Peak District is also shown and ASTER band passes are shown at the bottom of the figure. With 2,151 bands, the ASD TerraSpec provides data with a sampling density over two-hundred times greater than the ASTER sensors 9 bands over the same wavelengths. This results in crude resolution making the

identification of specific minerals difficult. In the ASTER resampled data (Figure 32), dolostone and limestone end members look largely similar; however, subtle differences in the angle between ASTER bands 5 and 8 can be observed.

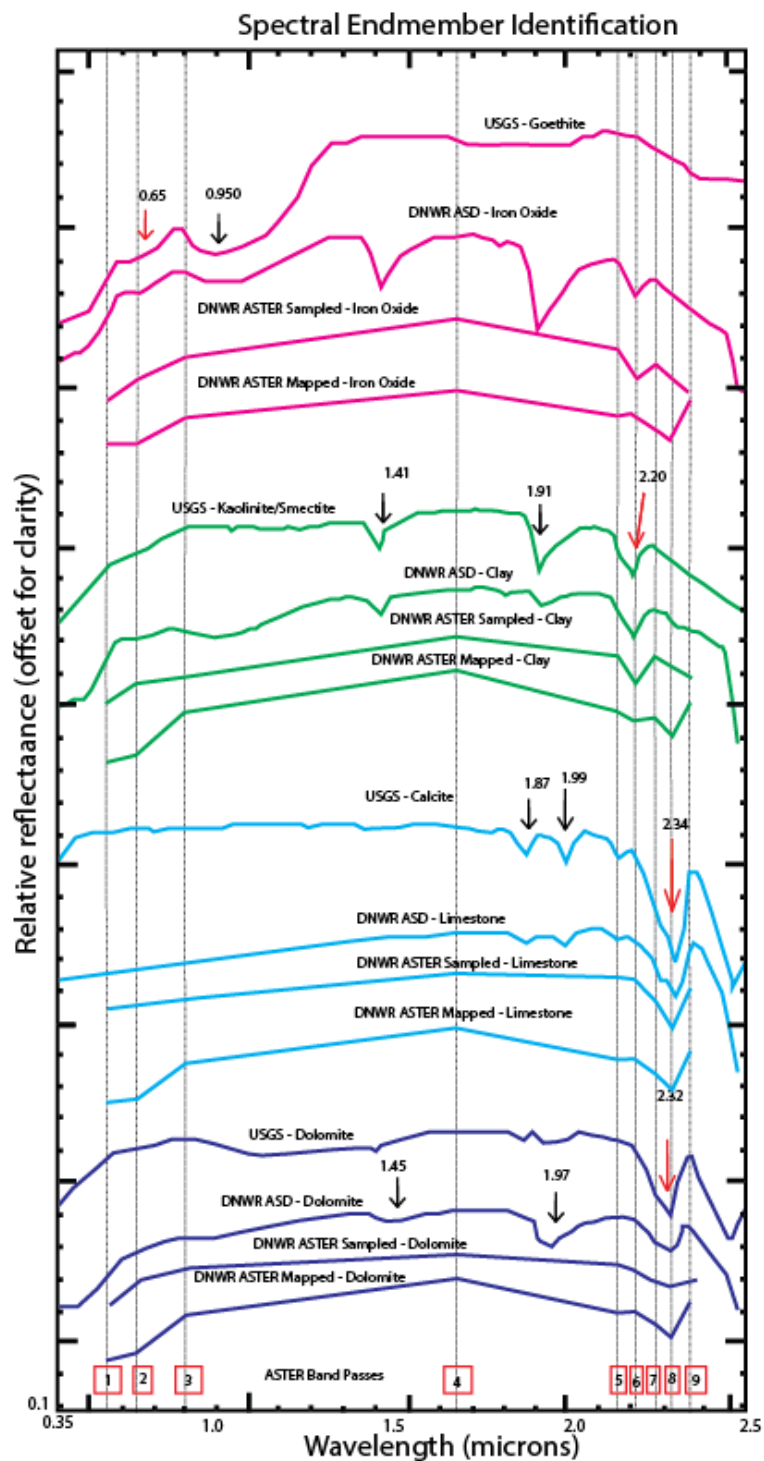


Figure 32: USGS mineral spectral library, ASD collected DNWR sample spectra, and ASD sample spectra resampled to ASTER wavelengths shown. Key spectral features used for identification are noted with arrows and approximate wavelengths used for identification in ASD samples. Red arrows note features that can be resolved at ASTER spectral resolution. Black arrows note features only resolved at ASD and library spectral resolution. “ASTER Mapped” profiles are generated from the average spectral profile of mapped end members shown in Figure 28 in the Gass Peak district.

4.3.2 TIR (Lab and ASTER)

Shown in Figure 33 are four spectral profiles: quartzite sandstone, chert, limestone, and dolomite. The TIR spectra from the Nicolet apparatus are shown below the spectra resampled to ASTER TIR band passes, which are centered at 8.3 μm , 8.65 μm , 9.1 μm , 10.6 μm , and 11.3 μm (Figure 33).

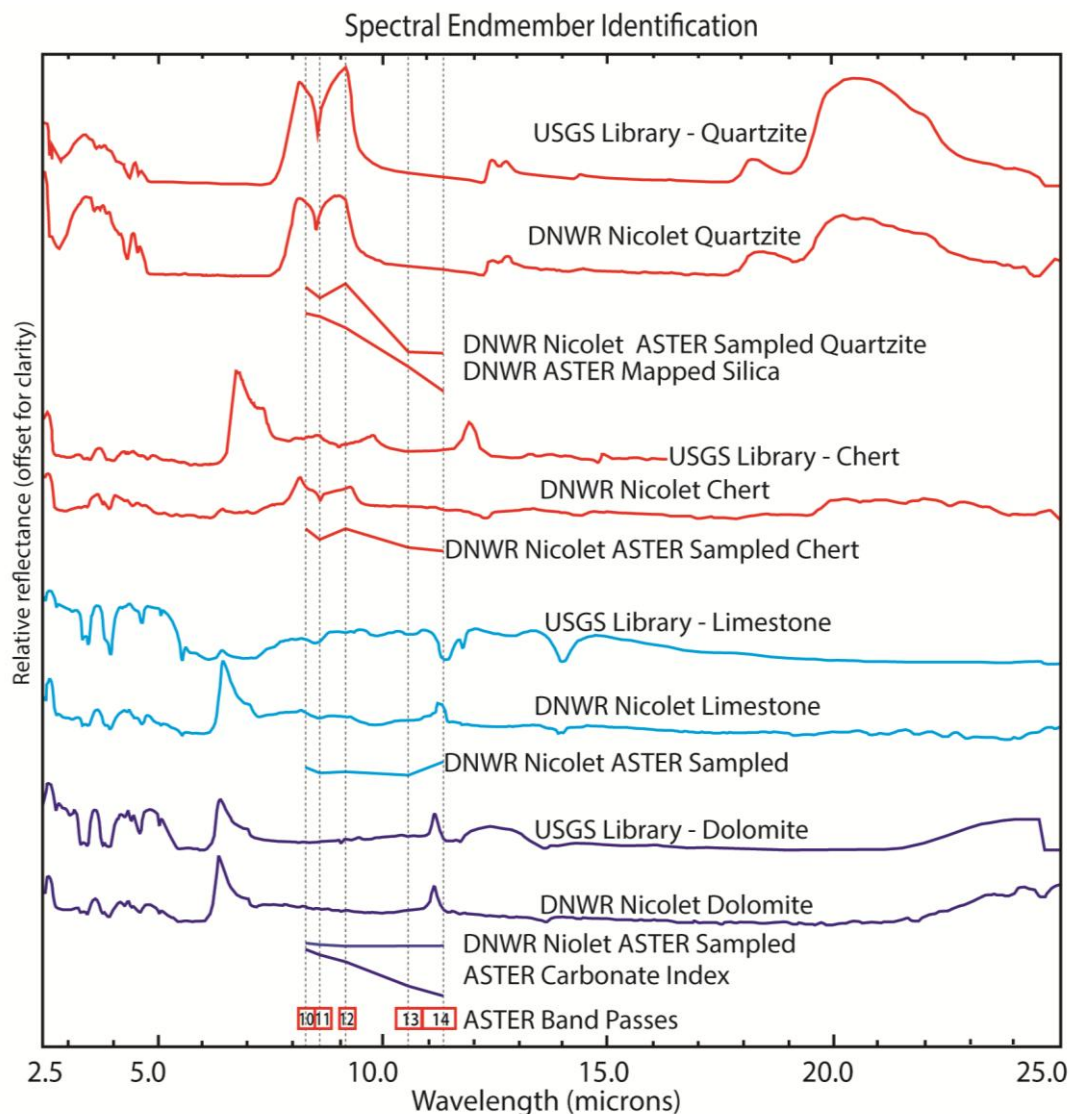


Figure 33: TIR spectral collected on a Thermo Nicolet spectrometer between 2.5 and 25.0 μm ASTER sampled spectral is shown above. Note the “ASTER Carbonate Index” is not a result from the final mapped end member, but from the carbonate index results used during mineral likelihood mapping. Chert spectra reflects a carbonate and silica composition. Note the strong silica absorbance feature at band 11 in the quartzite rocks is also present in the DNWR Nicolet Chert spectra.

5.0 Discussion

Evaluation of field targets selected from mineral likelihood maps similar to Figure 16 and the final mapping in Figures 27-31 indicate the spectral response is largely a result of the primary mineralogy of unaltered rocks and stratigraphic units, rather than minerals formed by hydrothermal alteration. Band ratio images generated from both Landsat ETM+ and ASTER processing highlight subtle, but continuous, compositional differences in rock units such as those found between the limestone and dolostone carbonate rocks, but fail to identify specific lithologic classes. Mineral likelihood maps, final end member maps, and band ratio images typically highlight compositional differences which are concordant with lithologic features from both field observations and geologic maps.

5.1 Landsat ETM+ Results

Landsat ETM+ band ratio images such as Figure 18 through Figure 21, and those found in the Appendix A, highlight a variety of ground cover types and can be used to map the extent of geologic units and alteration; however, the spectral resolution of the sensor is too coarse to be useful beyond identifying generalized lithologic and alteration contacts and lineaments.

In Figure 18 much of the north trending Sheep Range is mapped in hot to warm (red-orange-yellow) pixels; since this image maps the combination of iron oxide, clay alteration, and gossan bearing rocks as red and green pixels, the band ratios here suggest that region is dominated by iron bearing units. The boundaries of this anomaly correlate best with the elevation of pinyon and juniper forests, which typically grow above 1.8 km

in the DNWR, with higher elevations generally more densely vegetated. Vegetation has high reflectance in the SWIR portion of the EM spectrum, mineral mapping over such areas should be viewed with skepticism and field validation is needed to improve confidence in remote mapping of such areas.

Figure 20 provides zoomed imagery from Figure 18 but focused in the southern DNWR, the overlain, structural, and lithologic contact line work helps to emphasize the capabilities of using Landsat ETM+ band ratios to map contacts. The cool (blue-purple-magenta) colors, which typically correlate with Mississippian and Devonian carbonate units are the same areas where most of the historical mine workings were found, including the June Bug mine (Figure 4).

Evaluation of these methods found that simple band ratio combinations, sometimes combined with a principle component stretch (PC), are most successful at displaying meaningful information from the Landsat ETM+ imagery; however, the spectral resolution of this sensor does not provide sufficient data to map zones of hydrothermal alteration. The other Landsat ETM+ images can be found in Appendix A.

5.2 ASTER Results

5.2.1 ASTER Processing and Band Ratio Images

As discussed above, data artifacts in the ASTER scenes such as Figure 15 can create areas of ambiguity in the final products. To remediate these internal inconsistencies, areas of discontinuous pixels are separated out and processed individually during final mapping procedures. This allows the operator to guide processing along image boundaries, creating a more consistent and reliable end product. As with the Landsat ETM+ data product, heavily vegetated areas should be evaluated

with care. Additionally, alluvium and alluvial fans, which are comprised of erosional material from the ranges, create areas of high albedo, and thus high reflectance in remote sensing images, resulting in adjacent pixels with spectrally differing signals. Alluvial deposits can be seen as the large portions of the bright yellow and orange mottled areas dominating the southeast portion of Figure 22 and Figure 23. These mottled areas can easily be confused with the yellow and orange areas in the Lake Mine area, in the north and north east portion of the figures, which look similar. When compared to the geologic map and field checked, these regions were actually delineating unique lithologic units, Mississippian and Devonian units and localized alteration in the Lake Mine area in the Bonanza King Formation. To account for the variable response of the alluvial fan deposits a mask was used to concentrate the study strictly to outcrops during the final end member processing.

5.2.2 ASTER Mineral Distribution Mapping

Zones classified as iron oxide (limonite) in the image, which can elsewhere be related to the weathering of sulfides in metallic mineral deposits, are most often restricted to Tertiary volcanic rocks in the northeast and outcropping Bonanza King Formation, throughout much of the Sheep Range. Field checks found that these locations are largely unaffected by hydrothermal alteration. Only Tertiary volcanic rocks with local, minor iron staining due to weathering, were observed. Yellow goethite staining was observed in much of the Lake Mine area, but the spectral mapping appears to be dominated by the carbonate host rocks, localized iron oxides, and scattered silica and clay areas.

Clay minerals, which should be expected in hydrothermal alteration zones, crop out in only a few areas in the processed imagery. Field checks indicated clays are generally related to local shale, siltstones, clay-rich partings on thin-bedded limestone, and localized weak alteration within or adjacent to small (1-2 meter) fault zones. Most often, little more than bleached rock with weak decalcification is present. The exception is the Lake Mine area at the north east end of the Sheep Range, west of the northern extent of the Gass Peak thrust fault, (Figure 27, Figure 28, and Figure 34 box A.), here Bonanza King Formation rocks host local hydrothermally altered clay minerals commonly associated with ore zones. The ASD Terraspec allowed specific clay minerals to be identified in the Lake Mine area, including scattered samples of kaolinite and dickite, and more extensively illite and montmorillonite. All of these clay minerals may be found in association with hydrothermal environments, though dickite is the only one formed almost exclusively from hydrothermal alteration. Kaolinite and montmorillonite can form in hydrothermal environments as well as during weathering processes and illite can form during hydrothermal alteration, but generally not weathering. The presence of this suite of clay minerals in close proximity to each other is good evidence for hydrothermal activity in the area, with the extent of clay minerals marking the extent of alteration. The boundaries of alteration are well defined in both Landsat ETM+ and ASTER band ratio images (Figure 17 and Figure 18 (Landsat ETM+) and Figure 21 and Figure 22 (ASTER)). The final mapping products, (Figure 27 and Figure 28), resulted in only scattered-rare pixels of iron oxide and clay alteration in the Lake Mine area, however, the region was well defined by the limestone end member. Though the alteration mapped by remote sensing was somewhat less than suggested by field

observations, the SAM algorithm classifies each pixel as only one end member and field observations found that although much of the rock exhibits some degree of alteration and bleaching, the alteration of limestone was incomplete in the region. This is likely reflected in the spectral response over the area as well as the SAM map results.

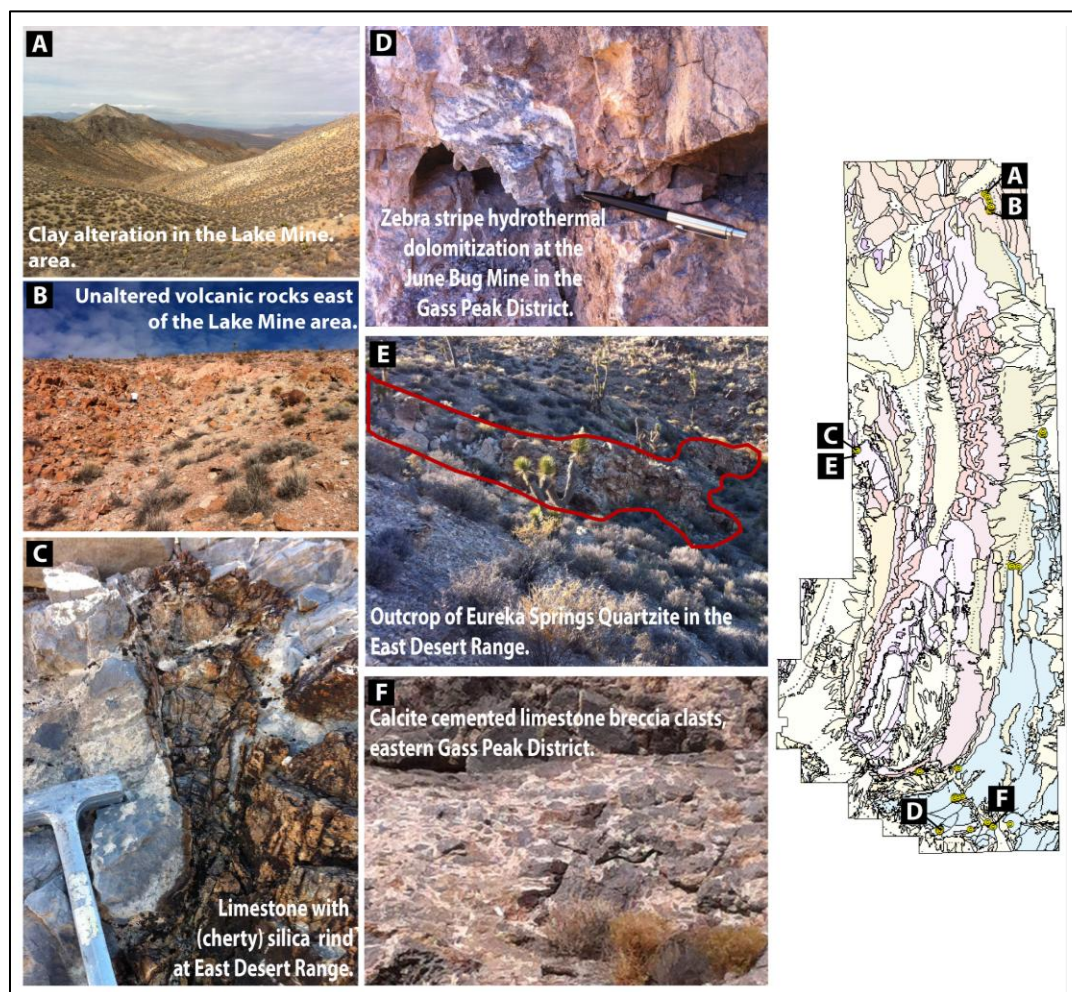


Figure 34: Photos from field validation with locations of boxes correlating to the simplified geologic map with field locations in yellow, to the right.

Field checks of silica anomalies identified from the TIR bands indicate the presence of silica-rich lithologies such as chert and quartzite (Figure 35 Box C and Box E) these were mapped successfully in the final mineral distribution product (Figure 27). In Figure 28 a scattering of silica pixels can be seen mapped in the Lake Mine area where

variably developed silicification and true jasperoids were observed in the alteration zone. Additionally rocks that appeared to be quartzite were also locally exposed. False silica anomalies were encountered at the northern extent of the Las Vegas Range, there dark gray, flat lying dolomite, was encountered when field checking isolated pixels along the ridge tops. In the East Desert Range (Figure 29) anomalies within the Eureka Quartzite are so well constrained that the 90 m TIR pixels show local strike-slip offsets of less than 100 m. This can also be seen in the green lineations trending northwest in the East Desert Range on northwest portion of the map area shown in Figure 35 box B, as well as the light green, northeast trending, linear cluster of pixels, on the western side of the Las Vegas Range (Figure 35 box C), these pixels correlate to Sterling Quartzite Formation rocks from the geologic map (Page et al., 2005).

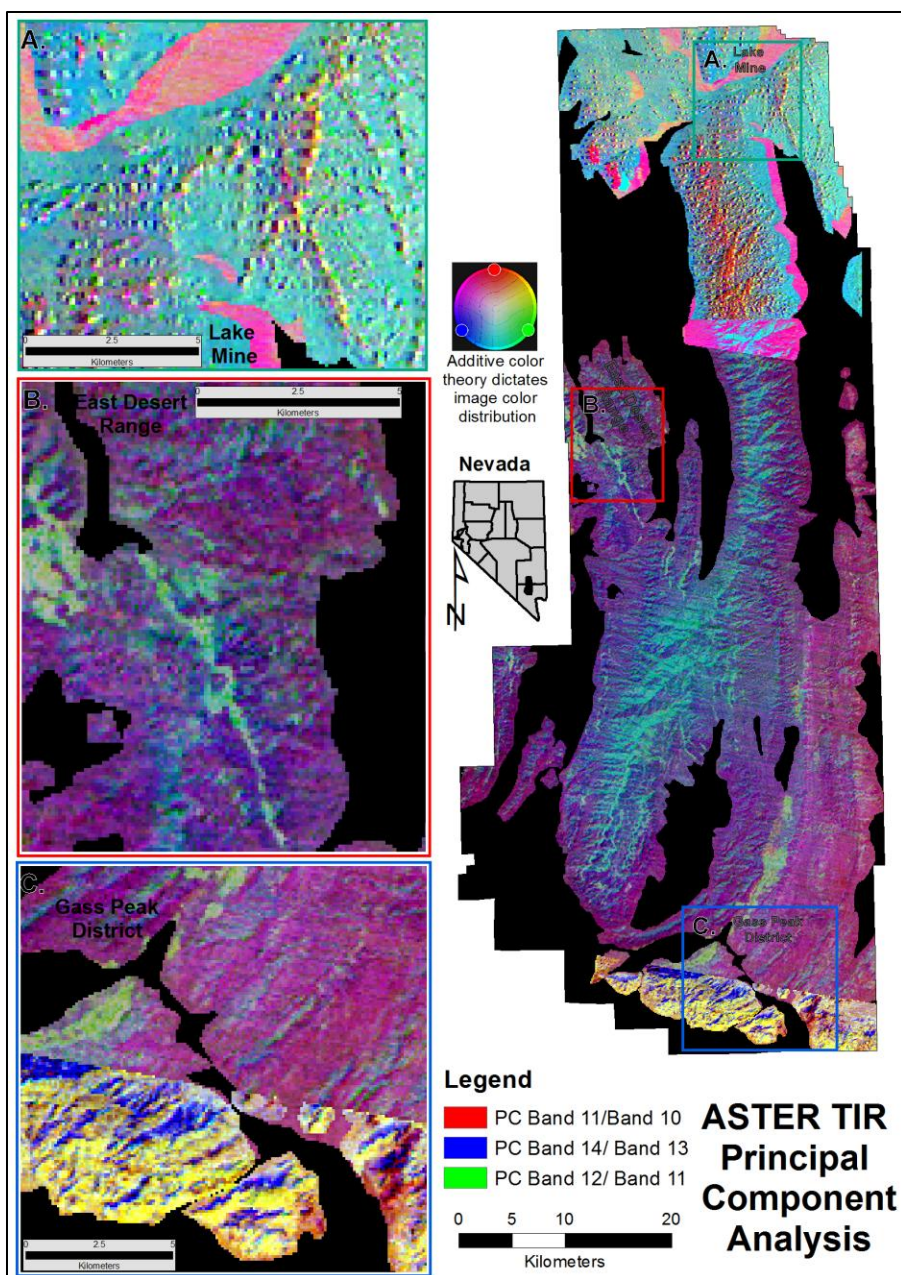


Figure 35: TIR PCA band ratio image. Red-Band 11/Band 10 is intended to highlight silica, blue-Band 14/Band 13 ratio is a carbonate inverse ratio (intended to subdue carbonate background response), and the green-Band12/Band11 is another silica band ratio. The principal component analysis statistically increases signal while subduing noise in the data. The resulting data set typically highlights the desired feature and decreases background interference, but as a consequence the color combinations may not correlate with the initial input colors and will not be consistent across multiple scenes as seen in the differences in boxes A, B, and C. Field observations found few exposed silica rocks in the Lake Mine this area box A does not appear to highlight useful information. Green colored pixels in box B and the northwest quadrant of box C highlight lithologic silica, Eureka Quartzite, in box B and Sterling Quartzite and chert observed in some sections of the Bird Spring Formation in box C. Yellow and blue in the southern portion of box C represents carbonate rocks, and reddish hues in the southeast appear to map exposed chert rocks.

Hydrothermal dolomite, which is associated with mineralization in the Gass Peak District, only shows as sporadic dolomite-dominant pixels in both remote sensing images and outcrop during field checks (Figure 21, Figure 24, and 35 Box D). Local calcite cemented, limestone breccia, such as that shown in Figure 35 Box F, are present; primarily adjacent to faulting. The imagery confirms the absence of a large zone of pervasive hydrothermal dolomitization, which would be expected to be associated with large carbonate-hosted base metal deposits. A portion of the Gass Peak District in the northwest corner of Figure 30 does show a contiguous cluster of pixels mapped as clay, suggesting a previously unidentified and altered area may be present in this region.

Limestone was mapped extensively in the DNWR and is the most common rock unit in the area of interest. Limestone was observed near almost all field validation sites (excluding Tertiary volcanic dominated locations, which were generally observed to be large, unaltered and continuous units (Figure 35 Box B). Lithologic dolostone members in Cambrian, Ordovician, Silurian and Devonian carbonate rocks are known to be present within the DNWR. The results from the SAM algorithm and final mineral mapping products do not appear to have differentiated these formations. As can be seen in the ASTER sampled reference spectra in Figure 32, dolomite and calcite spectra, sampled at ASTER band passes will have very similar spectral response; this has likely resulted in dolomite units falsely identified as limestone (calcite). This suggests that ASTER is probably not effective for mapping the extent of hydrothermal dolomitization observed at the DNWR.

As discussed above silica anomalies generally corresponded with outcrops of silica rich bedrock such as Eureka Quartzite, as shown in Box E, Figure 35, or chert sections of the Bird Springs Formation; however, some of the field checked silica anomalies found carbonate bedrock, typically Paleozoic limestone units, which contained local cherty silica rinds, such as those shown in Figure 35 Box C and described by others in the geologic background of this text. These rinds were generally 5-20 mm thick with a discrete boundary with the carbonate host rock. In some locations the chert rinds had a preferred orientation along faults and fractures, though more often they were comprised of 5 cm to 0.5 m amorphous, somewhat lenticular, bedding parallel features. Locally they may account for 10-25% of the exposed rock surface, enough to potentially result in anomalous silica mapping in the ASTER imagery, however these features are typically not continuous enough to result in laterally continuous pixels at ASTER resolutions.

The Tertiary volcanic rocks in the northeastern Sheep Range were generally mapped with silica, dolomite, and clay pixels Figure 28. Observations found the rocks to be primarily unaltered with 10-20% phenocrysts (mostly quartz, biotite, and hornblende) and 80-90% matrix (quartz and volcanic glass), with only a fraction of the phenocrysts comprised of quartz crystals. The presence of quartz in the matrix and other silicate minerals like phyllosilicates and amphiboles may contribute to the spectral response indicating silica. In the southern Pahranaagat Range, shown in Figure 28, Tertiary volcanic units mapped as clay end members may indicate regions of hydrothermal activity. The Pahranaagat Shear Zone, known to be active in this region during the Tertiary, may be responsible for activating, or reactivating, faulting in the area, providing fluid conduits for any hydrothermal activity (Muntean et al., 2014). Field observations

found no evidence of exposed dolomite in the volcanic units in the northeast. These false positives may be present in part due to spectral similarities between biotite and dolomite, which have major spectral features at 2.328 and 2.338 microns respectively (Hauff, 2000).

5.3 Spectrometry

The spectral end member profiles shown in Figure 32 and Figure 33 represent a sample of the data analyzed. Thermo Nicolet sampling requires additional sample preparation making it impractical to utilize when sample identification has been completed using the ASD Terraspec and traditional mineral and rock identification methods.

In addition to helping identify specific clay mineral constituents, otherwise impossible to identify with Landsat ETM+ or ASTER, both the ASD Terraspec and the Thermo Nicolet spectra show examples of spectral mixing, which can obscure remote sensing results since the mapping algorithm is required to classify each pixel as only one end member. The limonite minerals goethite, hematite, and jarosite are all identified by distinctive absorption features in the VNIR color bands, specifically at 0.65 and 0.95 microns, but not in the SWIR (Hauff, 2000). Multiple minerals can often be identified in a single spectrum, as is the case for the iron oxide sample from Figure 32; the absorption features near 1.41 and 1.19 microns and 2.20 microns are more closely associated with clay minerals, possibly smectite. This spectral mixing can cause ambiguity among samples and can present obvious challenges when using the mineral mapping algorithms presented in this study.

The laboratory TIR spectra shown in Figure 33, was collected for integration with remote mapping algorithms and comparison with reference spectra. The quartzite, chert, limestone, and dolostone samples with spectral plots shown in Figure 33 were first identified using traditional mineral identification methods then compared to the USGS reference library spectra. The limestone and dolomite spectra are differentiated primarily using the 10.6 micron feature, this feature is strong enough for ASTER band passes to potentially capture the difference and differentiate the carbonate end members during mineral mapping; however, the 90 m pixels in the TIR bands appear to be too broad to spectrally identify pure samples of dolostone resulting in only a differentiation between silica and carbonate rocks in the TIR ASTER scenes. Chert and quartzite were also analyzed using the Thermo Nicolet spectrometer, both are easily identifiable in hand specimen; however, the chert sample profile has distinct features, which correlate well with the 10.6 micron feature indicative of dolomite, this is another example of spectral mixing of end members and effectively pollutes the ASTER end member spectra shown in Figure 33.

6.0 Conclusions

- No significant hydrothermal alteration systems was detected in this study suggesting there are no large mineral deposits in the DNWR.
- This study shows that the sensors and methods utilized over the DNWR effectively map lithologic and structural features by highlighting different mineral classes; furthermore, these methods can effectively guide field exploration in arid regions and be used to prioritize areas of both high and low mineral potential.

- Over smaller study areas needing only one 60km X 60km ASTER scene, preliminary band ratio false color images can be generated quickly (a few hours) and focused mineral mapping may be possible within a few days to a week depending on the size of the area, the diversity of the AOI, the desired final product(s), and confidence desired.
- Future mineral assessments and exploration should consider remote sensing studies when evaluating poorly studied, large, remote, and arid areas. Heavily vegetated areas will require more thorough field investigation as false positives are more common in areas of mixed ground cover.

References

- Agar, B., 2010. ASTER Alteration Mineral Mapping: Las Pampas, Cajamarca, Peru for B and G Mining S.A.C.
- Adams, J.B., Smith, M.O., Gillespie, A.R., 1993. Imaging spectroscopy: interpretation based on spectral mixture analysis. In: Pieters, C.M., Englert, P.A.J. (Eds.), *Remote Geochemical Analysis: Elemental and Mineralogical Composition*. Cambridge University Press, New York, pp. 145–166.
- Arehard, G.B., Chakurian, A.M., Tretbar, D.R., Christensen, J.N., McInnes, B.A., and Donelick, R.A., 2003, Evaluation of Radioisotope Dating of Carlin-Type Deposits in the Great Basin, Western North America, and implications for Deposit Genesis: *Economic Geology*, v. 98, p. 235-248.
- Anderson, R.Ernest, compiler, 1999, Fault number 1122, Maynard Lake fault, in Quaternary fault and fold database of the United States: U.S. Geological Survey website, <http://earthquakes.usgs.gov/hazards/qfaults>, accessed 08/02/2014 12:34 AM.
- Ashley, R. P., & Abrams, M. J., 1980. Alteration Mapping Using Multispectral Images- Cuprite Mining District, Esmeralda County, Nevada. U.S. Geological Survey Open File Report 80-367, Pages 1-26.
- Baldrige, A. M., S.J. Hook, C.I. Grove and G. Rivera, 2009.. The ASTER Spectral Library Version 2.0. *Remote Sensing of Environment*, vol 113, pp. 711-715.
- Bierwith, P.N., (2002). Evaluation of ASTER satellite data for geological applications. Consultancy Report to Geoscience Australia, 50 pp.
- Boardman, J.W., 1993. Automated Spectral Unmixing of AVIRIS Data Using Convex Geometry Concepts: in *Summaries, Fourth JPL Airborne Geoscience Workshop*.
- Boardman, J.W., 1998. Leveraging the high dimensionality of AVIRIS data for improved sub-pixel target unmixing and rejection of false positives: mixture tuned matched filtering. *Summaries of the Seventh Annual JPL Airborne Geoscience Workshop*, Pasadena, CA, p. 55.
- Boardman, J.W., Kruse, F.A., Green, R.O., 1995. Mapping target signatures via partial unmixing of AVIRIS data, summaries. *Proceedings of the Fifth JPL Airborne Earth Science Workshop*, 23–26 January, Pasadena, California, JPL Publication 95–1, vol. 1, pp. 23–26.
- Buchanan, L.J., 1981, Precious, metal deposits associated with volcanic environments in the Southwest: *Arizona Geological Society Digest* 14, p. 237-262

- Clark, R.N., Swayze, G.A., Gallagher, A.J., King, T.V and, Calvin, W.M. (1993). The U. S. Geological Survey, Digital Spectral Library: Version 1: 0.2 to 3.0 microns, U.S. Geological Survey Open File Report 93-592, 1340 pages.
- Clark, R.N., (1999), "Spectroscopy of Rocks and Minerals and Principles of Spectroscopy": in Remote Sensing for the Earth Sciences, Manual of Remote Sensing, 3rd Ed., Vol. 3 Chapter 1, through section 1.3, pp. 3-28. John Wiley and Sons, Inc.
- Cline, J.S., Hofstra, A.H., Muntean, J.L., Tosdal, R.M., and Hickey, K.A., 2005. Carlin-Type Gold Deposits in Nevada: Critical Geological Characteristics and Viable Models. Economic Geology 100th Anniversary Volume, p. 451-484.
- Crouch, Stanley; Skoog, Douglas A. (2007). Principles of instrumental analysis. Australia: Thomson Brooks/Cole.
- Crowley, J.K., Brickey, D.W., Rowan, L.C., 1989. Airborne imaging spectrometer data of the Ruby Mountains, Montana: mineral discrimination using relative absorption band-depth images. Remote Sens. Environ. 29, 121-134.
- Duebendorfer, E.M., and Black, R.A., 1992, The kinematic role of transverse structures in continental extension: An example from the Las Vegas Valley shear zone, Nevada: Geology , v. 20, p. 87-90.
- Guilbert, John M and Park, Charles F. 2007. The Geology of Ore Deposits. Long Grove, IL: Waveland Press. Print.
- Gabr, S., Ghulam, A., Kusky, T., 2010. Detecting Areas of High-potential Gold Mineralization Using ASTER Data. Ore Geology Reviews, v. 38, p. 59-69.
- Goetz, A.F.H., Rock, B.N., Rowan, L.C., 1983. Remote sensing for exploration: an overview. Econ. Geol. 78, 573-590.
- Green, A.A., Berman, M., Switzer, P., Craig, M.D., 1988. A transformation for ordering multispectral data in terms of image quality with implications for noise removal. IEEE Trans. Geosci. Remote Sens. 26 (1), 65-74.
- Hauff, P., 2000. Applied Reflectance Spectroscopy with Emphasis on Data Collection and Data Interpretation Using the PIMA-II Spectrometer. Spectral International Inc.

- Harris, J. R., Rencz, A. N., Ballantyne, B., & Sheridan, C., 1998. Mapping Altered Rocks Using Landsat TM and Lithogeochemical Data: Sulphurets-Brucejack Lake District, British Columbia, Canada. *Photogrammetric Engineering & Remote Sensing*, v. 4, p 1-14.
- Harsanyi, J.C., Farrand, W.H., Chang, C.I., 1994. Detection of subpixel signatures in hyperspectral image sequences. *Proceedings of 1994 ASPRS Annual Conference*, Reno, Nevada, pp. 236–247.
- Hewett, D., 1931. Geology and ore deposits of the Goodsprings quadrangle, Nevada. U.S. Geological Survey, Professional paper 162.
- Hewson, R.D., Cudahy, T.J., Huntington, J.F., 2001. Geologic and alteration mapping at Mt Fitton, South Australia, using ASTER satellite-borne data *IEEE 2001 International geoscience and remote sensing symposium*, 9–13 July (2001).
- Hofstra, A.H., Snee, L.W., Rye, R.O., Folger, H.W., Phinisey, J.D., Loranger, R.J., Dahl, A.R., Naeser, C.W., Stein, H.J., and Lewchuk, M., 1999, Age constraints on Jerritt Canyon and Other Carlin-Type Gold Deposits in the Western United States—Relationship to Mid-Tertiary extension and Magnetism: *Economic Geology*, v. 94, p. 769-802.
- Inzana, J., Kusky, T., Higgs, G., Tucker, R., 2003. Supervised Classifications of Landsat ‘TM’ Band Ratio Images and Landsat ‘TM’ Band Ratio Image with Rada for Geological Interpretations of Central Madagascar. *Journal of African Earth Sciences*, v. 37, p. 59-72.
- Kääb, C. Huggel, F. Paul, R. Wessels, B. Raup, H. Kieffer and J. Kargel 2002: Glacier Monitoring from ASTER Imagery: Accuracy and Applications. *EARSel Proceedings. LIS-SIG Workshop*. Berne, March 11-13, 2002.
- Kääb, 2005 Remote sensing of mountain glaciers and permafrost creep, *Physical Geography Series*, Zurich, 48, 266 pages, 3-85543-244-9
- Kuehn, C.A. and Rose, A.W., 1992, Geology and Geochemistry of Wall-Rock alteration at the Carlin-type Gold Deposit, Nevada: *Economic Geology*, v. 87, 1697-1721.
- Kruse, F.A., Boardman, J.W., Lefkoff, A.B., Heidebrecht, K.B., Shapiro, A.T., Barloon, P.J., Goetz, A.F.H., 1993. The Spectral Image Processing System (SIPS)—interactive visualization and analysis of imaging spectrometer data. *Remote Sens. Environ.* 44, 145–163.
- "Landsat." *Landsat*. N.p., n.d. Web. 13 Aug. 2013. <http://landsat.usgs.gov/>.

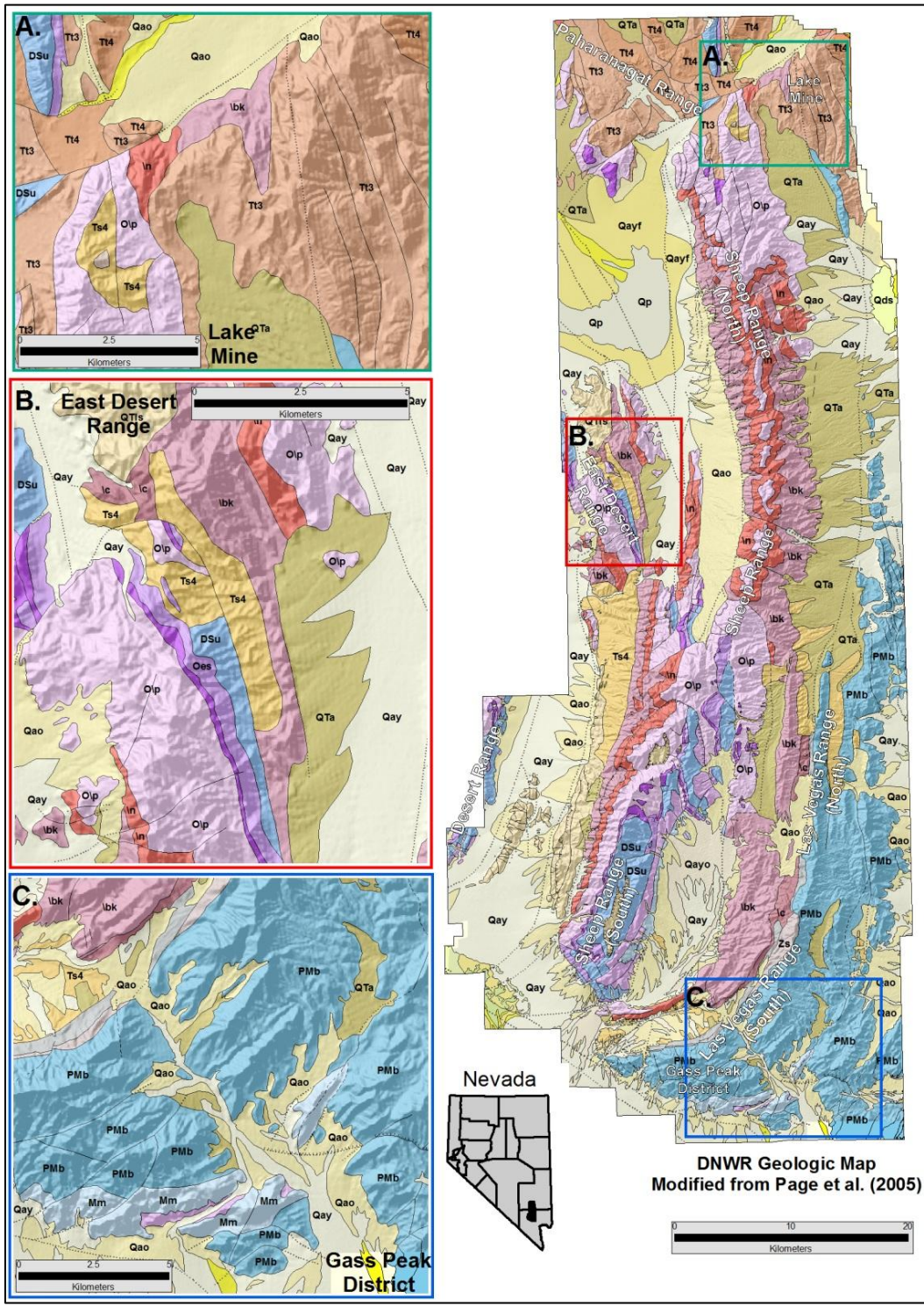
- Leach, D.L., Taylor, R.D., Fey, D.L., Diehl, S.F., and Saltus, R.W., 2010, A deposit model for Mississippi Valley-Type lead-zinc ores, chap. A of Mineral deposit models for resource assessment: U.S. Geological Survey Scientific Investigations Report 2010–5070–A, 52 p.
- Longwell, C. R., Pampeyan, E. H., Bowyer, B., & Roberts, R. J., 1965. Geology and mineral deposits of Clark, Nevada. NBMG Bulletin. Retrieved from <http://www.nbmng.unr.edu/sales/davescans/bull70.pdf>
- Longwell, C.R., 1974. Measure and Date of Movement on Las Vegas Valley Shear Zone, Clark County, Nevada. Geological Society of America Bulletin, v. 85, p. 985-990.
- Long, S.P., 2012, Magnitudes and spatial patterns of erosional exhumation in the Sevier hinterland, eastern Nevada and western Utah, USA: Insights from a Paleogene paleogeologic map: *Geosphere*, v. 8, p. 881-901, doi: 10.1130/GES00783.1.
- Muntean, J., Hinz, N., Cramer, T., Davis, D., Dering, G., Sladek, C., 2014. An Updated Mineral and Energy Resource Assessment of the Desert National Wildlife Range, Clark and Lincoln Counties, NV, Draft Report. Nevada Bureau of Mines and Geology, University of Nevada.
- Mars, J.C., Rowan, L.C., 2006. Regional mapping of phyllic- and argillic-altered rocks in the Zagros magmatic arc, Iran, using Advanced Spaceborne Thermal Emission and Reflection Radiometer (ASTER) data and logical operator algorithms. *Geosphere* 2, 161–186.
- NASA Land Processes Distributed Active Archive Center (LP DAAC). ASTER L1B. USGS/Earth Resources Observation and Science (EROS) Center, Sioux Falls, South Dakota. 2001.
- Nevada Bureau of Mines and Geology (NBMG). 2012. Nevada Bureau of Mines and Geology Special Publication MI-2012. The Nevada Mineral Industry.
- Ninomiya, Y., 2003a. A stabilized vegetation index and several mineralogic indices defined for ASTER VNIR and SWIR data. Proc. IEEE 2003 International Geoscience and Remote Sensing Symposium (IGARSS'03) Vol. 3, Toulouse, France, 21–25 July 2003, pp. 1552–1554.
- Ninomiya, Y., 2003b. Advanced remote lithologic mapping in ophiolite zone with ASTER multispectral thermal infrared data. Proc. IEEE 2003 International Geoscience and Remote Sensing Symposium (IGARSS'03) Vol. 3, Toulouse, France, 21– 25 July 2003, pp. 1561–1563.

- Ninomiya, Y., Fu, B., Cudahy T., 2005. Detecting Lithology with Advanced Spaceborne Thermal Emission and Reflection Radiometer (ASTER) Multi-Spectral Thermal Infrared "Radiance-at-Sensor" Data. *Remote Sensing of Environment* V. 99 (2005), p. 127-139.
- Ninomiya, Y.; Bihong Fu, "Spectral indices for lithologic mapping with ASTER thermal infrared data applying to a part of Beishan Mountains, Gansu, China," *Geoscience and Remote Sensing Symposium*, 2001. IGARSS '01. IEEE 2001 International , vol.7, no., pp.2988,2990 vol.7, 2001 doi: 10.1109/IGARSS.2001.978231
- Oskouei, M. M., & Busch, W., 2012. A selective combined classification algorithm for mapping alterations on ASTER data. *Applied Geomatics*, V. 4 .1, p. 47-54. Doi:10.1007/s12518-012-0077-1
- Page, W.R., Dixon, G.L., Rowley, P.D., and Brickey, D.W., 2005, Geologic map of parts of the Colorado, White River, and Death Valley groundwater flow systems, Nevada, Utah, and Arizona: Nevada Bureau of Mines and Geology Map 150, scale 1:250,000, 1 sheet, 23 p.
- Patel, N. and Rampal, K.K., 1992. Discrimination of Rock Types Using Landsat Thematic Mapper Data. *Advanced Space Research*, v. 12, issue 7, p. 35-38.
- Pour A.B. and Hashim M., 2012, The Application of ASTER Remote Sensing Data to Porphyry Copper and Epithermal Gold Deposits. *Ore Geology Reviews*. Vol. 44. p. 1-9.
- Rowan, L.C., Goetz, A.F.H., Ashley, R.P., 1977. Discrimination of hydrothermally altered and unaltered rocks in visible and near infrared multispectral images. *Geophysics* 42 (3), 522–535.
- Rowan, L.C., Mars, J.C., 2003. Lithologic Mapping in the Mountain Pass, California Area Using Advanced Spaceborne Thermal Emission and Reflection Radiometer (ASTER) Data. *Remote Sensing of the Environment*, v. 84, p. 350-366.
- Rowan, L.C., Hook, J.C., Abrams, M.J., Mars, J.C., 2003. Mapping of Hydrothermally Altered Rocks at Cuprite, Nevada, Using the Advanced Spaceborne Thermal Emission and Reflection Radiometer (ASTER), A New Satellite-Imaging System. *Economic Geology*, v. 98, p. 1019-1027.
- Rowan, L.C., Schmidt, R.G., Mars, J.C., 2006. Distribution of Hydrothermally Altered Rocks in the Reko Diq, Pakistan Mineralized Area Based on Spectral Analysis of ASTER Data. *Remote Sensing of the Environment*, v. 104, p. 74-87.

- Rowley, P.D., 1998, Cenozoic transverse zones and igneous belts in the Great Basin, western United States—Their tectonic and economic implications, in Faulds, J.E., and Stewart, J.H., eds., Accommodation zones and transfer zones—The regional segmentation in the Basin and Range province: Geological Society of America Special Paper 323, p. 195-228.
- Sabins, F.F., 1987. Remote Sensing Principles and Interpretation, 2nd edition. Freeman, New York.
- Sabins, F.F., 1999. Remote Sensing for Mineral Exploration. *Ore Geology Reviews*, v. 14, p. 157-183.
- Schilling, J.H., 1968, Molybdenum Resources of Nevada: Nevada Bureau of Mines and Geology Bulletin 79-3, 189 p.
- Sillitoe, R.H., 1993, Epithermal models: Genetic types, geometrical controls, and shallow features: Geological Association of Canada Special Paper 40. p.403-417.
- Sillitoe, R.H., and McKee, E.H., 1996. Age of supergene oxidation and enrichment in the Chilean porphyry copper province: *Economic Geology*.v.9. p-64-79.
- Sillitoe, R. H. "Porphyry Copper Systems." *Economic Geology* 105.1 (2010): 3-41.
- Simmons, S.F., Browne, P.R.L., 2000. Hydrothermal Minerals and Precious Metals in the Broadlands-Ohaaki Geothermal System: Implication for Understanding Low-Sulfidation Epithermal Environments. *Economic Geology*, v. 95, p. 971-999.
- Simmons, S.F., White, N.C., John, D.A., 2005. Geological Characteristics of Epithermal Precious and Base Metal Deposits. *Economic Geology* 100th Anniversary Volume, p. 485-522.
- Singh, A., Harrison, A., 1985. Standardized principal components. *Int. J. Remote. Sens.* 6, 883–896.
- Steven, A.T., and Ratte, J.C., 1960. *Geology and Ore Deposits of the Summitville District, San Juan Mountains, Colorado*. USGS Professional Paper-343. USGS. US Government Print Office.
- Stoffregen, R.E., 1987. Genesis of acid-sulfate alteration and Cu–Au–Ag mineralization at Summitville, Colorado. *Econ. Geol.* 82, 1575 – 1591.
- Thompson, A.J., Hauff, B., Robitaille, P.L., 1999. Alteration Mapping in Exploration: Application of Short-Wave Infrared (SWIR) Spectroscopy. *Society of Economic Geology, Newsletter*, v. 39, p. 16-27.

- Tingley, J.V., Castor, S.B., Garside, L.J., Bonham, H.F. Jr., Lugaski, T.P., Lechler, P.L., 1993. Energy and Mineral Resource Assessment of the Desert National Wildlife Range, Eastern Section: Clark and Lincoln Counties, Nevada. Reno, NV: Nevada Bureau of Mines and Geology, University of Nevada, Reno.
- Tschanz, C.M., Pampeyan, E.H., 1970. Geology and Mineral Deposits of Lincoln County, Nevada. Nevada Bureau of Mines and Geology Bulletin 73, p. 106-109 and selected tables/plates. United States, Department of the Interior, 2000/2013. Land Use Statistics from Department of the Interior, Washington D.C.
- U.S. Geological Survey, 2013. Mineral commodity summaries 2013: U.S. Geological Survey, 198 p.
- U.S. Fish and Wildlife Service, 2005. Desert National Wildlife Refuge Brochure. Desert National Wildlife Refuge, HCR 38 Box 700, Las Vegas, NV 89124.
- Van Der Meer, Freek D., Harald M.a. Van Der Werff, Frank J.a. Van Ruitenbeek, Chris A. Hecker, Wim H. Bakker, Marleen F. Noomen, Mark Van Der Meijde, E. John M. Carranza, J. Boudewijn De Smeth, and Tsehaie Woldai. "Multi- and Hyperspectral Geologic Remote Sensing: A Review." International Journal of Applied Earth Observation and Geoinformation 117 (2012): 112-28. Web.
- Vikre, P., Browne, Q., Fleck, R., Hofstra, A., & Wooden, J., 2011. Ages and Sources of Components of Zn- Pb, Cu, Precious Metal and Platinum Group Elements Deposits in the Goodsprings District, Clark County, Nevada. Economic Geology, v. 106, p. 1-32.
- Volesky, J.C.; R.J. Stern; and P.R. Johnson (2003) Geological control of massive sulfide mineralization in the Neoproterozoic Wadi Bidah shear zone, southwestern Saudi Arabia, inferences from orbital remote sensing and field studies, Precambrian Research, 123(2-4): 235-247.
- Wernike, B., Guth, P.L., Aken, G.J., 1984. Tertiary Extensional Tectonics in the Sevier Thrust Belt of Southern Nevada. Geological Society of American 1984 Annual Meeting, Reno, Guidebook, v. 4, p. 473-510.
- Watanabe, H., and Kazuaki M., 2003. Rock Type Classification by Multi-Band TIR of ASTER. Geosciences Journal, v. 7, No. 4, p. 347-58. Web.
- 43 U.S.C. 1714. United States Code, 2009 Edition. Title 43 – Public Lands Chapter 35 – Federal Land Policy and Management Subchapter II – Land Use Planning and Land Acquisition and Disposition. Sec 1714 – Withdrawals of lands from the U.S. Government Printing Office, www.gpo.

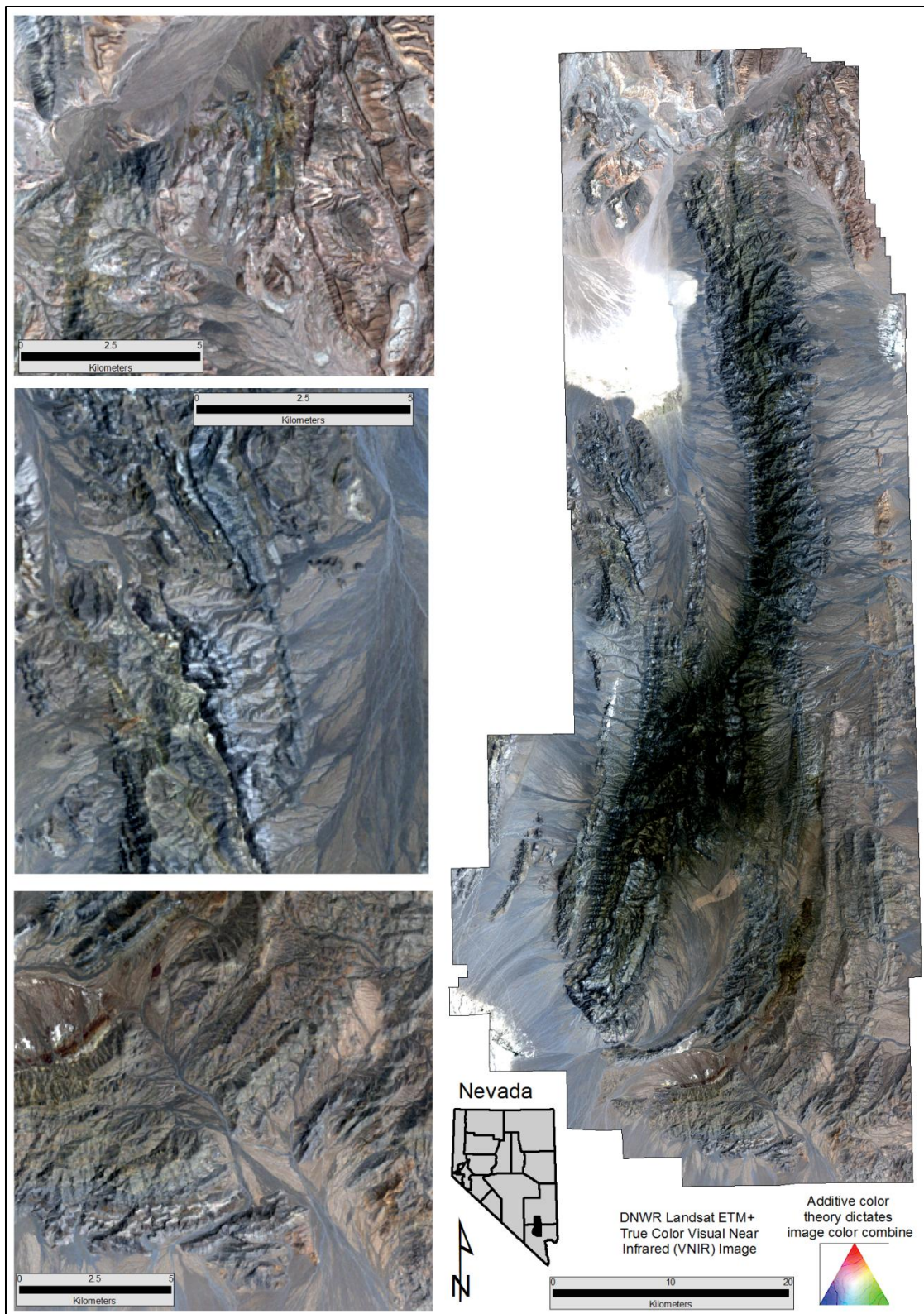
Appendix A – Band Ratio Composite Image



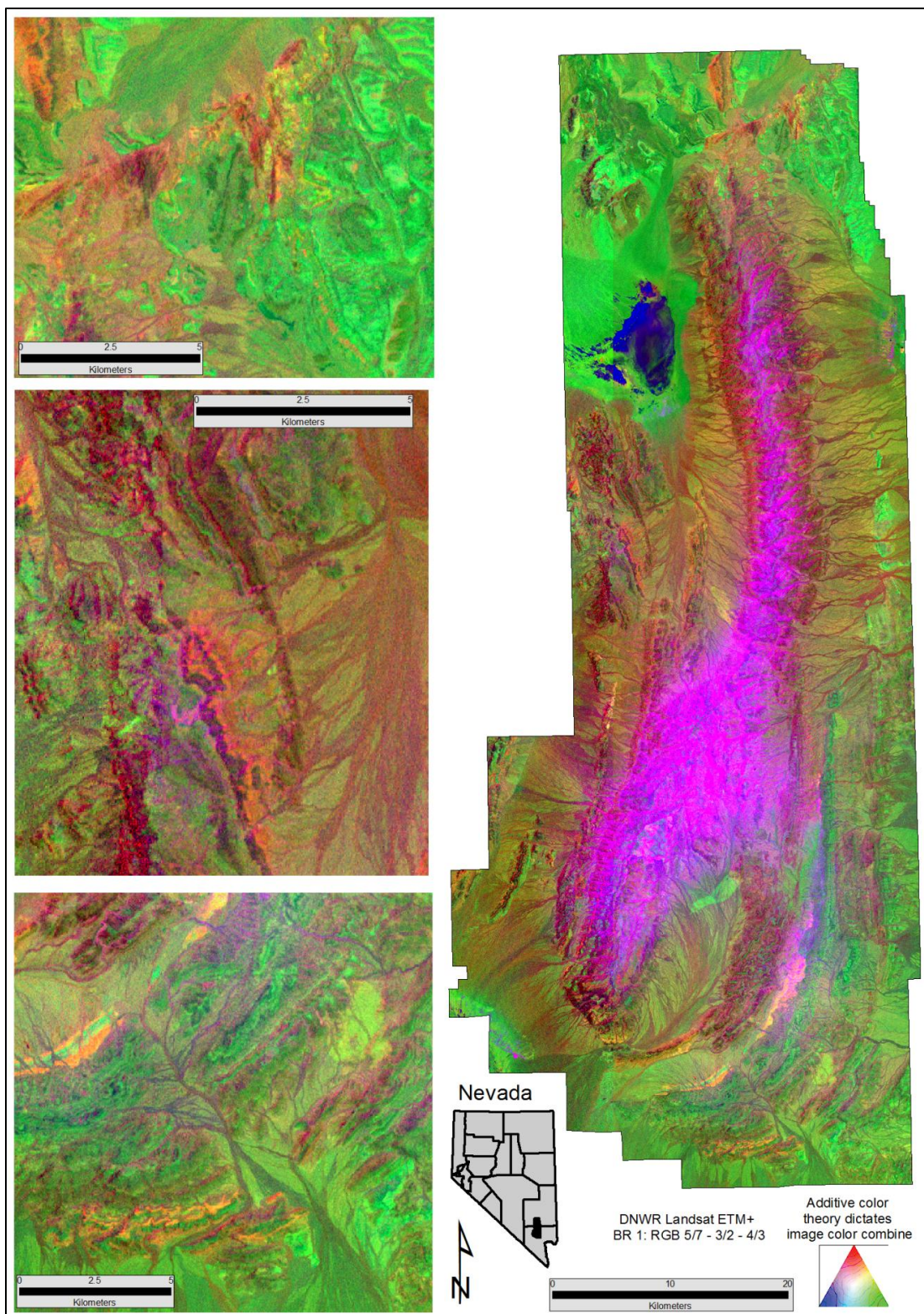
Location key for appendix figures. Boxes A, B, and C correspond with the Lake Mine area, East Desert Range, and Gass Peak District respectively.

Appendix Key: Landsat ETM+ band combinations and false color composite image descriptions.

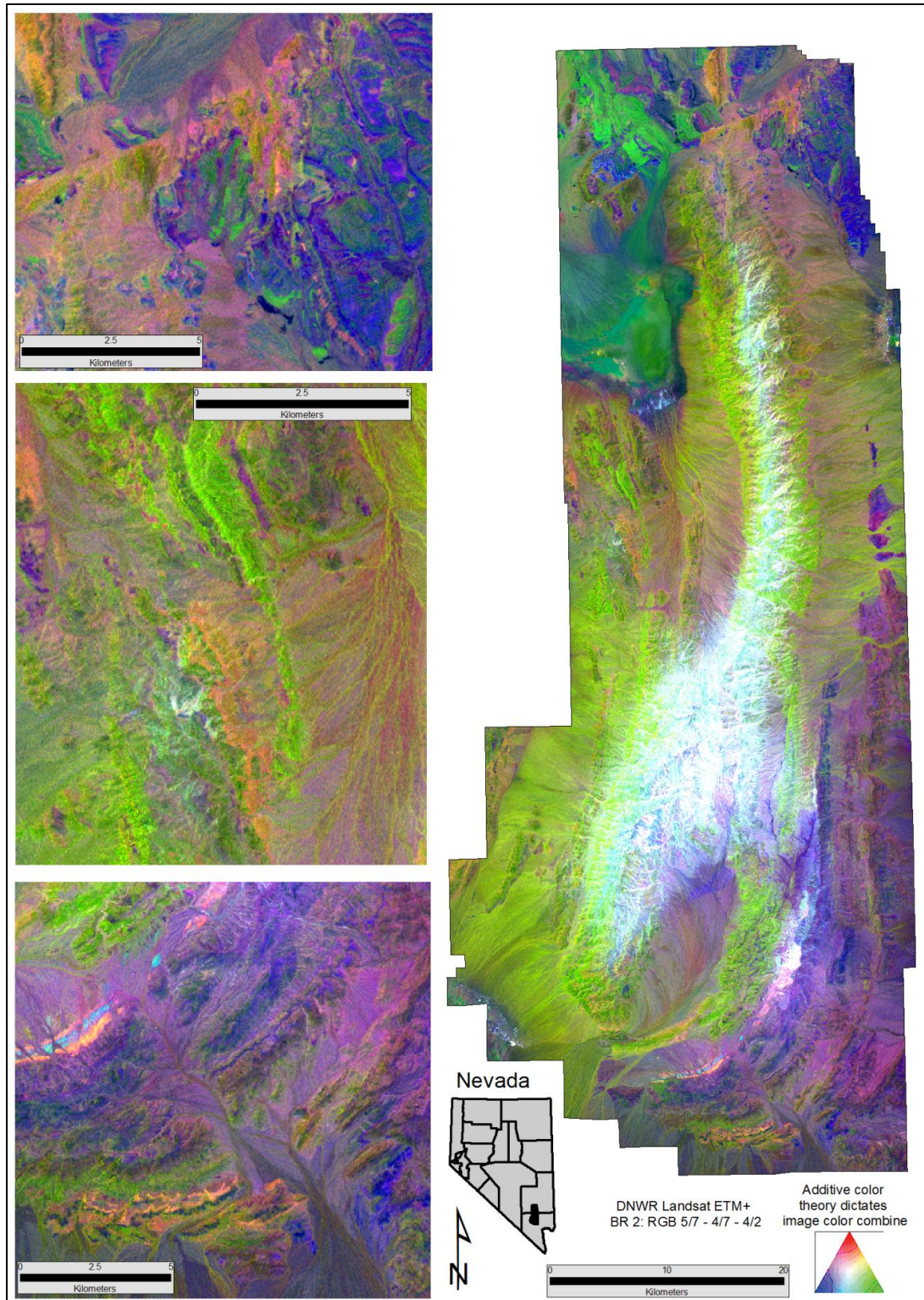
Landsat ETM+ Band Combination Images and Descriptions				
Image #	Red	Green	Blue	Description and/or Source
0	Band 3	Band 2	Band 1	True/Natural Color Image
1	5/7 FeOx/AlOH	3/2 Iron Oxide	4/3 Vegetation	"Abram's Ratio" - Abrams (1980)
2	5/7 FeOx/AlOH	4/7 Carbonate Rocks	4/2 Vegetation	Abram (1980)
3	5/7 FeOx/AlOH	5/1 Gossan	(5/4)(3/4) Unaltered Background	Inzana et al. (2003)
4	3/4 Outcrops	4/5 Gossan	5/7 FeOx/AlOH	Patel and Rumpel (1992)
5	PC Band 7	PC Band 4	PC Band 2	False color principle component stretch. principle component (PC) stretch disallows matching mineral groups to colors.
6	5/7 (PC Bands)	5/1 (PC Bands)	4 (PC Bands)	Colors should distinguish FeOx+AlOH, from mafic+FeIII rock use of PC stretch disallows matching mineral groups to colors but highlights differences between selected bands. Modeled after Abram (1980).
7	5/7 (PC)	4/5 (PC)	3/1 (PC)	Initial combination Red-FeOx+AlOH Blue-Gossan+Fe rich Green-FeOx. PC stretch disallows matching mineral groups to colors but highlights differences between selected bands. Modeled after Patel and Rumpel (1992).
8 9 10	5 5/7 5/7	4 3/1 3/1	1 1 5/4	Images used during 1993 assessment of DNWR. Primarily as a lithological discrimination image and to identify alteration as zones of higher albedo, not areas around Gass Peak in the in the north. Additionally other areas of red and magenta colors may indicate FeOx and clay minerals commonly associated with alteration south and Lake mine. Tingley et al. (1993)



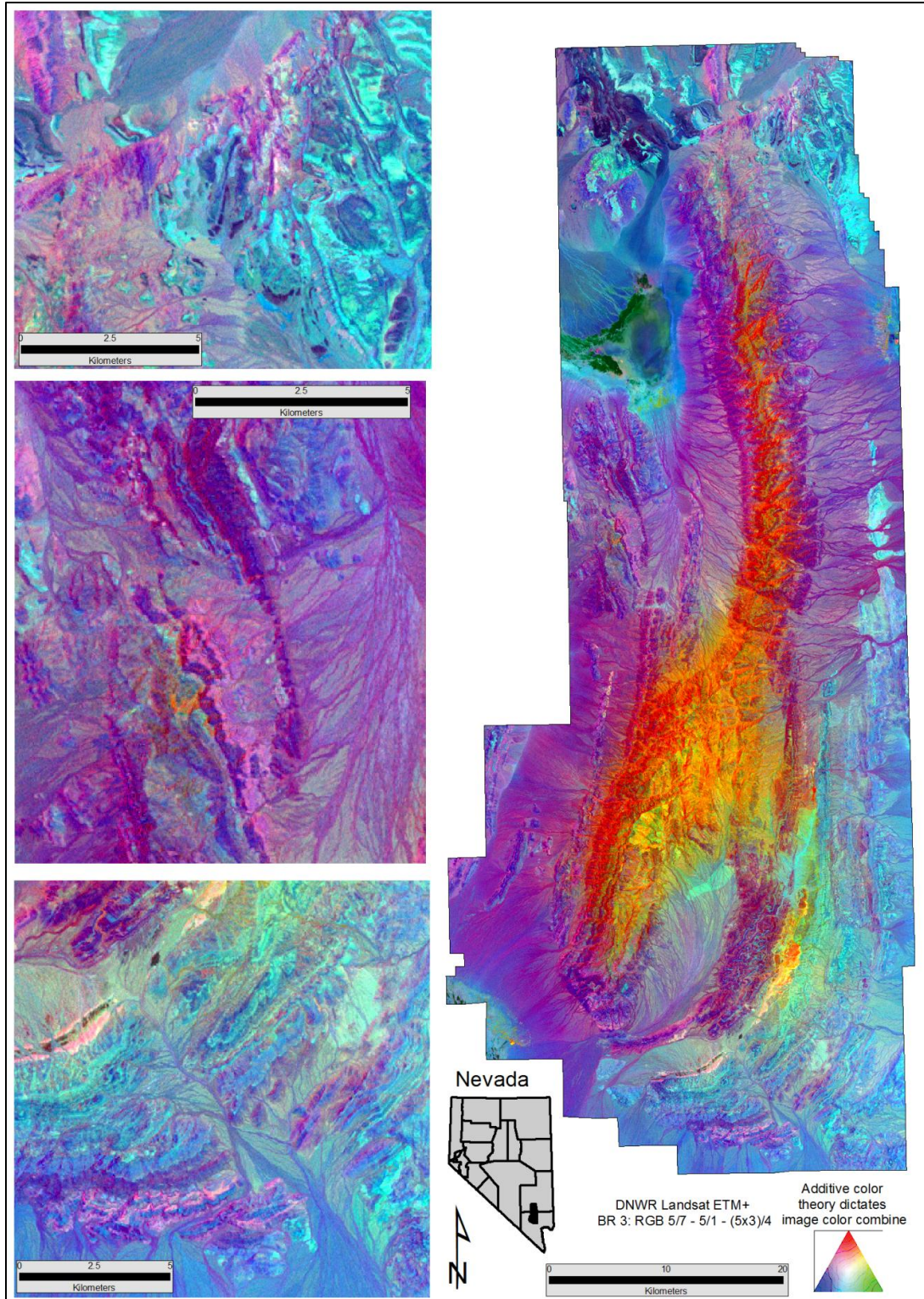
Landsat ETM+ Band Ratio Image 0 – True Color Image.



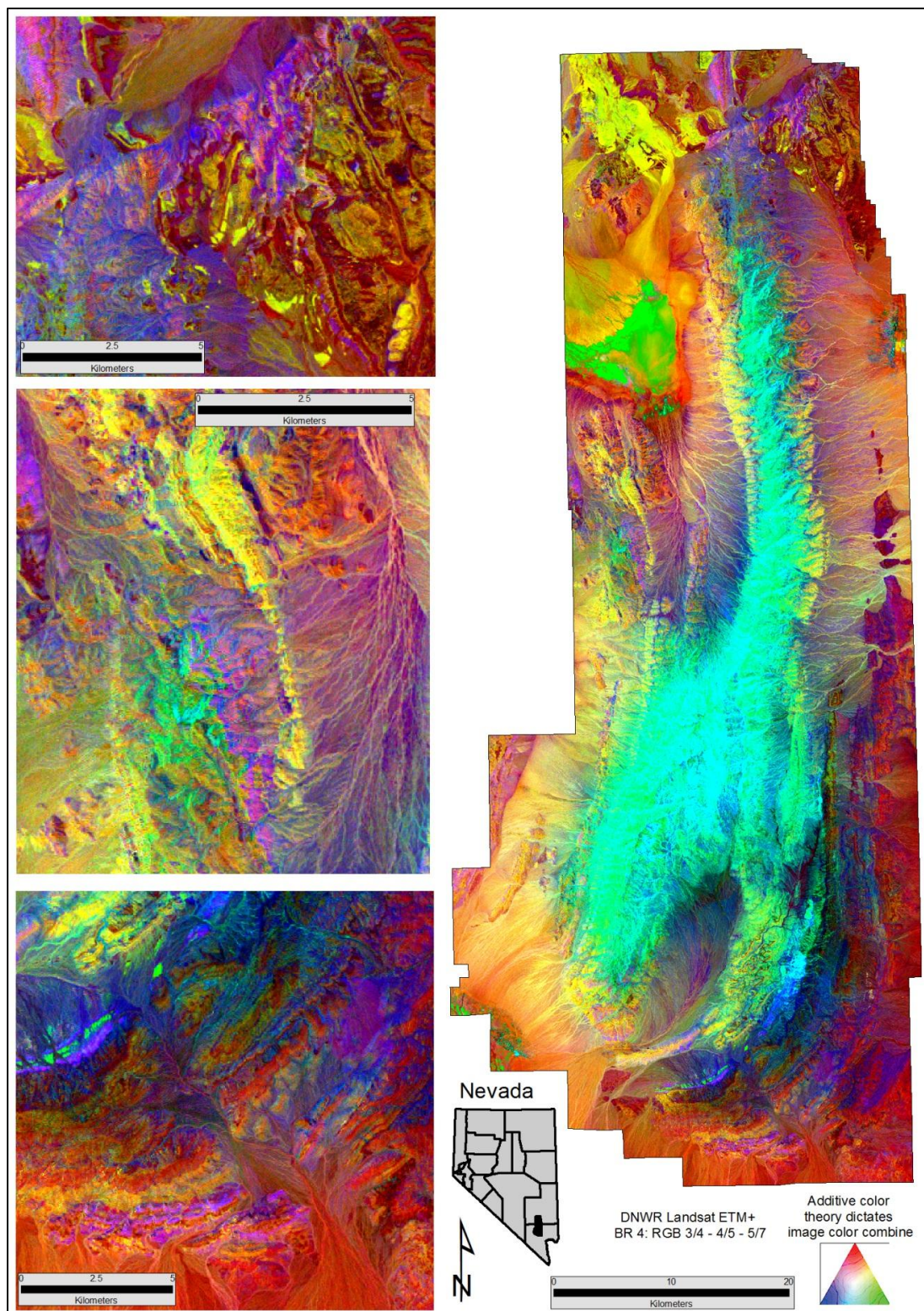
Landsat ETM+ Band Ratio Image 1 – R 5/7 FeO_x-AlOH; G 3/2 iron oxide; B 4/3 vegetation. Abrams (1980)



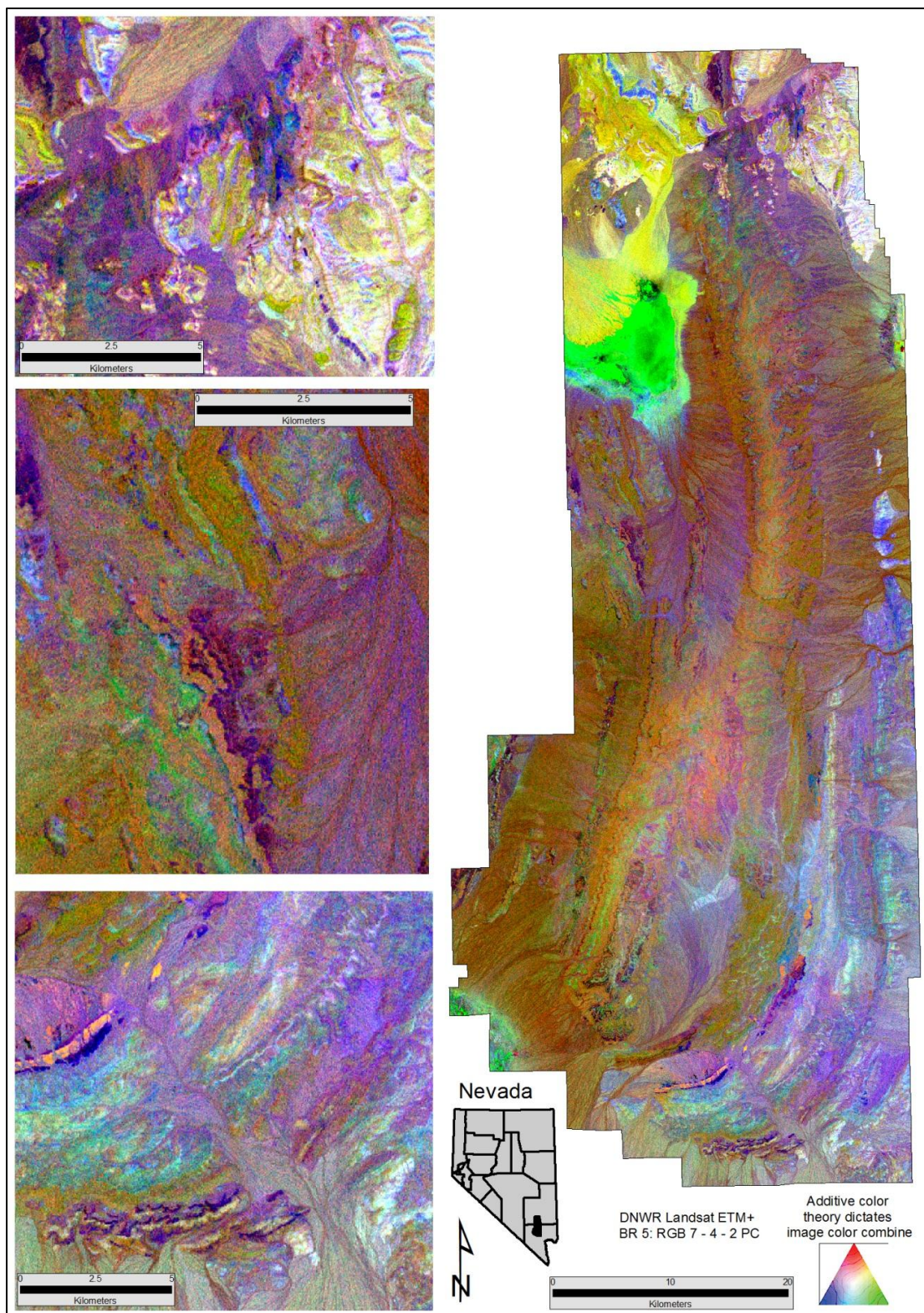
Landsat ETM+ Band Ratio Image 2 – R 5/7 FeOx-AlOH; G 4/7 carbonate rocks; B 4/2 vegetation.
 Abrams (1980).



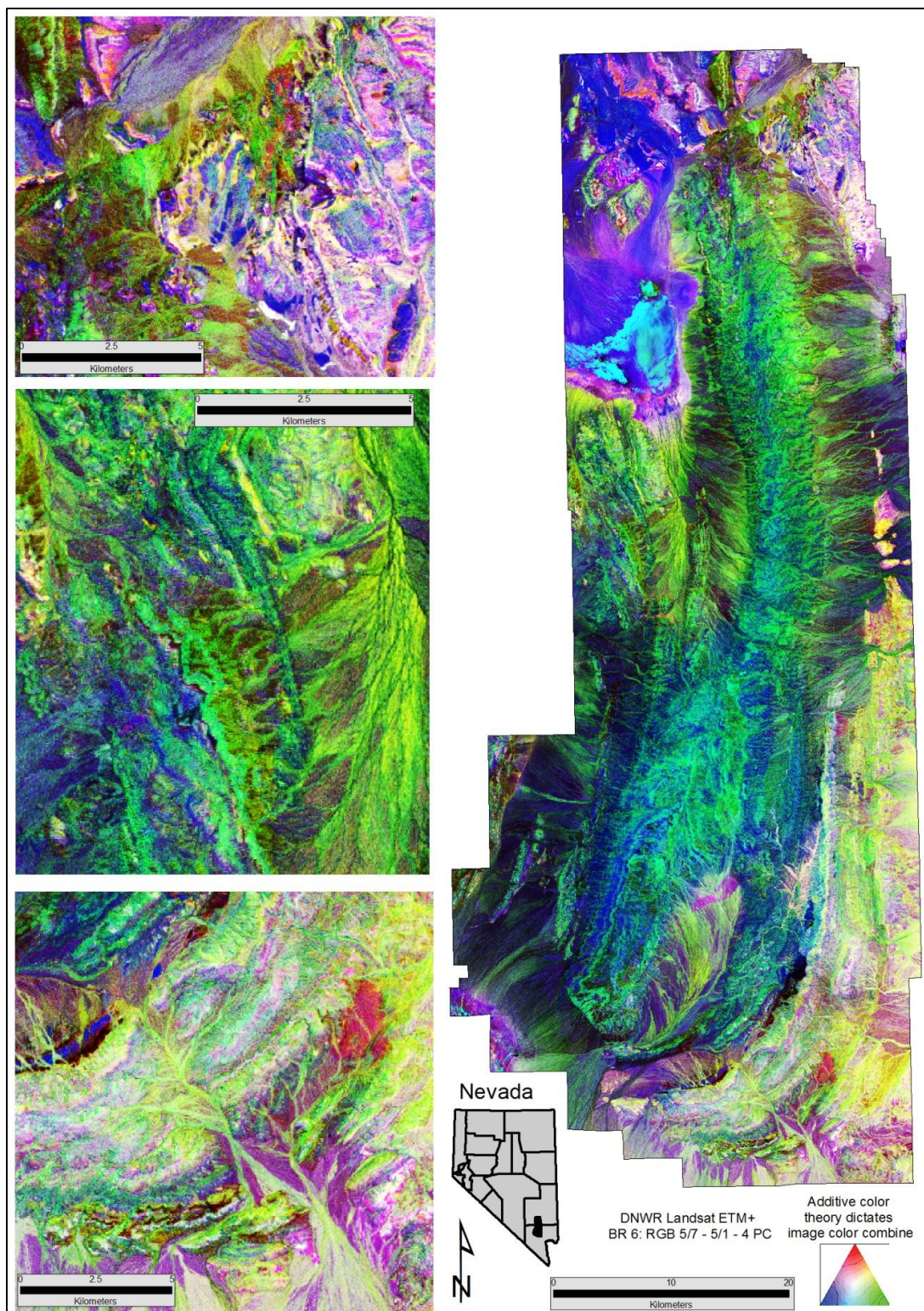
Landsat ETM+ Band Ratio Image 3 – R 5/7 FeOx-AlOH; G 5/1 gossan; B (5/4)(3/4) unaltered rocks. Inzana et al., (2003)



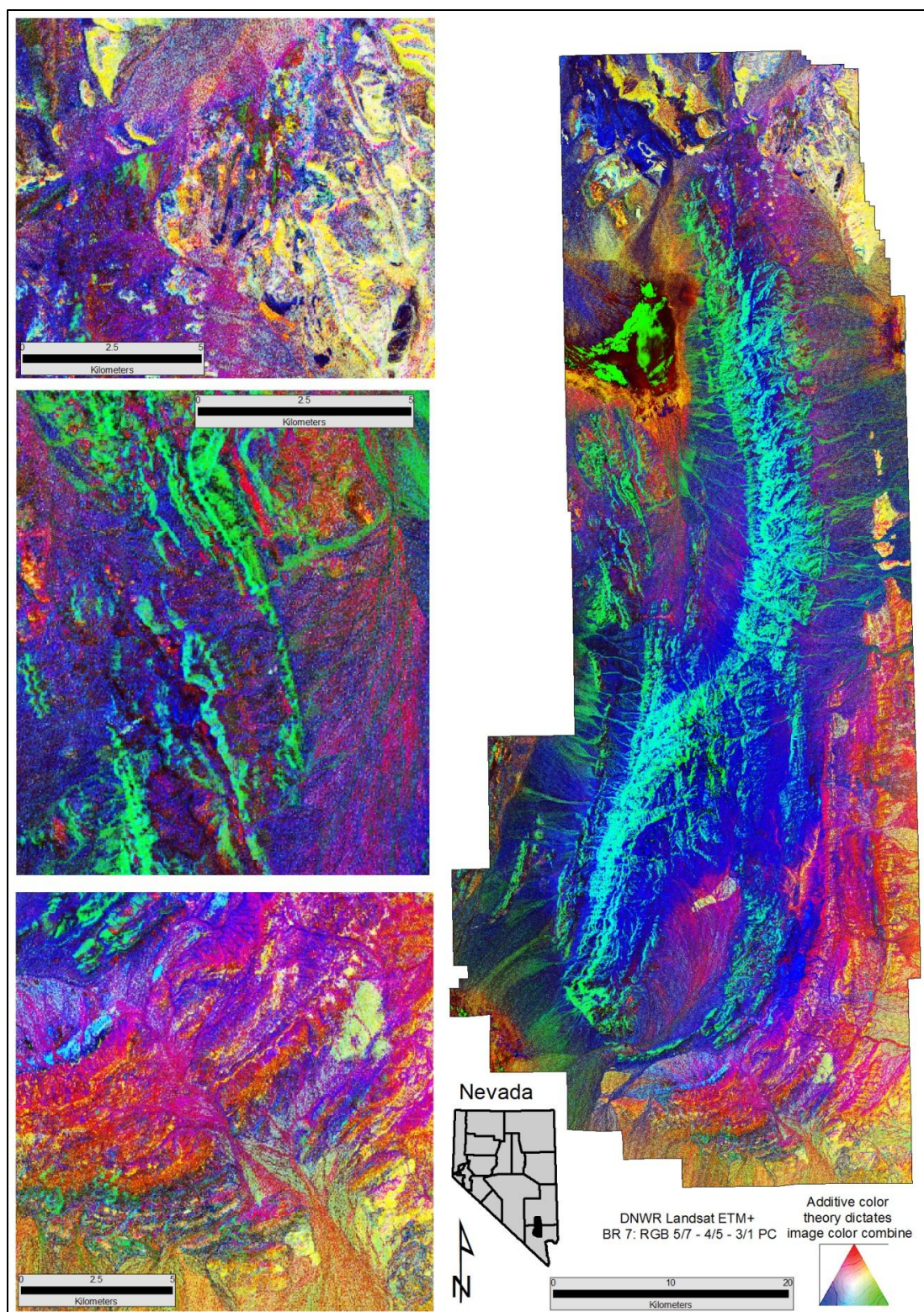
Landsat ETM+ Band Ratio Image 4 – R 3/4 outcrops; G 4/5 gossan; B 5/7 FeOx/AlOH. From Patel and Rumpel (1992).



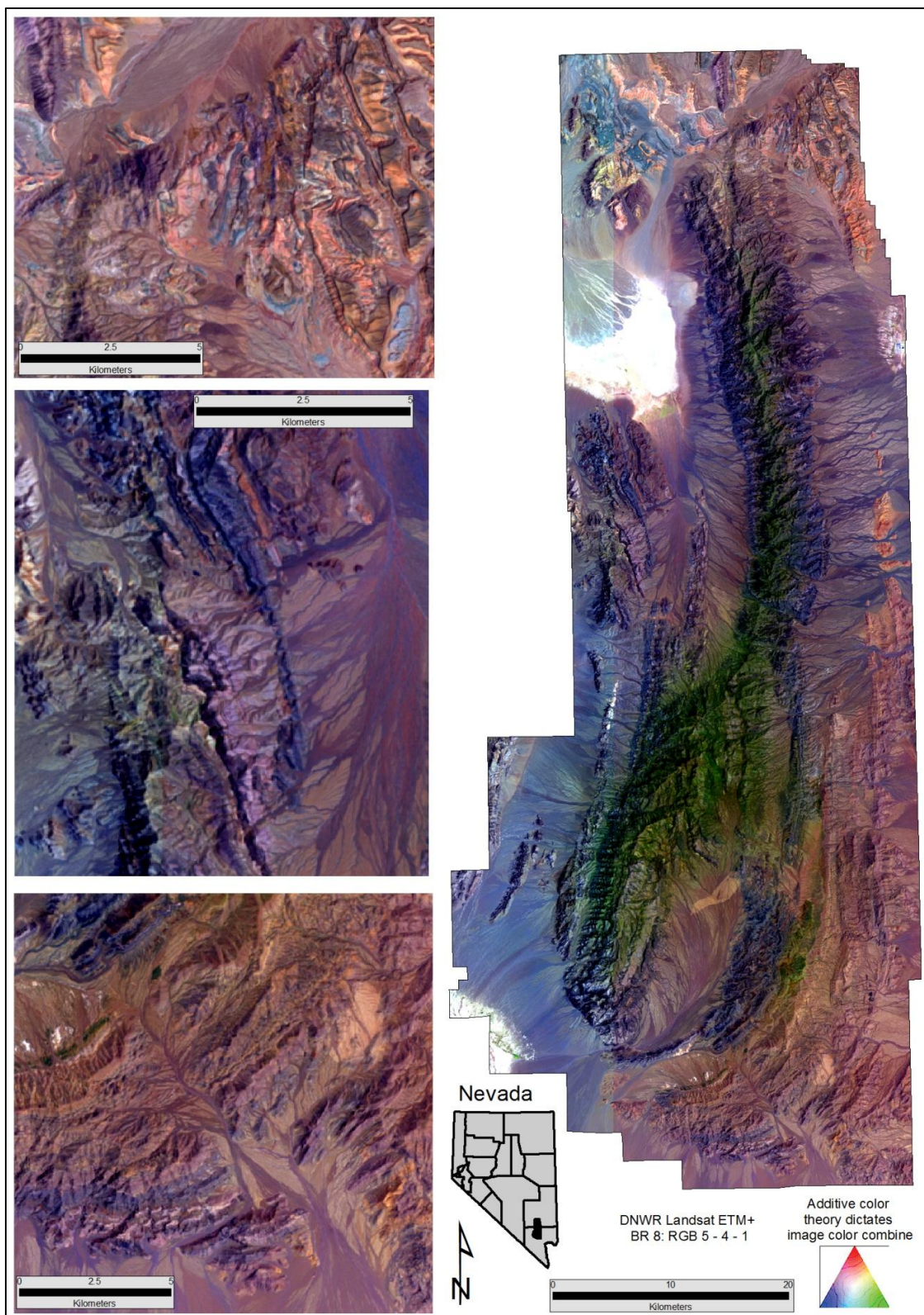
Landsat ETM+ Band Ratio Image 5 – R PC Band 7; G PC Band 4; B PC Band 2.



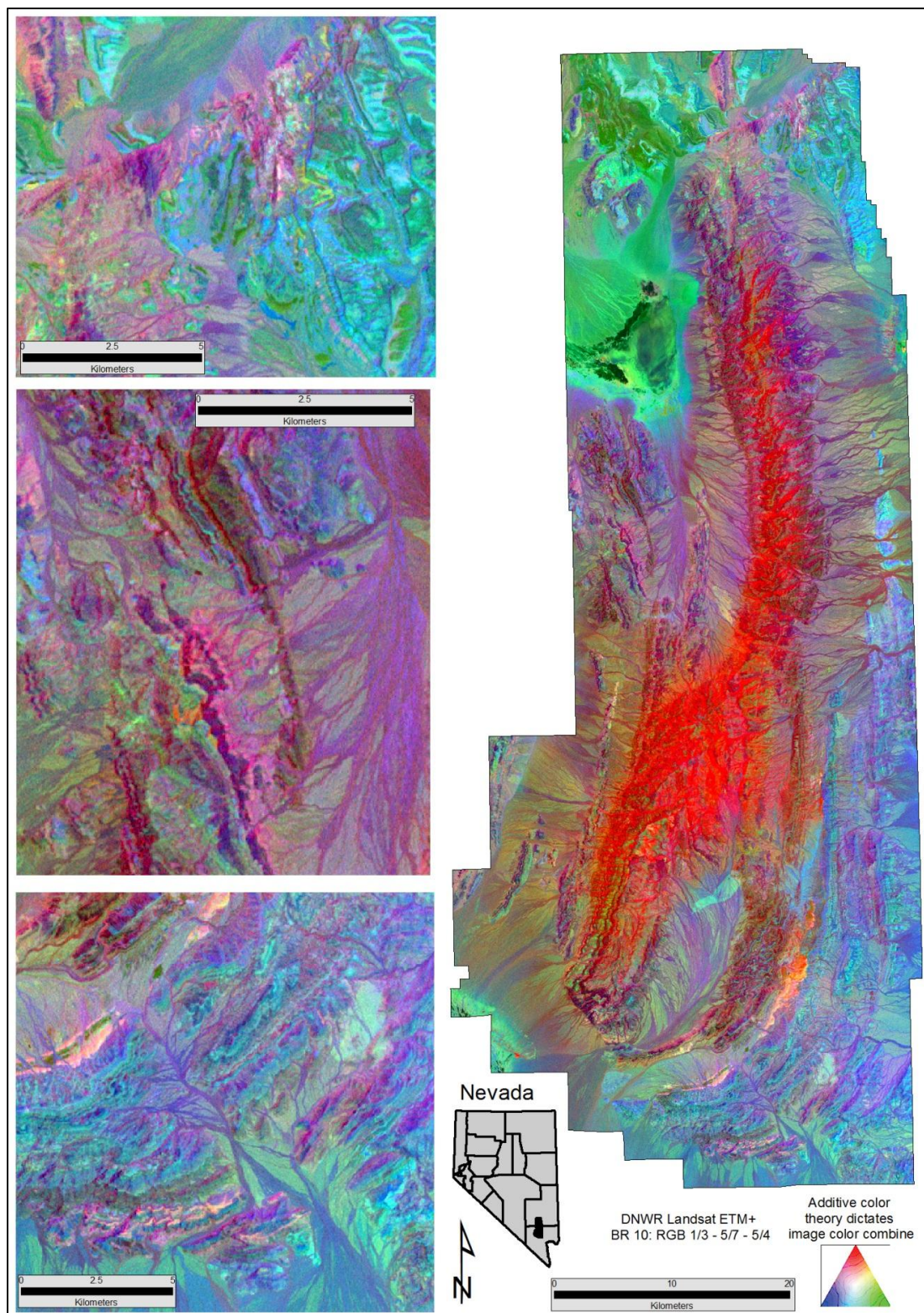
Landsat ETM+ Band Ratio Image 6 – R 5/7 PC Bands; G 5/1 PC Bands; B 4 PC Bands. Modified from Abram (1980).



Landsat ETM+ Band Ratio Image 7 – R 5/7 PC Bands; G 4/5 PC Bands; B 3/1 PC Bands. (Modeled after Patel and Rumpel (1992))

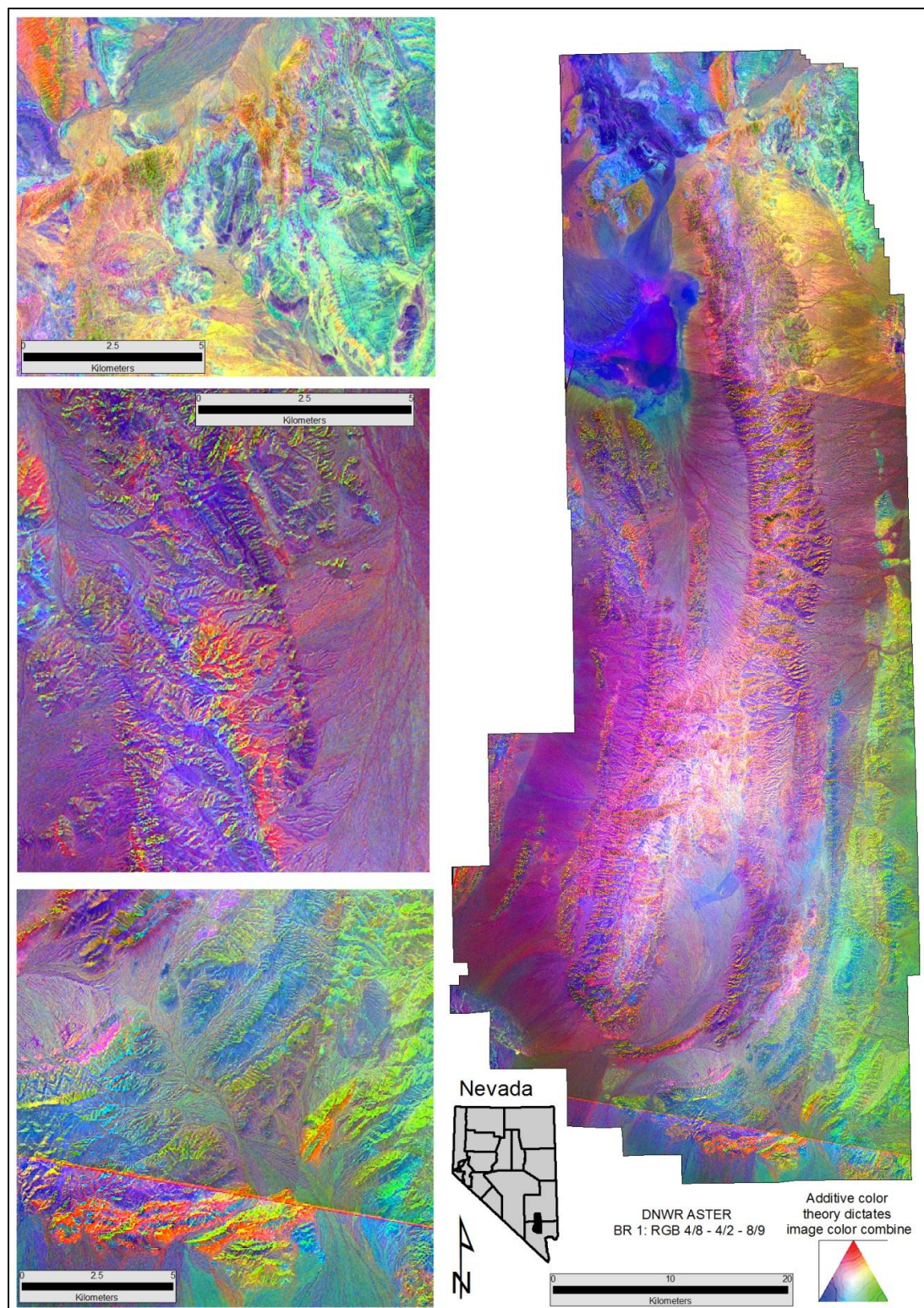


Landsat ETM+ Band Ratio Image 8 – R 5; G 4; B 1. From Tingley et al. (1993).

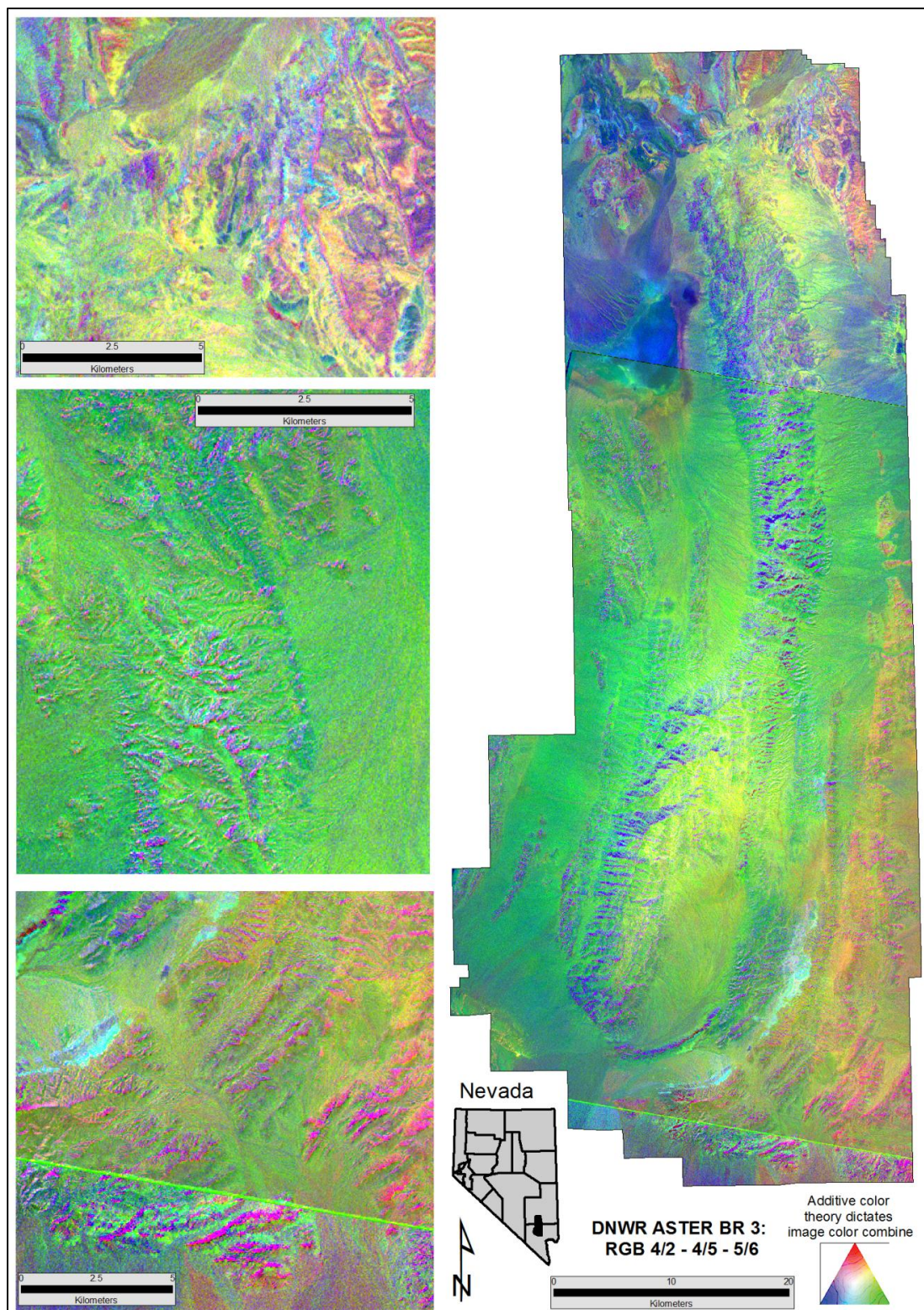


Landsat ETM+ Band Ratio Image 10 – R 5/7; G 3/1; B 5/4. From Tingley et al. (1993).

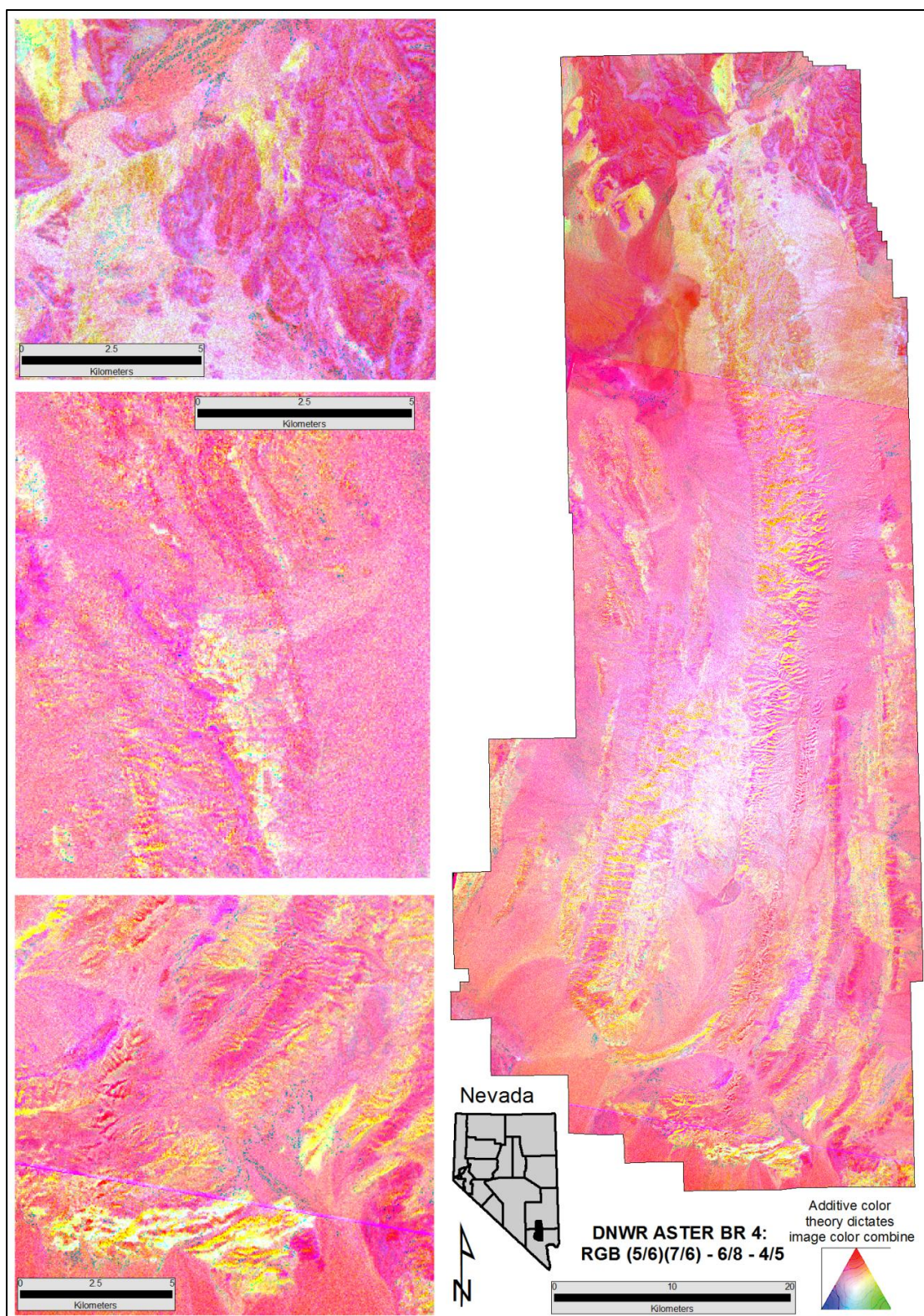
ASTER Band Ratio Combinations				
Image #	Red	Green	Blue	Source
1	4/8 FeOx	4/2 Alteration	8/9 Contrast	Gabr et al. (2010)
2	5/6 Sericite	7/6 Muscovite	7/5 Kaolinite	Hewson (2001)
3	4/2 Gossan	4/5 Alteration	5/6 Host	Volesky (2003)
4	5/6*7/6 Phengitic	6/8 Amphibole	4/5 Laterite	Bierwith (2002)
5	5/3+1/2 FeIII	(6+8)/7 Dolomite	(7+9)/8 Carbonate	Rowan et al., Combination (2003 & 2006)
6	Band 3	Band 2	Band 1	True/Natural Color Image
7	(11*11)/(10*12) Silica	13/14 Carbonate	12/13 Carbonate	Ninoyima et al. (2005)



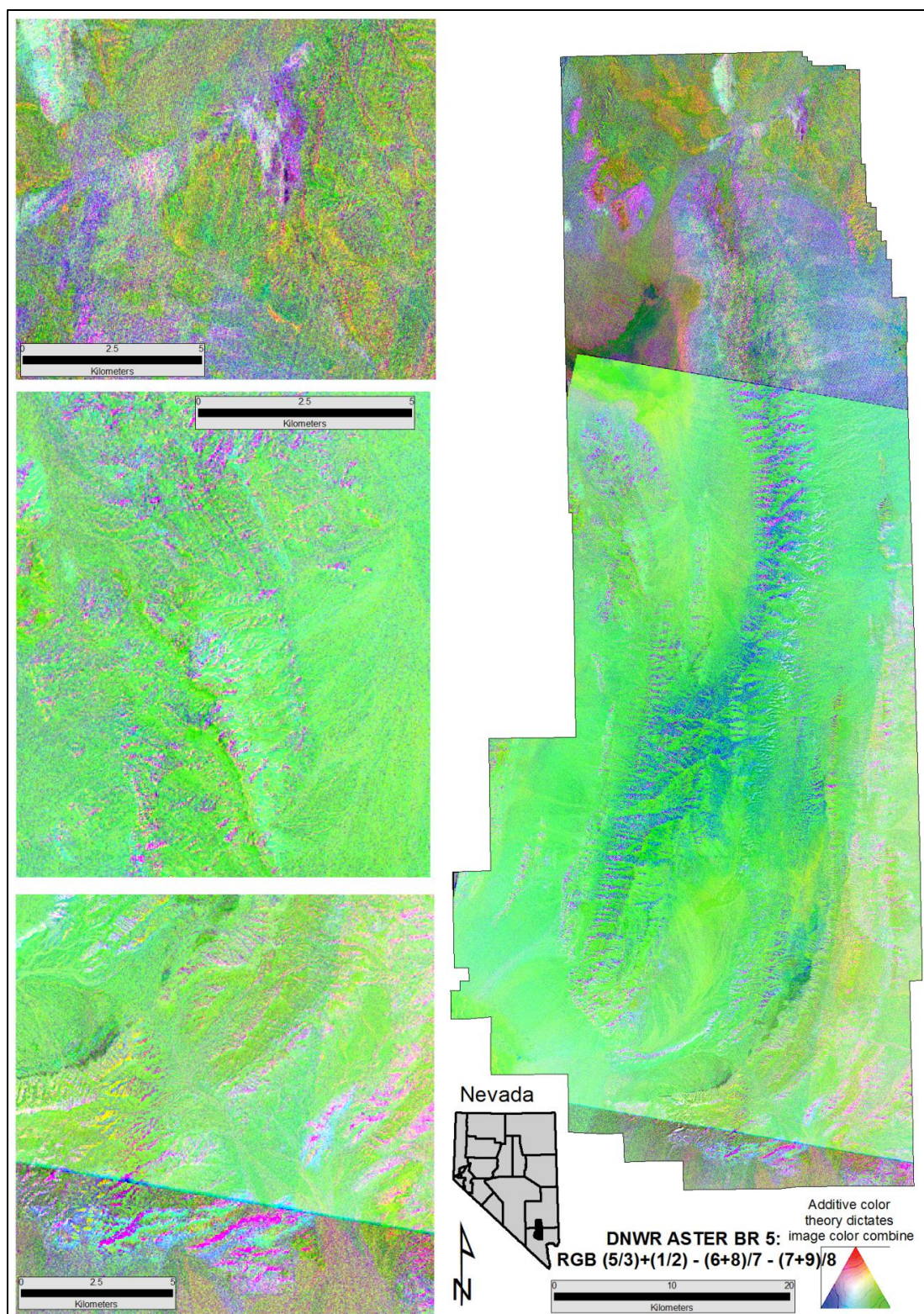
ASTER Band Ratio Image 1 – R 4/8 FeOx; G 4/2 Alteration; B 8/9 Unaltered Rocks. From Gabr et al., (2010).



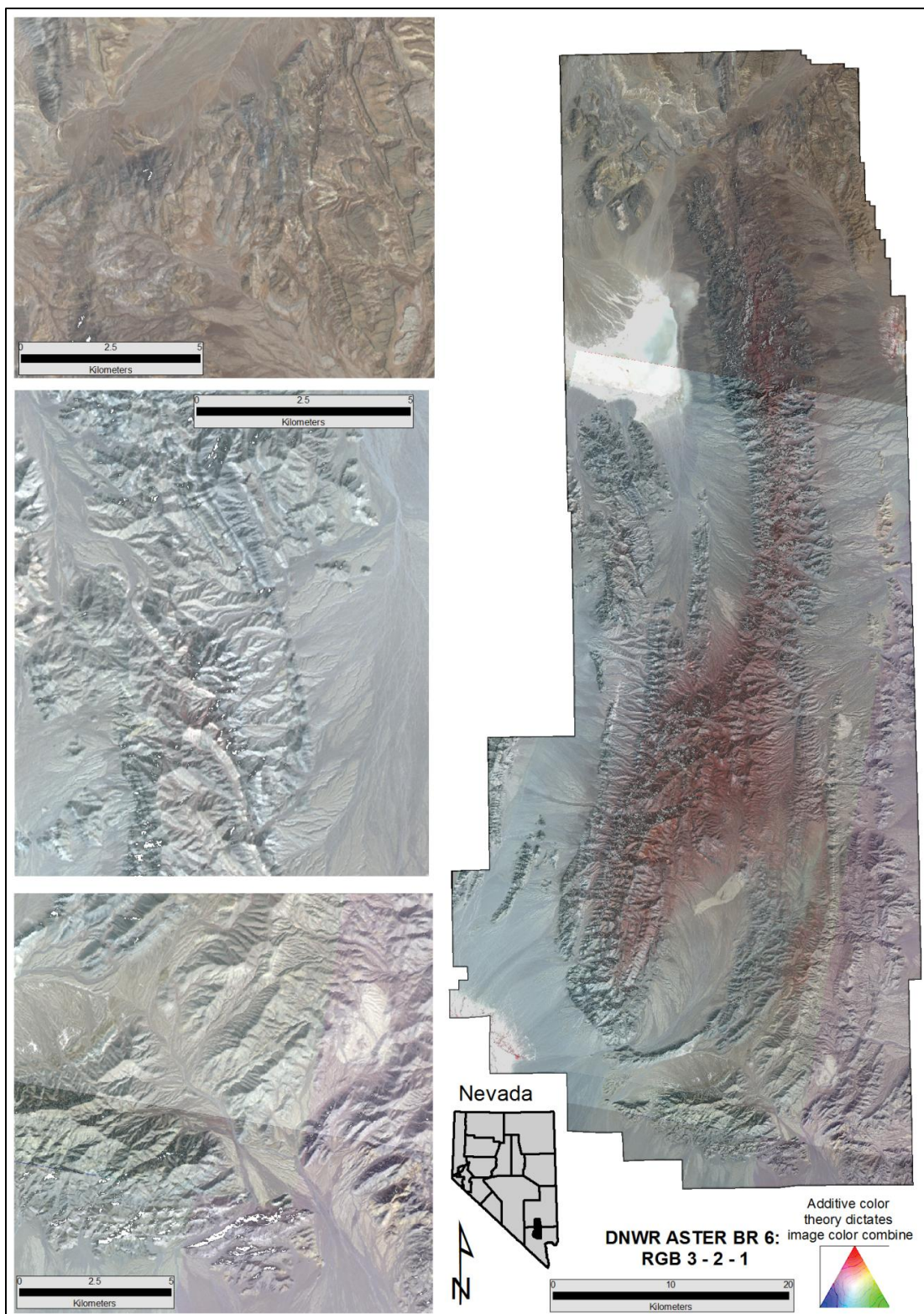
ASTER Band Ratio Image 3 – R 4/2 Gossan; G 4/5 Alteration; B 7/5 Unaltered Rocks. From Volesky, (2010).



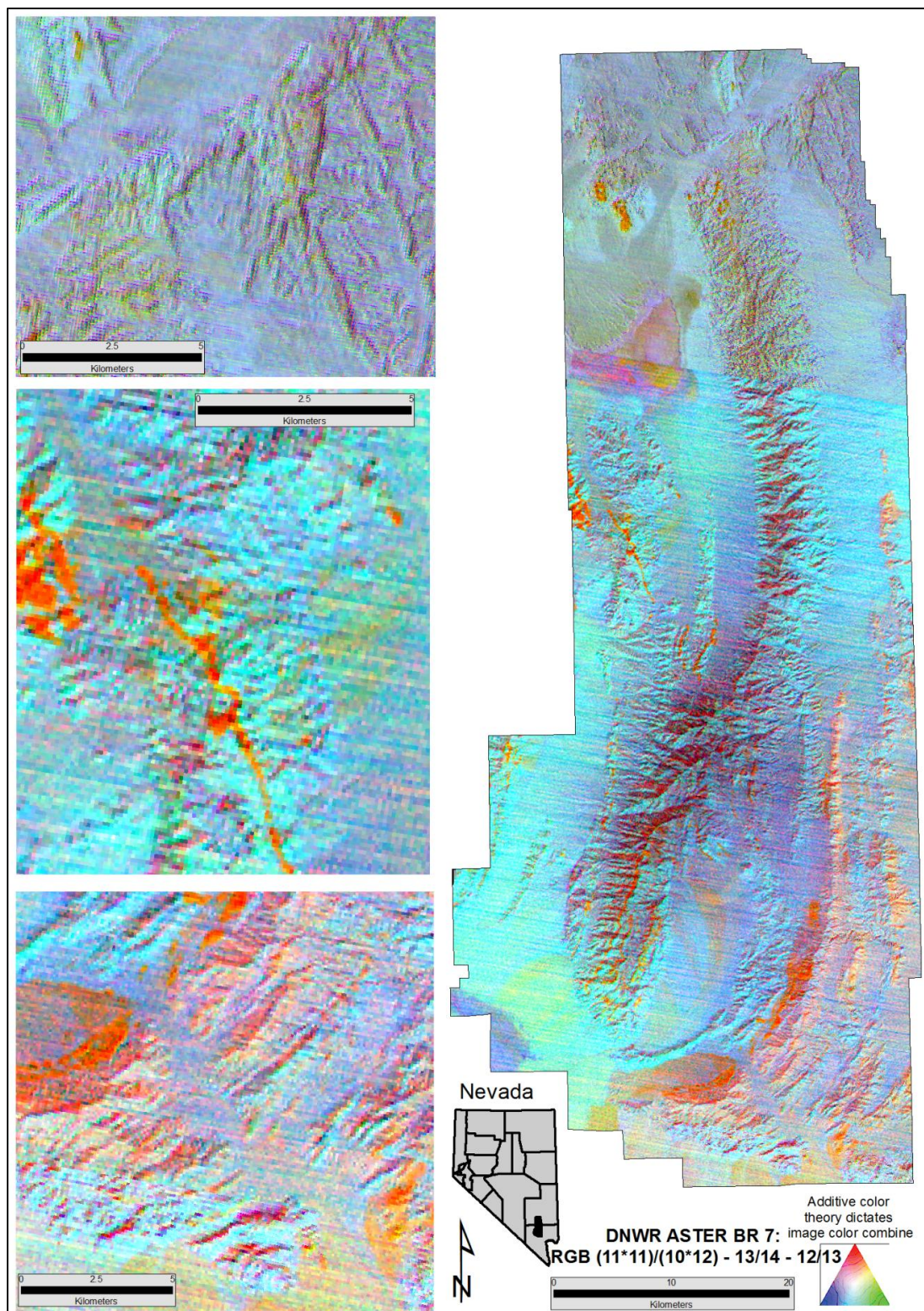
ASTER Band Ratio Image 4 – R (5/6)(7/6) phengitic; G 6/8 amphibole; B 4/5 laterite. From Bierwith et al., (2010).



ASTER Band Ratio Image 5 – R $(5/3+1/2)$ FeIII; G $(6+8)/7$ dolomite; B $(7+9)/8$ carbonate. Combination of Rowan band ratios (2003 and 2006).

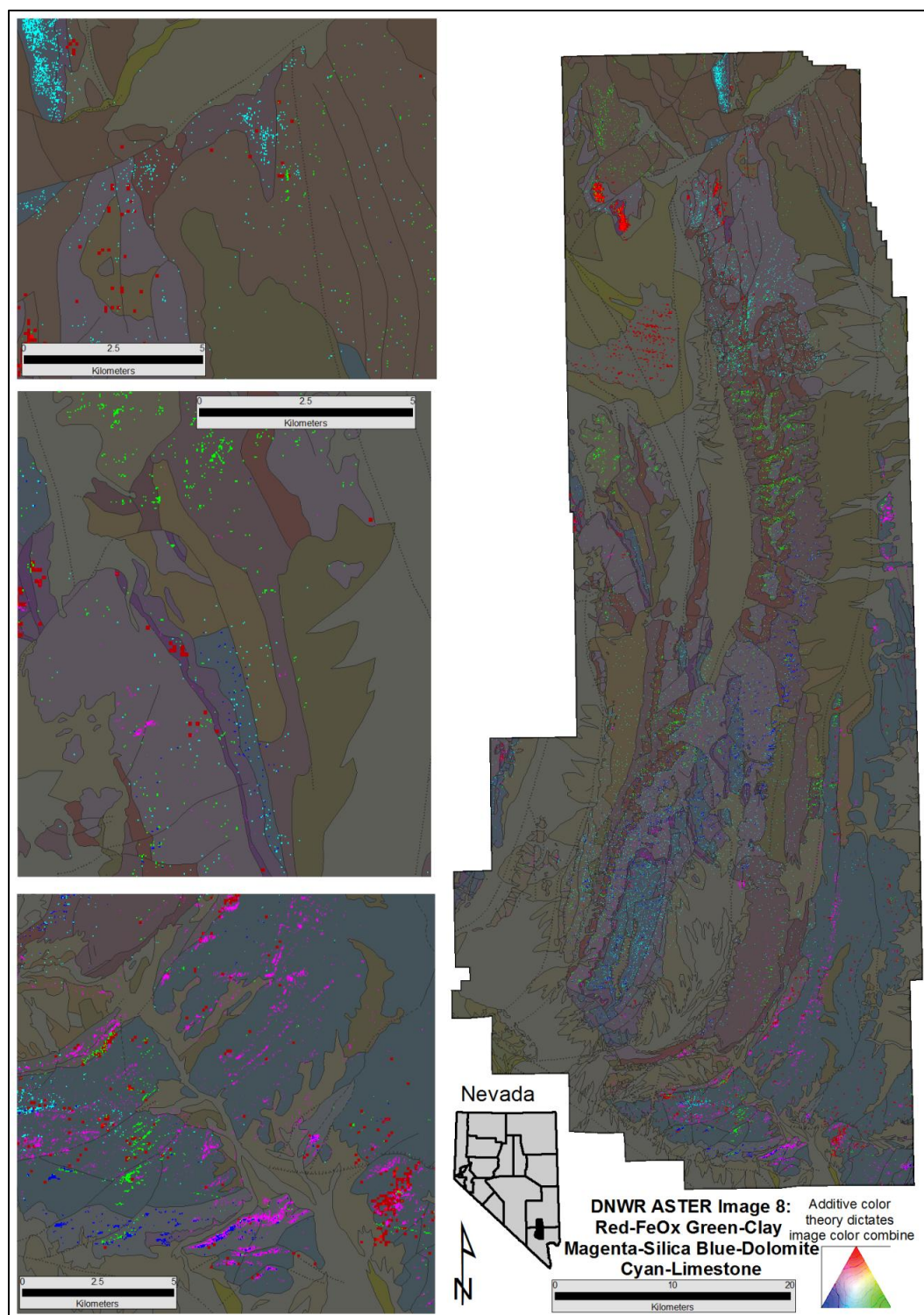


ASTER Band Ratio Image 6 – R 3; G 2; B 1. True color image.



ASTER Band Ratio Image 7 – R (11*11)/(10*12) silica; G 13/14 carbonate; B 12/13 carbonate. From Ninoyima (2003B).

Mineral Index Methods*				
8 (Multi-color image)	Red-FeOx		Green-Clay	Mineral Likelihood Index Map
	Magenta-Silica	Cyan-Limestone	Blue-Dolomite	
Dolomite: Mask of ratios $4/5 > 1$; $5/6 > 1$; $7/6 < 1$; $7/5 < 1$; $7/8 < 1$; $9/8 > 1$, $6/9 > 1$ on SFF result for Dolomite 1				
Calcite: Mask of ratios $4/5 > 1$, $5/6 > 1$, $7/6 < 1$, $7/5 < 1$, $7/8 > 1$, $9/8 > 1$, $5/8 > 1$, $6/9 > 1$ on SFF result for SFF result for Calcite 3				
FeOx: Mask of ratios $2/1$, $3/2$, & $3/1$ within known ranges for goethite, hematite & jarosite on PC3 of PC123				
ALOH: Mask of ratios $4/5 > 1$; $7/6 > 1$, $7/8 > 1$; on ratio $7/6$				
Silica: Mask of band ratios $12/13 < 1$; $12/11 < 1$; $13/11 > 1$; $11/10 > 1$ on TIR MF result for silica				
*Note: Mineral Index Methods mask values are approximated here due to variables such as time of day, time of year, light cloud cover, pixel mixing etc. When masking band ratios the operator must set parameters to highlight contiguous pixels, ideally over regions known to contain the desired end member. This applies to all $< > =$ operations shown above. (Specific masking thresholds used during this study can be found in the appendix.)				



ASTER Image 8 – Highly constrained mineral likelihood map. Modified from Agar (2010) mapping methods.

Appendix B – Final Mapping Parameters

"Spectral Angle Mapper" - Mapping Parameters				
North DNWR	Mineral	Color	SAM Max Angle	Threshold For Rule Image
	Limestone	Cyan	0.096	.085-.096
	Silica	Red	0.1	.09-.10
	Dolomite	Blue	0.09	.085-.090
	Iron Oxide	Magenta	0.09	.08-.09
	Clay	Green	0.065	.055-.0650
North Sheep	Mineral	Color	SAM Max Angle	Threshold For Rule Image
	Limestone	Cyan	0.09	.075-.09
	Silica	Red	0.12	.11-.119999
	Dolomite	Blue	0.1	.09-.0999
	Iron Oxide	Magenta	0.12	.115992-.119959
	Clay	Green	0.075	.07-.08
DNWR East East	Mineral	Color	SAM Max Angle	Threshold For Rule Image
	Limestone	Cyan	0.1	.09-.1
	Silica	Red	0.12	.11-.12
	Dolomite	Blue	0.11	.1-.11
	Iron Oxide	Magenta	0.14	.136-.139954
	Clay	Green	0.088	.08-.087995
DNWR East West	Mineral	Color	SAM Max Angle	Threshold For Rule Image
	Limestone	Cyan	0.09	.08-.09
	Silica	Red	0.105	.09-.1050
	Dolomite	Blue	0.092	.066688-.09200
	Iron Oxide	Magenta	0.1	.09-.09995
	Clay	Green	0.08	.07-.08
Gass Peak East	Mineral	Color	SAM Max Angle	Threshold For Rule Image
	Limestone	Cyan	0.095	.075-.095
	Silica	Red	0.125	.11-.125
	Dolomite	Blue	0.11	.01-.010999 (*+ 0.2-0.3 observed)
	Iron Oxide	Magenta	0.155	.15-.155
	Clay	Green	0.095	.08-.095
Gass Peak West	Mineral	Color	SAM Max Angle	Threshold For Rule Image
	Limestone	Cyan	0.089	.075-.089
	Silica	Red	0.11	.068398-.109988
	Dolomite	Blue	0.12	.10-.12 *(+0.25-0.3 Observed)
	Iron Oxide	Magenta	0.145	.14-.145
	Clay	Green	0.095	.065573-.094999
				* High values are generally excluded as anomalous, here dolomite and limestone were observed in the field validating the higher levels of the SAM score.

Feature Index	Applied to image	Color	Mask Ratios	Gass Peak W	Gass Peak E	Sheep Range E	Sheep Range W	Sheep Range N	Pahranagat Range
				Class Threshold	Class Threshold	Class Threshold	Class Threshold	Class Threshold	Class Threshold
FeOx	PC3 from PC123	Magenta	2/1	>1	>1	>1	>1	>.91	>.93
			3/2	>1.21	>1.3	>1.3	>1.3	>1.2	>1.15
			3/1	>1.25	>1.3	>1.2	>1.25	>1.15	>1.16

Feature Index	Applied to image	Color	Mask Ratios	Gass Peak	Sheep Range	Sheep Range N	Paharanagat Range
				Class Threshold	Class Threshold	Class Threshold	Class Threshold
Silica	Band 14/12	Red	12/13	>0.88	>0.85	<0.92	<0.92
			12/11	>1.025	>1.045	<1.04	<1
			13/11	<1.17	<1.2	>1.2	>1.115
			11/10	N/A	<1.22	>1.04	>1.03
			14/13	<1.2	N/A	N/A	N/A